Numerical investigation of the influence of subduction on deformation within the overriding plate

Zhibin Lei

School of Earth and Environmental Sciences

Cardiff University

Submitted in partial fulfilment of the requirements for the degree of

Doctor of Philosophy

September 2022

Abstract

Subduction can pose a fundamental tectonic overprint on the overriding plate by generating a variety of deformation patterns incorporating both extension and shortening strains. Latest research suggests that the diversity of subduction configuration, e.g., multiple slab interaction, inherited tectonic setup, plays an important role in affecting the deformation patterns observed in the overriding plate. However, the driving mechanism accounting for the initiation of the deformation, especially extension, in the diversified subduction configuration is still much less explored, for which this thesis aims at a better understanding through thermal mechanical numerical modelling.

In Chapter 3, the thesis investigates single-sided subduction (SSS). Previous investigation implies that it takes a pre-weakened or an immobile overriding plate to reproduce back-arc extension. Nevertheless, it skips answering how the overriding plate gets weakened or becomes immobile before extension initiates. Here, results show that back-arc extension can self-consistently emerge as trench retreat rate increases, even when the overriding plate is mobile and homogeneous. This is a significant advance in simulating back-arc extension, though the trench retreat rate can go higher than what has been observed in current plate framework, suggesting that additional processes may also need to be considered, e.g., melt weakening, grain size reduction etc.

In Chapter 4, the thesis investigates dual inward dipping subduction (DIDS), which, as recent research suggests, can affect the deformation patterns in the overriding plate. A major improvement here is incorporating a composite rheology which enables plate to weaken self-consistently relative to previous DIDS models. It does this by inhibiting

the mobility of the overriding plate and forming a stronger upwelling mantle flow underlying the overriding plate relative to SSS models. Composite rheology also enables investigation on the evolution of dominant deformation mechanism, which shows dislocation and yielding contribute most to viscosity reduction in the overriding plate. This is a significant advance in simulating DIDS, and the quantitative method proposed here to evaluate each deformation mechanism's contribution to viscosity reduction can be a powerful tool to understand other strain localisation processes, e.g., formation of plate boundaries.

Observation shows that the distance from marginal extension centre to the nearest trench ranges from ~170-850 km, of which the driving mechanism is unclear. In Chapter 5, the thesis investigates the role of heterogeneity within the overriding plate in affecting the distance from extension to trench. The results show that the location and size of the continental block can efficiently regulate if and where marginal basin develops within the overriding plate.

Overall, this thesis demonstrates the strong coupling between slab induced mantle flow and deformation in the overriding plate, and improves the current understanding on how progressive weakening can influence back-arc or marginal extension.

Acknowledgements

I was laughing when I first heard that someone would like to pursue a PhD degree just to make sure his name on the gravestone starts with "Dr". Now that I am around the end of this journey to earn that title. I became aware of the weight and honour underlying it. As all doctoral students know, behind the name on the cover page of the thesis are a wealth of others who shared their knowledge, advice, experience, time, and friendship to achieve what it looks like now.

First and foremost, I sincerely thank my supervisor and friend, Prof. Huw Davies. I won't even be possible to step on a geodynamic research path and reach so far without his patient guidance and warm support.

Many thanks for the HAWK support team, especially Thomas Green and Jose Munoz Criollo on helping me installing and updating Fluidity. Thank Dr Ian Thomas who helps setting up Fluidity environment on Louisville, Quartz and HAWK.

I also thank the many people with whom I have had constructive discussions and emerging new ideas, especially Dr Adam Beall, Dr Anouk Beniest, Dr Hongyuan Zhang. Also thank Anouk Beniest for mentoring me on my first vEGU and shared a lot her PhD and postdoc experience.

Thank the group members Dr James Panton, Dr Evie Snee, Duo Zhang, Gwynfor Morgan, Nicolas Recalde, Abigail Plimmer for reading paper together and hanging out now and then.

Thank Prof. Minghui Yang for encouraging me to apply for the doctoral project, when I was not confident enough to face the great difficulty to study abroad.

Table of contents

List of figures

List of tables

Chapter 1   Introduction

Subduction of the oceanic plate is a profound process generating the plate tectonic framework, which distinguishes Earth from other planets lacking life (eg. Stern, 2018). Subduction can drive both geo-hazards and localised deformation which can affect the overriding plate, imposing a huge impact upon the local area or even global regions (eg. Baxter et al., 2020; Bevis et al., 1995; Kusky, 2022). Integrating these short-term events over time develops long-term and regional scale tectonic consequences, which can alter the thermal and compositional structure of the overriding plate. The tectonic overprint includes the formation of plutonic intrusions, volcanic island arcs, back-arc basins, continent marginal basins, thinning lithosphere, and intraplate volcanism, all of which hold mineral and hydrocarbon potentials (Arnulf et al., 2022; Caratori Tontini et al., 2019; Ficini et al., 2017; Fouquet et al., 1991; Halbach et al., 1989; Uyeda and Kanamori, 1979; Yang and Faccenda, 2020). It is thus important to figure out the driving mechanism of the deformation process that oceanic subduction induces within the overriding plate, which this thesis will focus on. To begin with, the life cycle of the oceanic floor is briefly reviewed.

1.1   The life of an oceanic floor

1.1.1   Born to retire

Oceanic floor observation in the 1950s and 1960s revealed the life span of an oceanic floor (Hess, 1962). The oceanic plate is born at a mid-ocean ridge and the age of the plate increases linearly with its offset away from the mid-ocean ridge. Meanwhile, the oceanic plate cools down, and its thermal thickness and density increases (Becker et al., 2009; Davies and Davies, 2010; Parsons and Sclater, 1977; Richards et al., 2018; Stein and Stein, 1992). As a result, the negative buoyancy of the oceanic plate builds

up gradually and the oceanic floor subsides (Conrad and Lithgow-Bertelloni, 2002; Crameri et al., 2019). At a certain point when the negative buoyancy is strong enough to overcome all resistance, subduction initiates and the oceanic plate starts to be recycled into the deep earth (Crameri et al., 2020; Hall et al., 2003; Knight et al., 2021; Maunder et al., 2020). It is worth noting that the maximum age of an oceanic plate at the trench today is ~200 Ma old (Becker et al., 2009; Coltice et al., 2012; Crameri et al., 2019). The absence of oceanic plate older than 200 Ma suggests that old oceanic plate has a strong tendency to initiate self-driven subduction.

While mature subduction is mainly driven by the negative buoyancy of the cold subducting slab relative to the underlying the mantle (e.g., Gerya, 2022; Korenaga, 2013; Vlaar and Wortel, 1976), the driving mechanisms for subduction initiation are more diverse and include forced horizontal convergence (Candioti et al., 2020; Crameri et al., 2020; Hall et al., 2003), plume-driven (Baes et al., 2016; Cloetingh et al., 2021; Gerya et al., 2015; van Hinsbergen et al., 2021), impact-driven (O'neill et al., 2017) etc. It is important to note that one single mechanism is unlikely to explain every subduction initiation event, but rather different mechanisms are possible in different regions (Gerya, 2022).

After subduction initiates, the slab starts to interact with the upper mantle while subducting to a deeper depth until it achieves static equilibrium gradually (Figure 1.1). Most slabs flatten more or less at the depth of 660 km transition zone, where the slab is expected to experience force rebalance as viscosity jumps upwards due to the phase change of mantle minerals and upward density jump (Fukao et al., 2009; Goes et al., 2017; Li et al., 2019).
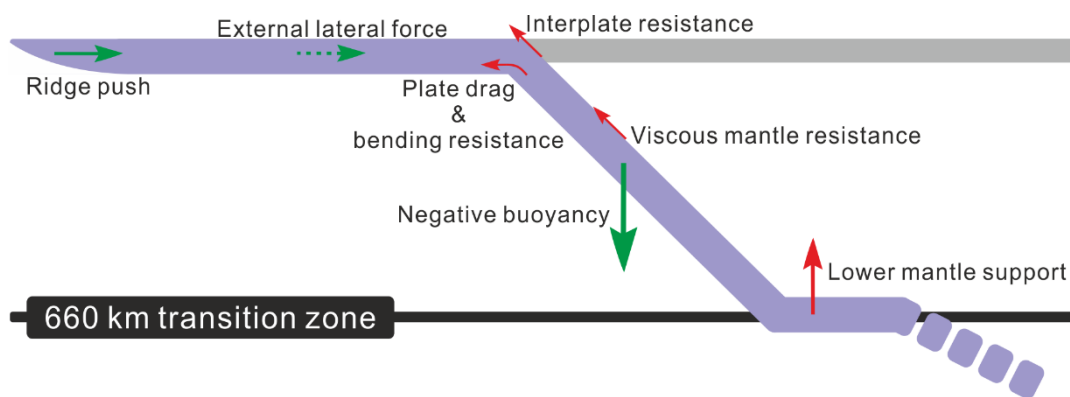
Figure 1.1 Force analysis of the sinking slab in the upper mantle (based on Forsyth and Uyeda, 1975; Goes et al., 2017). The green arrows are forces driving subduction, while the red arrows marks forces resisting subduction.

1.1.2   Subduction's impact upon the overriding plate

While subduction is the end of the life of an oceanic plate at the Earth's surface, it is just of start of the subducting slab's major impact in deforming the overriding plate. Research suggests that the sinking slab can pose a variety of tectonic overprints within the overriding plate extending over 1000 km away from the trench. The tectonic overprint at the surface can include creating an accretional wedge, fore-arc basin, volcanic arc, back-arc basin, intraplate volcanism, respectively as the distance away from the trench increases (Braszus et al., 2021; Chen et al., 2015; Rawlinson et al., 2017; Ruellan et al., 2003; Sternai et al., 2014; Yang et al., 2021, 2018; Yang and Faccenda, 2020). Besides, subduction can also regulate the magnitude of the plate's velocity and surface heat flow (Beniest and Schellart, 2020; He, 2015; Parsons and Sclater, 1977; Schellart et al., 2011). The deformation induced by subduction within the overriding plate consists of reshaping the stress field, triggering earthquakes at various depths, and assimilating of magmas into the overriding plate's lithosphere (Anderson et al., 2021; Baxter et al., 2020; Bevis et al., 1995; Erdős et al., 2021; Holt et al., 2015a; Kusky, 2022; Straub et al., 2020).

Among the above impacts of subduction on the overriding plate, this thesis is especially interested in the development of extensional processes. These include rifting and spreading centres in the back-arc region (Hawkins, 1995; Hoernle et al., 2021; Parson and Wright, 1996; Schliffke et al., 2022; Toksöz and Hsui, 1978), extension in continental marginal basins (Chekhovich et al., 2012; Lallemand and Jolivet, 1986; Schellart, 2017; Sleep and Toksöz, 1971; Toksöz and Hsui, 1978), increasing heat flow (Beniest and Schellart, 2020; Čížková and Bina, 2015; Parson and Wright, 1996; Sleep and Toksöz, 1971), and continental break-up (Dal Zilio et al., 2018; East et al., 2020; Ren et al., 2020; Zhang et al., 2018). It is to be noted, that not all these extensional processes are always active during subduction. For example, the Japan Sea and the Bristol Bay Basin (Alaska) have ceased extension even though subduction is still active (Morishita et al., 2020; Walker et al., 2003).

1.2   Knowledge gaps and research plan

The self-driven oceanic subduction can be decomposed into three major participants: the subducting oceanic plate, the overriding plate, and the convective mantle wedge flow. The net negative buoyancy of the subducting slab is the "engine" to provide the source of energy for the subduction system. While the mantle wedge flow is the medium to transfer the sinking slab's impact upon the overriding plate. In brief, the observed overriding plate deformation is the result of all these components exchanging energy and material with each other. To understand the driving mechanism of the deformation patterns observed in subduction zones, abundant research has been conducted in analysing the role of each component. This thesis investigates three aspects which can influence the deformation patterns observed within the overriding plate.

1.2.1 Trench retreat and back-arc extension

Back-arc extension is widespread in modern subduction zone system (Ewart et al., 1998; Heuret and Lallemand, 2005; Lallemand and Jolivet, 1986; Liu et al., 2017; Schellart et al., 2008; Schliffke et al., 2022; Sleep and Toksöz, 1971; Uyeda, 1981; Walker et al., 2003), and it plays a significant role in producing geohazards, e.g., volcanic eruption, earthquakes (Kósik et al., 2020; Kusky, 2022) and generating resources, e.g., hydrocarbon, sulfide deposits, manganese crusts (Fouquet et al., 1991; Hessler and Sharman, 2018; Miller et al., 2018). However, the underlying driving mechanism to initiate back-arc extension is still debated.

Generally, two types of driving mechanisms accounting for back-arc extension has been proposed: 1) mechanism that addresses the role of shear basal traction induced by mantle wedge flow (Figure 1.2), e.g., trench-ward wedge flow (e.g., Chen et al., 2016; Erdős et al., 2021; Husson, 2012; Sleep and Toksöz, 1971; Suchoy et al., 2021), toroidal wedge flow (Schellart and Moresi, 2013), divergent upwelling mantle flow (Dal Zilio et al., 2018; Yang et al., 2019), gravitational instability of mantle lithosphere induced by the wedge flow (Currie et al., 2008), thermal erosion by mantle wedge flow (He, 2014; Le Voci et al., 2014); 2) mechanism that do not necessarily need mantle flow to initiate back-arc extension, e.g., trench suction (Elsasser, 1971).

Both numerical and analogue modelling results indicate that the overriding plate close to the trench develops compressional stress instead of tensile stress, excluding the effect of trench suction during subduction (e.g., Alsaif et al., 2020; Chen et al., 2016; Schellart and Moresi, 2013). As for the various mechanisms that involves mantle wedge flow, it is still debated which one plays the dominant role. Recent studies suggest that divergent mantle wedge flow is more likely to emerge in regions that develop whole mantle convection (Dal Zilio et al., 2018; Yang et al., 2019), while the

trench-ward component can solely induce back-arc extension when wedge flow is confined in the upper mantle (Chen et al., 2016; Erdős et al., 2021; Sleep and Toksöz, 1971; Suchoy et al., 2021). Gravitational instability (Currie et al., 2008; Davies et al., 2016; Le Voci et al., 2014) and thermal erosion (Davies et al., 2016; He, 2014; Le Voci et al., 2014) is likely to significantly reduce the thickness of the overriding plate provided that the mantle lithosphere is hotter, weaker, or wetter than average, the origin of which is unresolved. Two simulation assumptions are usually proposed to induce back-arc extension in previous research: a) fixed side boundary condition that inhibits mobility of the overriding plate as trench retreats (Capitanio et al., 2010; Gerya et al., 2008; Hertgen et al., 2020; Nakakuki and Mura, 2013); b) pre-weakened overriding plate rheology that allows the lithosphere to deform more easily during subduction (Capitanio et al., 2010; Currie et al., 2008; He, 2014; Yang et al., 2019). These assumptions limit the current understanding as it skips answering how the overriding plate gets weakened or become immobile before back-arc extension initiates, for which rigorous investigation is needed.
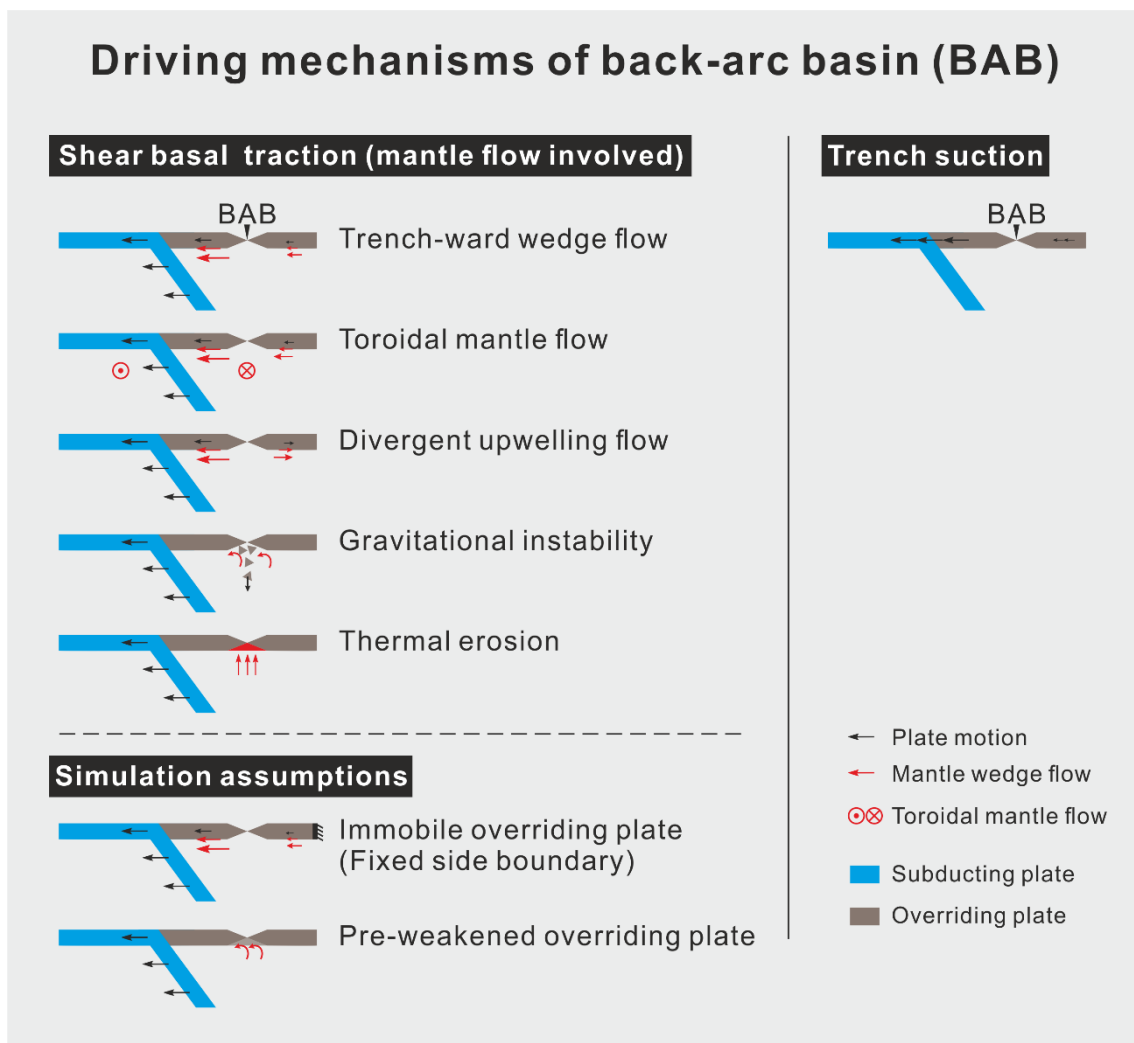
Figure 1.2 Review of driving mechanisms accounting for back-arc extension (basin) during subduction.

Observation presently show that trench retreat dominates trench advance, with 61.9-77.9% of all trenches retreating, irrespective of the adopted frame of references (Schellart et al., 2008). In addition, a fast retreating trench correlates well with the existence of back-arc extension (Figure 1.3, a), except for some cases where the trench retreat rate is lower than 5 cm/yr (Heuret and Lallemand, 2005; Schellart, 2008). A simplified conceptional model is built to explain the formation of back-arc basin as a function of the mobility of the trench and overriding plate relative to each other (Figure 1.3, b, Faccenna et al., 2021). In this diagram, back-arc develops when the trench moves away from the overriding plate, and compressional units will develop when

trench and overriding plate move against with each other. The model helps to explain the general dynamics in the back-arc region. However, it fails to explain why extension develops in the back-arc region instead of fore-arc region. Also, the origin of why plates achieve different velocity states is unclear. In brief, there is still great uncertainty in terms of how a high trench retreat rate relates to the extensional back-arc region, and what is the driving mechanism.
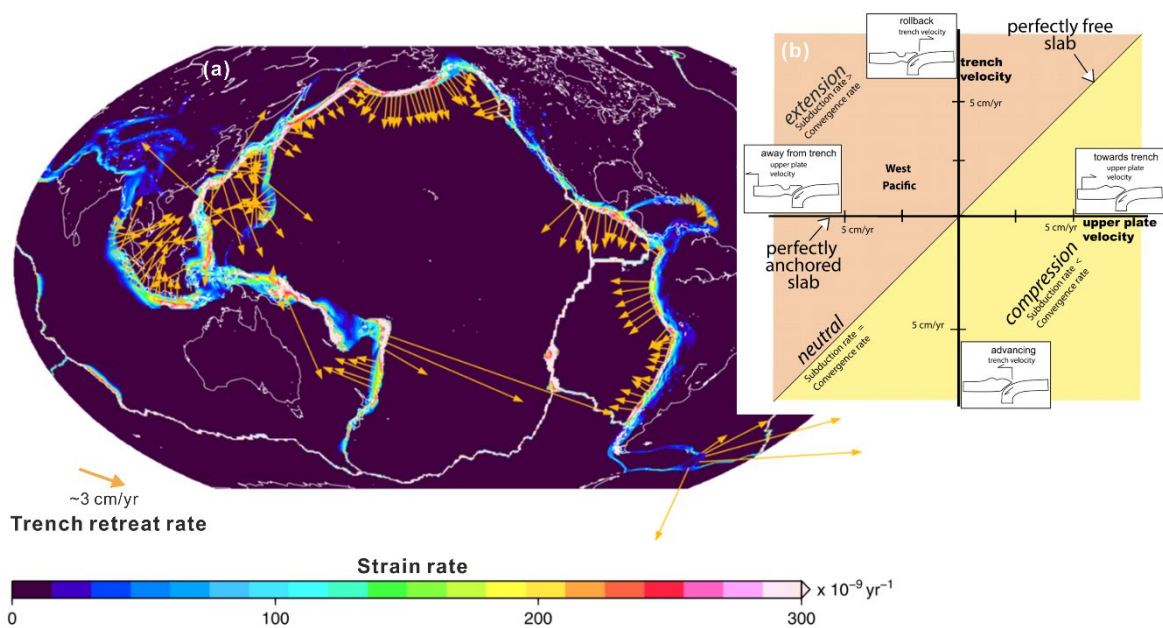
Figure 1.3 Theoretical model and observation of subduction zone deformation's correlation with trench mobility. (a) World map of trench retreat rate and strain rate in subduction zones (adapted from Husson, 2012) (b) Regime diagram of deformation patterns as a function of trench and overriding plate mobility (adapted from Faccenna et al., 2021).

To summarise, rigorous investigation has not been done yet on the trench retreat rate's role in initiating different extents of back-arc extension, especially within a mobile and homogeneous overriding plate. In Chapter 3, a series of 2-D thermo-mechanical and self-consistently driven models are run with a mobile overriding plate in set-ups that lead to a wide range of trench retreat rate. The role of high trench retreat rate in

generating different extents of extension in the back-arc region of a homogeneous and mobile overriding plate is tested.

1.2.2 Multiple slab interaction

Most subduction zones involve only one subducting slab. Multiple subduction zones, i.e., one overriding plate interacting with more than one subducting slab, is receiving growing attention from the community as its role in deforming the overriding plate has been overlooked due to the limited number of examples in the modern tectonic framework. The increasing precision of plate reconstruction reveals that multiple subduction system can be widely observed in Earth's history (Butterworth et al., 2014; Hall and Spakman, 2015; Matthews et al., 2016; Navarrete et al., 2019; Santosh, 2010; Vaes et al., 2019; Van Benthem et al., 2013; Wang et al., 2021; Windley et al., 2010; Young et al., 2019). Multiple subduction zones can be classified in four basic endmembers based on the spatial orientation of slabs relative to each other or the overriding plate, i.e., inward-dipping, same-dip, outward-dipping and oppositely dipping adjacent subduction zones (Figure 1.4). The investigation on the slab-slab interaction and slab-overriding plate interaction shows that the complex system can regulate the stress state, plate motion rate, deformation patterns, surface topography etc. within the overriding plate by inducing complex mantle flow patterns (Dasgupta and Mandal, 2018; Faccenna et al., 2018; Holt et al., 2017; Jagoutz et al., 2015; Király et al., 2021, 2018; Lyu et al., 2019; Pusok and Stegman, 2020).
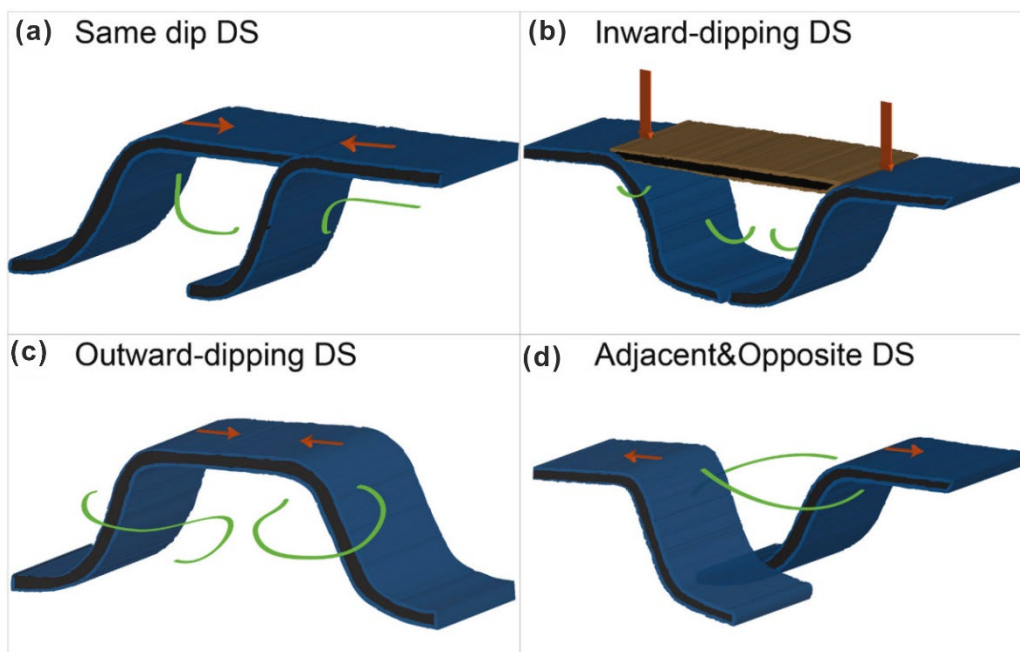
Figure 1.4 Basic endmembers of multiple subduction zone systems (adapted from Király et al., 2021). DS is short for double subduction.

Despite these improved observations and preliminary investigations, the multiple subduction system is still poorly understood in terms of how it differs from single sided subduction in deforming or weakening the overriding plate. In addition, there is limited understanding of whether the parameters that have been tested in single sided subduction systems will play the same role in multiple subduction systems.

To fill in some of the knowledge gaps, Chapter 4 investigates the dynamic evolution of dual inward dipping subduction or bi-vergent subduction, which occurs when the overriding plate is decoupled with two subducting slabs dipping towards each other. In particular, a series of 2-D thermo-mechanical numerical models are conducted to investigate how dual inward dipping subduction modifies the rheological structure of the overriding plate.

1.2.3 The role of the overriding plate

Various characteristics of the oceanic subducting plate, e.g., its age, slab dip, crust thickness, dehydration process, rigidity, geochemical heterogeneity, fabric orientation, velocity, gravity anomaly, sediment thickness, and the number of slabs are commonly cited as important properties governing the slab geometry, mantle wedge flow patterns, slab stress state, deformation patterns, dynamics, mantle wedge melting degree, and hazard potential in subduction zones (Bassett and Watts, 2015; Becker and Faccenna, 2009; Billen and Hirth, 2007; Cross et al., 1982; Heuret and Lallemand, 2005; Király et al., 2018; Kusky, 2022; Lallemand et al., 2005; Leat et al., 2000; Schellart, 2007; Timm et al., 2013).

Yet, the role of the overriding plate's properties in influencing the deformation patterns has been overlooked relative to the subducting plate for a long time. Existing research shows that the overriding plate's age, thickness, geometry, velocity boundary condition, rheology, can efficiently affect the trench motion, slab morphology in the mantle, tendency to form back-arc extension, and jumping of back-arc extension centre during subduction (Butterworth et al., 2012; Garel et al., 2014; Hertgen et al., 2020; Holt et al., 2015b; Meyer and Schellart, 2013; Rodríguez-González et al., 2014; Schellart, 2008; Schliffke et al., 2022; Sharples et al., 2014; van Dinther et al., 2010). Despite these pioneering investigations, the overriding plate's controls on its resulting deformation are still much less explored than that of the subducting plate.

Most previous investigations consider an overriding plate with a constant thickness and homogeneous thermal structure away from the trench. In reality, the thickness of the overriding plate is often spatially heterogeneous (Steinberger and Becker, 2018). In addition, the overriding plate can be an oceanic plate or a continental plate, and sometimes a combination of both plates, e.g., Japan subduction zone, Aleutian

subduction zone, both of which developed a marginal basin in the back-arc region and where the extension is now inactive (Jolivet et al., 1994; Walker et al., 2003). However, the role of a mixed overriding plate with both oceanic plate and the continental plate has not been rigorously tested.

In Chapter 5, the overriding plate is configured as a combination of both oceanic plate and a continental block. Its role in deciding the critical condition to initiate marginal extension and where an extension centre will develop is investigated.

1.3 Aims and objectives

In general, this thesis investigates what role high trench retreat, multiple slab interaction and heterogeneity of overriding plate may play in controlling different deformation patterns, especially the extensional tectonic processes, observed within the overriding plate. Also, the critical condition and driving mechanisms to initiate different extents of extension in the overriding plate will be addressed. In the end, the goal is to build a framework which could potentially improve the understanding of deformation patterns of the overriding plate observed during subduction processes.

This thesis will be using numerical methods rather than analogue models. Numerical modelling has the advantage of running multiple series of models at the same time, it is possible to investigate a range of processes, and one can access all the variables in the solution domain during the post-processing period. The alternative method of using analogue experiments to investigate dynamics has other benefits, but it can be difficult to completely mimic the Earth and access all the variables throughout the domain. Throughout the thesis the code Fluidity is used. In the next chapter I introduce this numerical method.

Chapter 2 Methods

The investigations in this thesis have been undertaken using numerical modelling. The models have been two dimensional. The computational modelling framework Fluidity (Davies et al., 2011; Kramer et al., 2021, 2012), a finite-element, control-volume code has been used. The temperature and mantle flow velocity is modelled by solving the coupled incompressible Stokes and energy equations in the Boussinesq approximation using Fluidity.

2.1   Governing equations

Under the Boussinesq approximation (McKenzie et al., 1974), the equations governing the thermally driven subduction process are derived from conservation of mass, momentum, and energy, for an incompressible Stokes flow

$$\partial_i u_i = 0, \qquad (2.1)$$

$$\partial_i \sigma_{ij} = -\Delta \rho g_j, \qquad (2.2)$$

$$\frac{\partial T}{\partial t} + u_i \partial_i T = \kappa \partial_i^2 T, \qquad (2.3)$$

in which u, g, σ, T, κ are the velocity, gravity, stress, temperature, and thermal diffusivity, respectively (Table 2.1). In particular, the full stress tensor σ_{ij} consists of deviatoric and lithostatic components via

$$\sigma_{ij} = \tau_{ij} - p\delta_{ij}, \qquad (2.4)$$

where τ_{ij} represents the deviatoric stress tensor, p the dynamic pressure, and δ_{ij} the Kronecker delta function. The deviatoric stress tensor and strain rate tensor $\dot{\varepsilon}_{ij}$ are related according to

$$\tau_{ij} = 2\mu\dot{\varepsilon}_{ij} = \mu\big(\partial_j u_i + \partial_i u_j\big), \tag{2.5}$$

with μ the viscosity. The density difference due to temperature is defined as

$$\Delta\rho = -\alpha\rho_s(T - T_s), \tag{2.6}$$

where α is the coefficient of thermal expansion, ρ_s is the reference density at the surface temperature T_s (Table 2.1).

Table 2.1 Key parameters used in this thesis.

Quantity	Symbol	Units	Value
Gravity	g	$m\ s^{-2}$	9.8
Gas constant	R	$J\ K^{-1}\ mol^{-1}$	8.3145
Mantle geothermal gradient	G	$K\ km^{-1}$	0.5 (UM) 0.3 (LM)
Thermal expansivity coefficient	α	K^{-1}	3×10^{-5}
Thermal diffusivity	κ	$m^2\ s^{-1}$	10^{-6}
Reference density	ρ_s	$kg\ m^{-3}$	3300
Cold, surface temperature	T_s	K	273
Hot, mantle temperature	T_m	K	1573
Maximum viscosity	μ_{max}	$Pa \cdot s$	10^{25}
Minimum viscosity	μ_{min}	$Pa \cdot s$	10^{18}
Diffusion Creep[a]			
Activation energy	E	$kJ\ mol^{-1}$	300 (UM) 200 (LM)
Activation volume	V	$cm^3\ mol^{-1}$	4 (UM) 1.5 (LM)
Prefactor	A	$Pa^{-n}\ s^{-1}$	3.0×10^{-11} (UM) 6.0×10^{-17} (LM)
	n		1
Dislocation Creep (UM)[b]			
Activation energy	E	$kJ\ mol^{-1}$	540
Activation volume	V	$cm^3\ mol^{-1}$	12
Prefactor	A	$Pa^{-n}\ s^{-1}$	5.0×10^{-16}
	n		3.5
Peierls Creep (UM)[c]			
Activation energy	E	$kJ\ mol^{-1}$	540
Activation volume	V	$cm^3\ mol^{-1}$	10
Prefactor	A	$Pa^{-n}\ s^{-1}$	10^{-150}
	n		20
Yield Strength Law[d]			
Surface yield strength	τ_0	MPa	2
Friction coefficient	f_c		0.2
	$f_{c,weak}$		0.02 (weak layer)
Maximum yield strength	$\tau_{y,max}$	MPa	10,000

a The rheology parameter of diffusion creep is guided by previous mineral deformation experiments (Hirth and Kohlstedt, 2003, 1995a; Ranalli, 1995). The UM and LM stands for "upper mantle" and "lower mantle," respectively. b The activation parameters and stress-dependent exponent used for dislocation creep are in agreement with previous mineral deformation experiments (Hirth and Kohlstedt, 1995b). c The parameterisation (based on Kameyama et al., 1999) makes Peierls creep tend to be weaker than yielding in the upper mantle, thus enabling trench retreat and creating richer slab morphology in the upper mantle (Garel et al., 2014). d A very high maximum yield strength value is used here to ensure that yielding only dominates at the depth of crustal scale. A friction coefficient of 0.2 is following numerical models (Garel et al., 2014; Gülcher et al., 2020), and it is intermediate between lower values of previous subduction models (Crameri et al., 2012; Di Giuseppe et al., 2008) and the actual friction coefficient of the Byerlee law (Byerlee, 1978).

2.2 Rheology

2.2.1 Deformation mechanisms

The governing rheological laws are identical throughout the model domain. In detail, a uniform composite viscosity is used to take account of four deformation mechanisms under different temperature-pressure conditions: diffusion creep, dislocation creep, Peierls mechanism, and yielding (Garel et al., 2014). The effective composite viscosity in the computational domain is given by

$$\mu_{eff} = \left(\frac{1}{\mu_{diff}} + \frac{1}{\mu_{disl}} + \frac{1}{\mu_P} + \frac{1}{\mu_y} \right)^{-1}, \qquad (2.7)$$

where μ_{diff}, μ_{disl}, μ_y define the creep viscosity following

$$\mu_{diff/disl/P} = A^{-\frac{1}{n}} exp \left(\frac{E + PV}{nRT_r} \right) \dot{\varepsilon}_{II}^{\frac{1-n}{n}}, \qquad (2.8)$$

in which A is a prefactor, n the stress component, E the activation energy, P the lithostatic pressure, V the volume, R the gas constant, T_r the temperature obtained by adding an adiabatic gradient of 0.5 K/km in the upper mantle and 0.3 K/km in the lower mantle to the Boussinesq solution (Fowler, 2005), $\dot{\varepsilon}_{II}$ the second invariant of the strain rate tensor. While the fourth deformation mechanism, yielding, is defined by a brittle-failure type yield-stress law as

$$\mu_y = \frac{\tau_y}{2\dot{\varepsilon}_{II}}, \qquad (2.9)$$

with μ_y the yielding viscosity and τ_y the yield strength. τ_y is determined by

$$\tau_y = min(\tau_0 + f_c P, \tau_{y,max}), \qquad (2.10)$$

with τ_0 the surface yield strength, f_c the friction coefficient, P the lithostatic pressure, and $\tau_{y,max}$ the maximum yield strength (Table 2.1). Note there is a layer of weak zone lying on top of the subducting plate. The weak layer shares the same rheology, except that its value of f_c is one tenth, and its maximum viscosity is 10^{20} Pa s. It is noted that for all models in this thesis there is no arbitrary weak zone emplaced in the initial overriding plate.

2.2.2   Viscosity dependency analysis

As rheology laws suggest, the four types of deformation mechanisms may yield viscosity that depends on multiple variables, e.g., temperature, static pressure (depth) and strain rate. The contour map of viscosity yielded by individual deformation mechanism shows that there is decreasing dependency on strain rate and increasing sensitivity to temperature for yielding, Peierls creep, dislocation creep and diffusion creep (Figure 2.1).
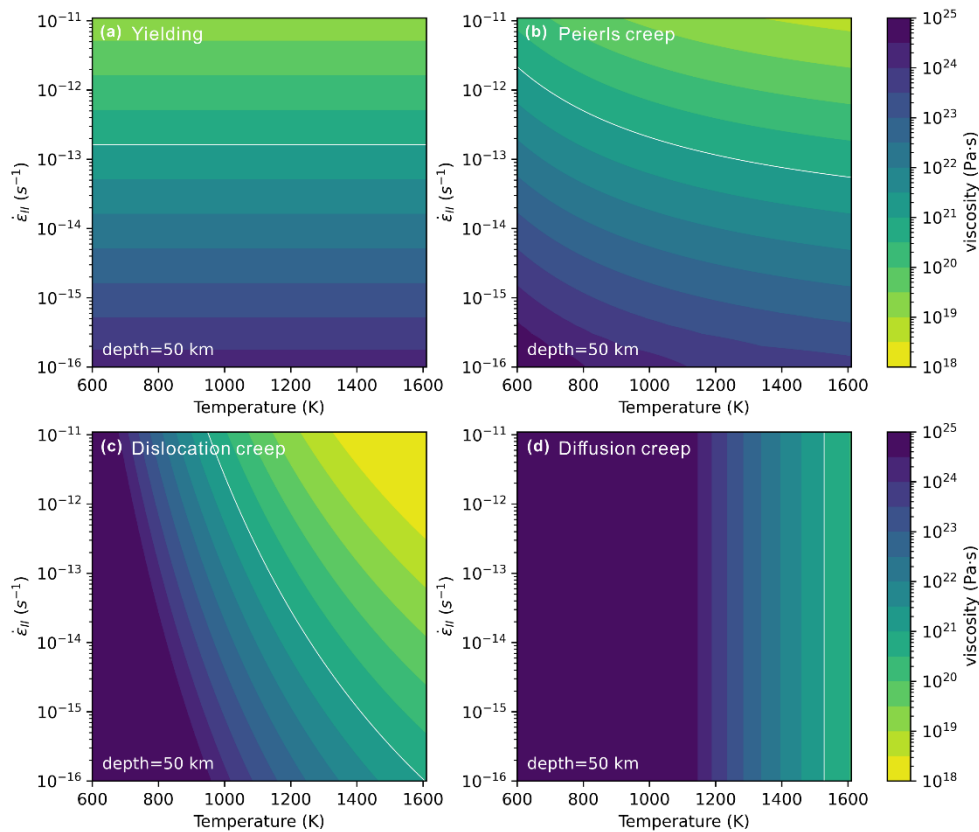
Figure 2.1 The composite viscosity contour map as a function of temperature and stain rate at the depth of 50 km. The while contour line marks the viscosity of $10^{21}\ Pa \cdot s$.

Combining these four types of deformation mechanism yields the effective viscosity (Equation 2.7). The dominant deformation mechanism (DDM) is defined as the composite rheology law that yields the minimum viscosity, which decides the magnitude of the effective viscosity. During simulation, the DDM may vary at different temperature, strain rate and depth, so the effective viscosity can be partitioned into different domains (Figure 2.2, a-c). The DDM evolution throughout the simulation may help improve the understanding of each deformation mechanism's contribution to deforming the overriding plate. This DDM analysis method introduced here has rarely been used before though composite rheology has become so widely applied. Also, this method can be a powerful tool to understand other strain localisation processes, e.g., formation of plate boundaries.
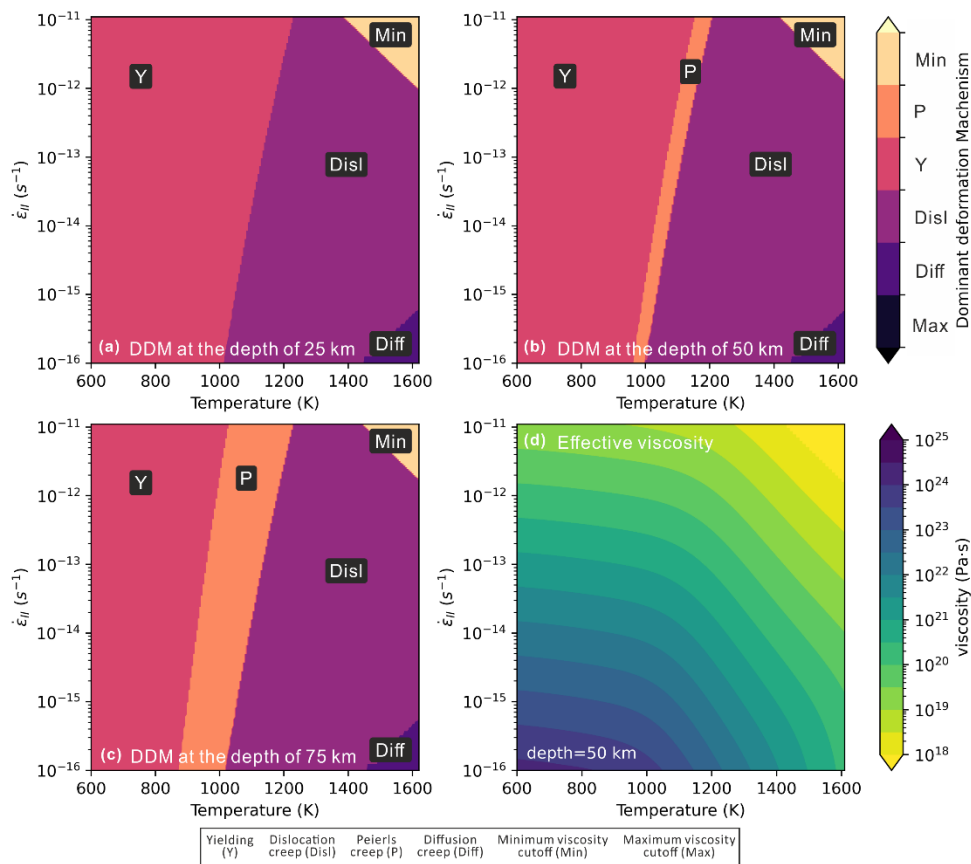
Figure 2.2 The effective viscosity contour map and partition of the dominant deformation mechanism (DDM).

2.3   Fluidity: the simulation code

In order to simulate dynamic subduction, the thermos-mechanical approach utilised here requires (i) extreme local resolution; (ii) solvers that can efficiently handle the sharp viscosity contrasts that arise during the simulation, and (iii) free mobile trench.

The computational modelling framework Fluidity (Davies et al., 2011; Kramer et al., 2021, 2012), a finite-element, control-volume code has been used. It uses an unstructured discretisation and a powerful and flexible grid adaptivity. Mesh size optimisation is set up to be controlled by a metric that depends on the magnitude of velocity, viscosity, temperature and material volume fraction, which is used to track

the interface between different materials used. The adaptive mesh allows features as small as 0.4 km to be tracked and resolved in this thesis.

The solution strategies used to solve the discretized form of equations (2.1) and (2.2) are identical to those outlined in Davies et al. (2011), with the addition of a modification to incorporate an implicit treatment of the free-surface boundary condition (Kramer et al., 2012), which facilitates the trench mobility. Equation (2.3) is discretized using finite volumes, constructed around the vertices of the triangular finite element mesh (Davies et al., 2011).

Fluidity has been extensively validated and applied to investigate various geodynamic problems, ranging from subduction process, pluming events, intraplate magmatism, dynamic topography, and overriding plate deformation, against a range of analytical and benchmark solutions (Alsaif et al., 2020; Beall et al., 2021; Davies et al., 2019, 2016, 2011; Duvernay et al., 2021; Garel et al., 2020, 2014; Jones et al., 2016; Kramer et al., 2012, 2021; Le Voci et al., 2014; Maunder et al., 2020; Perrin et al., 2018; Suchoy et al., 2021; Tosi et al., 2015).

The model setup of this thesis builds upon Garel et el. (2014). Multiple series of 2-D thermally driven subduction models are undertaken to investigate the role of a variety of tectonic setups in affecting the deformation patterns observed within the overriding plate. Throughout the thesis, two types of material are introduced, the weak layer and the normal material. The weak layer tops the surface of the subducting plate and it decouples the subducting plate from the overriding plate. Both types of material share a uniform rheology law, with just the parameter values for the friction coefficient and the maximum viscosity differing from each other (Table 2.1).

To be noted, all the models conducted have been two dimensional, which is much more efficient to run and process than three dimensional models, but at the cost of neglecting 3D effects during the subduction process, e.g., toroidal component of mantle wedge flow. This can form a substantial limitation when trying to match the results with real-world observations in subduction zones, and it has been cautiously evaluated and justified for the potential impact in each of the following chapters.

The detailed model geometry and boundary conditions will be introduced in each of the following three main chapters. The next chapter considers the reference case of single sided subduction beneath a homogeneous overriding plate.

Chapter 3 Impact of trench retreat rate on initiating focused back-arc extension within a mobile overriding plate

3.1 Introduction

The horizontal extension observed within the overriding plate in different subduction zones varies, especially in the back-arc. The extension ranges from inactive extension with high heat flow, e.g. Southeast Aleutian Basin (Christeson and Barth, 2015), to a rifting ridge with thinning lithosphere, e.g. Central Andaman Basin, Taupo Volcanic Zone (Morley and Alvey, 2015; Parson and Wright, 1996), and further extended to the opening of a new oceanic floor, e.g. Sea of Japan, Lau Basin (Jolivet et al., 1994; Taylor et al., 1996). The extension plays a significant role in producing hazards , e.g., volcanic eruption, earthquakes (Kósik et al., 2020; Kusky, 2022) and generating resources, e.g., hydrocarbon, sulfide deposits, manganese crusts (Fouquet et al., 1991; Hessler and Sharman, 2018; Miller et al., 2018). However, the underlying driving mechanism to initiate the extension remains debated.

Observation of plate and trench motion shows that retreating trench correlates well with the existence of back-arc extension except for some cases where trench retreat rate is lower than 5 cm/yr (Heuret and Lallemand, 2005; Schellart et al., 2008). A general explanation for this correlation is that the overriding plate extends to accommodate the void that trench retreat leaves. In detail, two driving mechanisms have been proposed: trench retreat generates strong convection currents (poloidal and toroidal flow) that transmits non-uniform basal traction upon the overriding plate (Sleep and Toksöz, 1971); and trench suction at the subduction zone interface pulls the overriding plate (Elsasser, 1971).

Further observations of subducting systems with a high trench retreat rate shows that a localised extension often develops in the overriding plate. For example, the trench retreat rate at Tonga is ~16 cm/yr where spreading ridge and opening seafloor is observed (Bevis et al., 1995). The correlation is supported by numerical and analogue investigations. Both trench retreat induced poloidal and toroidal flow components show a positive correlation with trench retreat rate (Funiciello et al., 2004; Stegman et al., 2006). Models with a higher trench retreat rate also correlate with higher strain rate in the overriding plate (Holt et al., 2015a; Meyer and Schellart, 2013).On the other hand, previous research indicates that the trailing boundary condition and heterogeneity of the overriding plate also play important roles in affecting the degree of back-arc extension. Models with either a fixed overriding plate or an overriding plate containing an arbitrary weak zone are prone to produce rifting or spreading back-arc extension (Capitanio et al., 2010; Gerya et al., 2008; Hertgen et al., 2020; Nakakuki and Mura, 2013; Yang et al., 2019), while studies with a mobile and homogeneous (without an arbitrary weak zone) overriding plate often fail to produce an opening back-arc incorporating focused thinning lithosphere (Chen et al., 2016; Čížková and Bina, 2013; Schellart and Moresi, 2013). To summarise, rigorous investigation has not been done yet on the trench retreat rate's role in initiating different extents of back-arc extension, especially within a mobile and homogeneous overriding plate.

In this research, a series of 2-D thermo-mechanical and self-consistently driven models are run with a mobile overriding plate in set-ups that lead to a wide range of trench retreat rate. The results produced three different types of localised back-arc stretching states as the trench retreat rate increases: i) minor extension with observable but not significant thinning of the thermal lithosphere; ii) rifting extension with hot mantle thermally intruded upward to the surface; iii) new spreading seafloor with thin lithosphere. It is found that a minimum trench retreat rate is needed to initiate

rifting extension in the back-arc. The extension is driven by the non-uniform basal drag of the trenchward mantle wedge flow due to rapid trench retreat.

3.2 Methods

Extending the model setup of Garel et el. (2014), this chapter tests a series of 2-D thermally-driven subduction models using the code Fluidity (Davies et al., 2011; Kramer et al., 2012), a finite-element control-volume computational modelling framework, with an adaptive mesh that can capture evolving changes with a maximum resolution of 0.4 km. To obtain a wide range of trench retreat rate for a mobile overriding plate, the initial age of the subducting plate is varied at the trench.

3.2.1 Model setup

Following Garel et al., 2014, this chapter runs spatially large models where the computational domain is 10000 km by 2900 km, with x (width) coordinates and z (depth) coordinates extending from the surface to the bottom of the lower mantle. Such a wide domain reduces the influence of side and bottom boundary conditions (Chertova et al., 2012). The thermal boundary conditions at the surface and bottom are defined by two isothermal values: $T = T_s$ and $T = T_m$ for surface and base of lower mantle respectively, while the sidewalls are insulating. As for velocity boundary conditions, a free-surface is applied at the top boundary to enable trench mobility, while the other boundaries are free-slip.

Age_{SP}^0 and Age_{OP}^0 represent the initial ages of subducting plate and overriding plate at the trench, which starts in the middle of the surface. Laterally on the surface, the age of both plates increases linearly with its distance away from the mid-ocean ridge on

either side. While vertically, the age of plate at surface defines the initial thermal structure through a half-space cooling model (Turcotte and Schubert, 2014),

$$T(x,z) = T_s + (T_m - T_s)erf\left(\frac{z}{2\sqrt{\kappa Age^0(x)}}\right), \tag{3.1}$$

with x the distance away from the mid-ocean ridge, z the depth, κ the thermal diffusivity. The thermal lithosphere is defined as the material colder than 1300 K.

The free surface boundary condition together with the mid-ocean ridge setup allow the subducting slab, overriding plate and trench to move freely as subduction evolves. To allow for a self-driven subduction without implementing external forces, the subducting plate is set up with a bend into the mantle and a 5 km thick low-viscosity decoupling layer on the top. The initial bending radius is 250 km and the slab bends over 77 degrees from the trench (Figure 3.1).
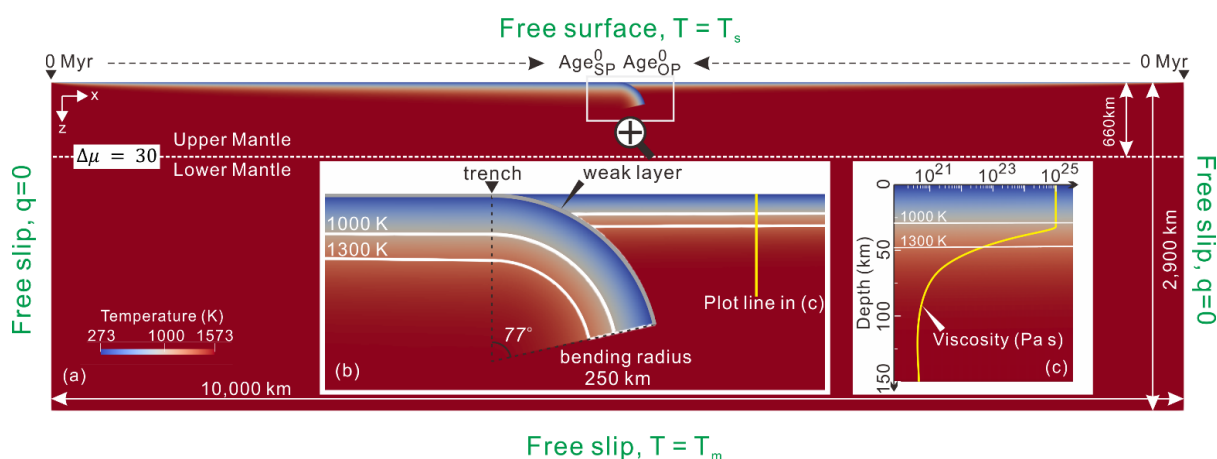
Figure 3.1 Model geometry and initial setup illustrated with the initial temperature field as the background. Age_{SP}^0 and Age_{OP}^0 represent the initial ages of subducting plate and overriding plate at trench. The viscosity jump ($\Delta\mu$) between upper and lower mantle at 660km transition zone is set up with a fixed value of 30. The trench is recognised as the position where the overriding plate meets the weak layer coating the subducting plate at the surface. a) The whole computational domain. b) Enlarged area of trench zone where bending slab meets flat overriding plate. A 5 km thick weak layer is set up on top of the subducting slab to facilitate decoupling. 1100 K and 1300 K isotherms are marked in while lines. c) Vertical profile of viscosity against depth within the overriding plate. The plot line is 400 km away from the initial trench.

3.2.2   Modify the rate of trench retreat

Trench retreat rate is related to multiple factors. Numerical investigations have shown that older subducting plate or higher slab density (Alsaif et al., 2020; Garel et al., 2014), narrower trench width (Schellart et al., 2011; Stegman et al., 2006), the inclusion of overriding plate and its aspect ratio (Butterworth et al., 2012; Capitanio et al., 2010), younger overriding plate or thinner overriding plate (Garel et al., 2014; Hertgen et al., 2020), and less slab resistance to bending (Di Giuseppe et al., 2008) could all contribute to faster trench retreat. While a higher viscosity jump at the mantle transition zone (Čížková and Bina, 2013; Garel et al., 2014), and a stress-dependent mantle viscosity (Holt and Becker, 2017) could reduce the rate of trench retreat.

Of all the parameters, the plate age turns out to be a concise and efficient parameter to obtain a wide range of trench retreat rates by modifying the initial plate ages (Age_{SP}^0 and Age_{OP}^0) at the trench (Table 3.1). This can vary the net negative buoyancy of the sinking slab and determines the maximum trench retreat rate potential during subduction. Meanwhile, several diagnostics were used to monitor the trench motion during the 10 Myr long simulations. Two series of models, each series with the same Age_{OP}^0 and a growing Age_{SP}^0, are simulated to demonstrate the role trench retreat rate may play in generating different extent of localised extension in the back-arc region.

Table 3.1 List of representative models with key variables governing trench retreat rate and diagnostics monitoring the trench motion and stretching state of the overriding plate.

Model name	Age_{SP}^0 (Myr)	Age_{OP}^0 (Myr)	H_{SP}^0 (km)	H_{OP}^0 (km)	t_{660} (Myr)	$\left|\triangle x_{trench}^{0-t_{660}}\right|$ (km)	$\left|u_{max}^{0-t_{660}}\right|$ (cm/yr)	$\left|\overline{u_{trench}^{0-t_{660}}}\right|$ (cm/yr)	Back-arc stretching state
SP80_OP20	80	20	89	45	3.8	138	11	3.6	i
SP90_OP20	90	20	94	45	3.5	160	14	4.6	i
SP100_OP20	100	20	100	45	3.2	200	19	6.3	ii
SP125_OP20	125	20	111	45	2.8	340	65	12.1	iii
SP150_OP20	150	20	122	45	2.5	390	113	15.6	iii
SP100_OP25	100	25	100	50	4.1	145	10	3.5	i
SP125_OP25	125	25	111	50	3.7	168	14	4.5	i
SP150_OP25	150	25	122	50	3.5	200	20	5.7	i
SP175_OP25	175	25	132	50	3.3	250	27	7.6	ii
SP200_OP25	200	25	141	50	3.1	375	96	12.1	iii

Models are named as follows, e.g. SP80_OP20 corresponds to initial subducting plate age at the trench of 80 Myr and 20 Myr for overriding plate. H_{SP}^0 and H_{OP}^0 are the initial thermal lithosphere thickness, marked by 1300 K isotherm, of the subducting plate and overriding plate at trench separately. t_{660} equals how much time the subducting plate takes to sink to 660km depth. $\left|\triangle x_{trench}^{0-t_{660}}\right|$ is the total trench retreat in the period of t_{660}. $\left|u_{max}^{0-t_{660}}\right|$ and $\left|\overline{u_{trench}^{0-t_{660}}}\right|$ are the magnitude of maximum and average trench retreat rate recorded during t_{660}. The code i, ii and iii describing the back-arc stretching state of the overriding plate represents minor extension, rifting and new spreading seafloor, respectively.

With a wide range of trench retreat rates achieved, it is possible to investigate its influence on the formation of different extents of extension within the overriding plate.

3.3 Results

3.3.1 Trench retreat rate through time

Self-consistent subduction, in most numerical and analogue models, starts with a non-steady state where negative buoyancy pulls the slab into the deeper mantle (Capitanio et al., 2010; Gerya et al., 2008; Schellart and Moresi, 2013). Meanwhile, trench retreat accelerates with time and reaches a maximum value ($u_{max}^{0-t_{660}}$) when the slab starts to interact with the lower mantle at t_{660} (Figure 3.2,a). During the interaction, the viscosity jump at ~660 km provides a balanced competing upward support to the sinking slab, as a result the trench retreat experiences an abrupt deceleration due to the reducing slab pull force. After this short period of adjustment, subduction enters the second stage, a near steady state where trench retreat rate keeps a constant magnitude at ~ 3 cm/yr for all the models.
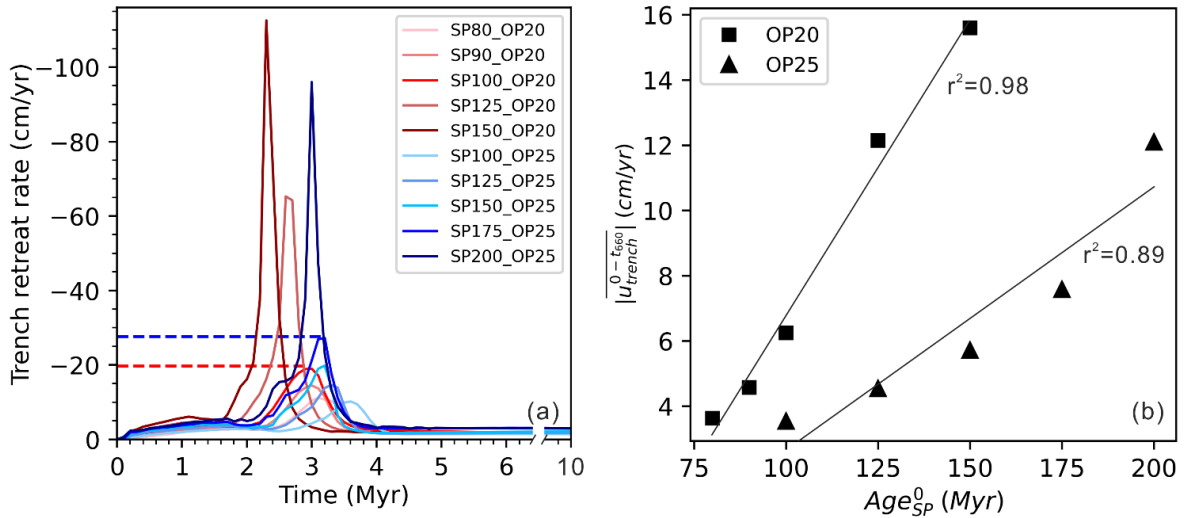
Figure 3.2 The motion of the trench through time and its Age_{OP}^{0} dependency during non-steady state subduction. a) Trench retreat rate through time. Negative value means that the trench is moving towards the subducting plate. The dashed lines of red and blue marks the $u_{max}^{0-t_{660}}$ for model SP100_OP20 and SP175_OP25 separately. b) Slab age dependency of diagnostic $\overline{|u_{trench}^{0-t_{660}}|}$ during non-steady state subduction.

For models with the same overriding plate, the average trench retreat rate over the first stage ($\left|\overline{u_{trench}^{0-t_{660}}}\right|$) is Age_{SP}^0-dependent during non-steady state subduction (Figure 3.2, b). However, this dependence fades away when the slab starts to interact with the lower mantle (Figure 3.2, a).

3.3.2 Subduction kinematics

Starting from the temporal segmentation of the subduction into non-steady and steady state subduction, this chapter investigates further to reveal more details of this model subduction system. Here using model SP175_OP25 as a case study, the whole process is characterised by illustrating the simultaneous dynamic evolution of temperature, horizontal component of the stress field, horizontal component of the velocity field, second invariant of strain rate, and magnitude of viscosity (Figure 3.3).
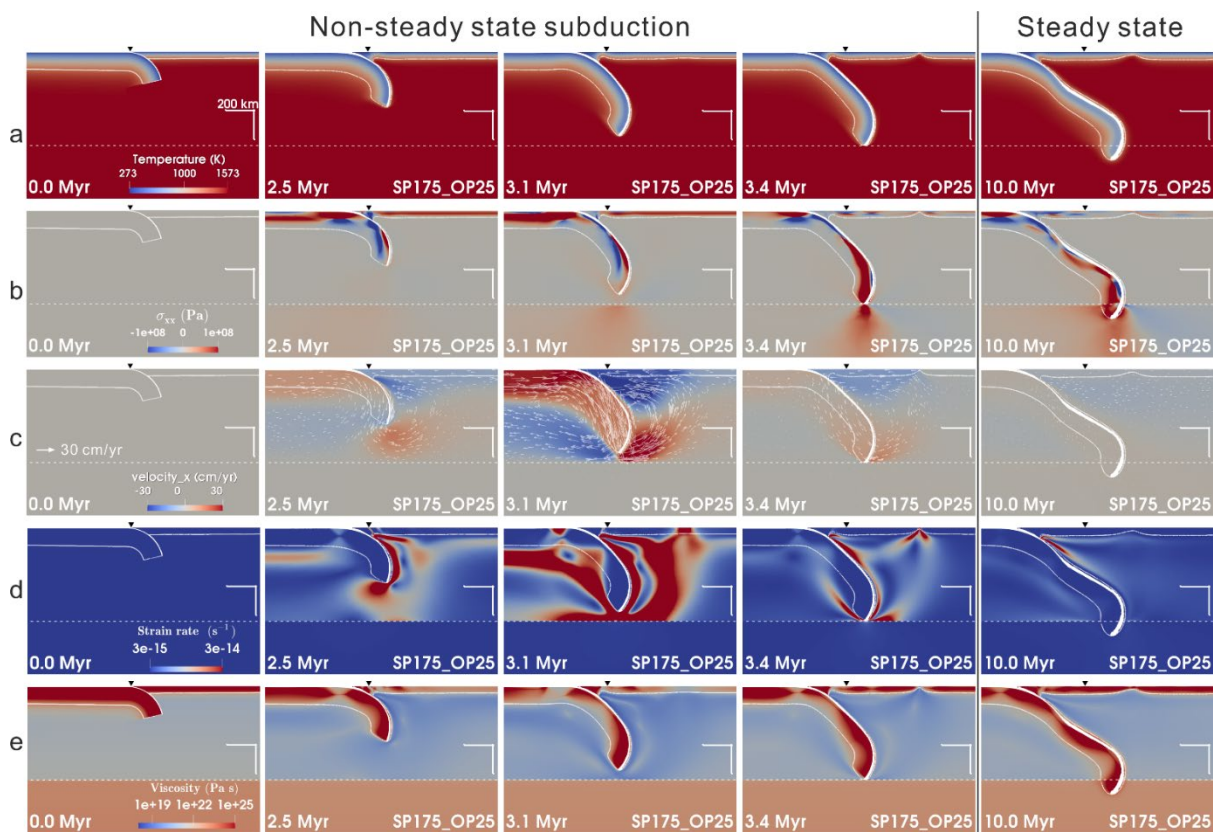
Figure 3.3 Simultaneous snapshots of a zoom-in to the region of active subduction in model SP175_OP25 showing: a) temperature, b) horizontal component of the stress field, the red area represents extension while the blue region indicates compression, c) horizontal component of velocity field superimposed with velocity vectors, d) second invariant of strain rate, e) magnitude of viscosity. The downward black triangle at the surface marks the initial location of trench. The curved white solid line underneath the plate is the 1300 K isotherm, i.e., this isotherm is taken as the bottom of the thermal lithosphere. The dashed white line marks the base of the transition zone at 660 km depth. The number with unit 'Myr' in the bottom left corner is the duration of the simulation. The right-angle scale bars above the transition zone represent 200 km in both horizontal and vertical direction.

3.3.2.1   Non-steady state subduction

Before the subducting plate starts to interact with the lower mantle around 3.3 Myr, there is localised thermal erosion in the mantle wedge (Figure 3.3, a). The horizontal component of the stress field indicates that the overriding plate portion away from the subducting plate is in a generally extensional state, leaving the portion close to the subducting plate in a general compressional stress state (Figure 3.3, b). The velocity vectors visualise a clockwise laminar mantle flow underlying the subducting plate and

an anticlockwise poloidal flow underlying the overriding plate (Figure 3.3, c). The horizontal component of velocity field within the whole overriding plate is initially consistent laterally. As the slab sinking accelerates, the trenchward velocity of the overriding plate next to the trench increases faster than the trailing part of the overriding plate. This creates an increasing horizontal velocity difference within the overriding plate. In the corresponding area, a high strain rate region (Figure 3.3, d) and low viscosity (Figure 3.3, e) region at 3.1-3.4 Myr is observed marking the initiation of the rifting within the overriding plate.

3.3.2.2 Steady state subduction

After the subducting plate reaches the lower mantle, both the mantle wedge erosion and the initiated rift cools down and the thermal thickness of the overriding plate starts to recover. The horizontal component of the stress field within the overriding plate loses the general high extensional stress state and becomes mixed with a low magnitude of both compressional and extensional stress field. The velocity field indicates that the whole system decelerates to a slow-motion mode, where plates and mantle flow move with a low uniform velocity magnitude. Meanwhile, the high strain rate vanishes in the back-arc region and it is only observed in a limited area in the mantle wedge. The viscosity field within the overriding plate also recovers its stiffness. In summary, the mobility of the whole subduction system is inhibited in this stage and tectonics within the overriding plate is relatively silent compared with the non-steady state subduction stage.

3.3.3 Three types of stretching state within the overriding plate

The case described above has demonstrated the ability of a retreating trench to induce deformation within the overriding plate. Here the diversity of localised extension that trench retreat can bring about within the overriding plate is presented. Three grades

of stretching state within the overriding plate have been recognised. Grade i) Minor extension. In the mantle wedge, convective mantle flux erodes part of the overriding plate's bottom (Figure 3.4, a). Further away towards the overriding plate, observable but very limited thinning of the thermal lithosphere develops. Grade ii) Rifting. A higher magnitude of thermal erosion develops in the mantle wedge. While rifting extension forms during non-steady state subduction in the back-arc (Figure 3.4, b), forming a ridge-like geometry at the plate's thermal bottom. The rift goes inactive during the steady state subduction. Grade iii) Spreading seafloor or break-up extension. In the mantle wedge, even higher magnitude of thermal erosion develops but no rifting extension forms. Further away towards the overriding plate, rifting extension develops and then breaks up into two parts forming a new oceanic floor during non-steady state subduction (Figure 3.4, c). The width of the opening seafloor can be as wide as ~250 km. During the steady state subduction, the break-up goes inactive due to the lack of consistent strong trench retreat.
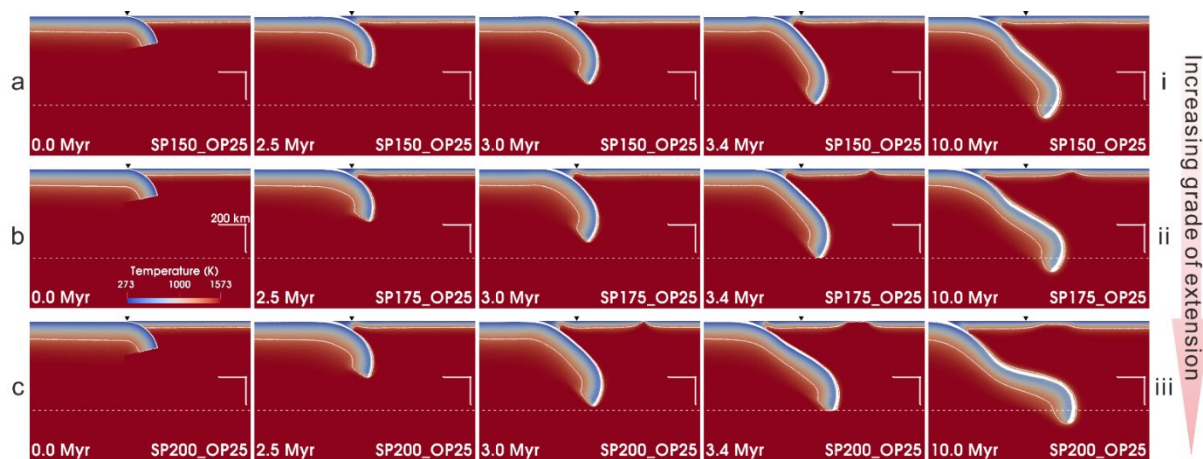
Figure 3.4 Simultaneous snapshots of the thermal field evolution of three cases, illustrating the differing stretching states within the overriding plate: a) minor extension (model SP150_OP25); b) rifting (model SP175_OP25); c) spreading seafloor (model SP200_OP25). All screenshots share the same temperature scale as is shown in first screenshot in row b.

To understand the deformation in the three stretching states, the second invariant of strain rate ($\dot{\varepsilon}_{II}$) is tracked in the back-arc region and plotted over time (Figure 3.5). It shows that for the five models that develop minor extension stretching state (Table 3.1), $\dot{\varepsilon}_{II}$ is always less than $2 \times 10^{-14}\ s^{-1}$ throughout the simulation. While for the two rifting extension models, $\dot{\varepsilon}_{II}$ can go beyond $2 \times 10^{-14}\ s^{-1}$ and reach the maximum value of ~$3.3 \times 10^{-13}\ s^{-1}$ when rift develops within the overriding plate. For the three break-up models, $\dot{\varepsilon}_{II}$ exceeds $3.3 \times 10^{-13}\ s^{-1}$ when the rifting ridge starts to spread in the back-arc. The strain rate quickly drops down to less than $1 \times 10^{-13}\ s^{-1}$ during steady state subduction, indicating that extensional deformation within the overriding plate gradually stops simultaneously.
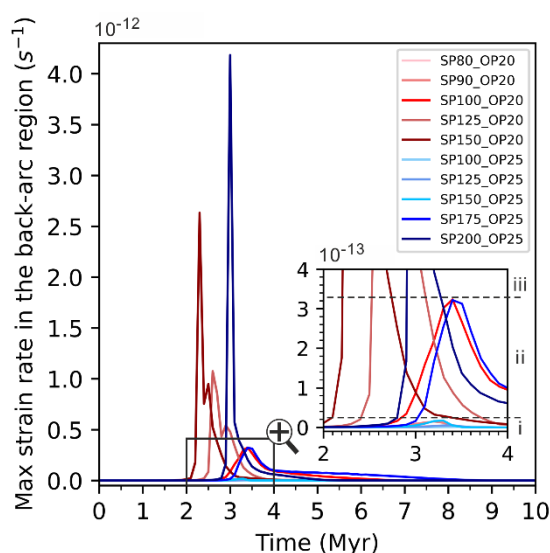
Figure 3.5 Maximum second invariant of strain rate through time in the back-arc region. The period from 2 to 4 Myr is enlarged to display the maximum strain rate corresponding to minor extension (Grade i) and to rift extension (Grade ii) that can be achieved throughout the simulation.

Matching the three stretching states with the trench retreat rate over time (Figure 3.2, a), it takes a minimum magnitude of trench retreat rate (u_{rift}) to initiate rifting within a given overriding plate. The u_{rift} for $Age_{OP}^0 = 20\ Myr$ and $Age_{OP}^0 = 25\ Myr$ are ~19 cm/yr and ~27 cm/yr respectively. When the trench retreat rate exceeds u_{rift}, break-

up extension develops following the rifting in the back-arc region. Take model SP200_OP25 for example, when the trench retreat rate reaches ~27 cm/yr at 2.9 Myr, the overriding plate starts to rift and $\dot{\varepsilon}_{II}$ is $1.8 \times 10^{-13} \, s^{-1}$ falling in the range of rift deformation (Figure 3.5). Then the trench retreat rate exceeds u_{rift} and break-up extension develops characterised by high $\dot{\varepsilon}_{II}$ greater than $3.3 \times 10^{-13} \, s^{-1}$ (Figure 3.5).

3.3.4 Regime diagram

Combining the above diagnostics and visualised output, a regime diagram of overriding plate stretching state is plotted in response to a variety of subducting and overriding plate ages (Figure 3.6, a). The diagram is divided into three parts based on the final stretching state of the overriding plate: i) minor extension, ii) rifting, iii) seafloor spreading. The diagram shows that with either increasing Age_{SP}^0 (i.e., increasing $\left| u_{max}^{0-t_{660}} \right|$) or decreasing Age_{OP}^0 (i.e., decreasing u_{rift}), a stronger extent of extension develops within the back-arc region.
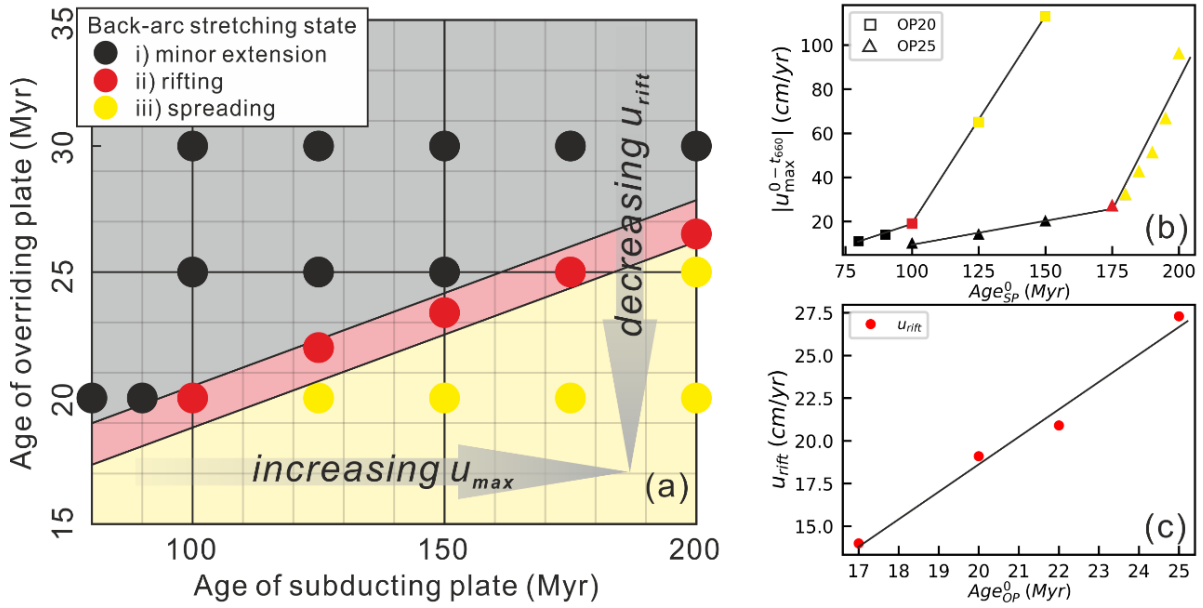
Figure 3.6 Regime diagram of back-arc extension and age dependency of trench motions. (a) Regime diagram of back-arc stretching state with varying Age_{SP}^0 and Age_{OP}^0. Grey area with black dot models has minor extension in the back-arc region, while pink area with red dot models is rifting extension. The yellow area with gold dot models represents spreading back-arc. (b) The maximum trench retreat rate in response to Age_{SP}^0. (c) The minimum trench retreat rate to initiate rift extension within an overriding plate with an initial age of Age_{OP}^0. The colour of markers in (b) and (c) refer to the legend of back-arc stretching state in (a).

In summary, it takes a minimum magnitude of trench retreat rate u_{rift} to initiate rifting within a given overriding plate in these models. The $\left|u_{max}^{0-t_{660}}\right|$ depends on Age_{SP}^0 for a given overriding plate (Figure 3.6, b), while the magnitude of u_{rift} depends on the strength of the overriding plate, i.e. Age_{OP}^0 in this research (Figure 3.6, c). A steeper slope of $\left|u_{max}^{0-t_{660}}\right|$ against Age_{SP}^0 is observed in models with spreading extension (Figure 3.6, b). This suggests that the strength of the original overriding plate is greatly weakened during rift extension, and it becomes equivalent to a much younger overriding plate in terms of rheology.

Comparing $\left|u_{max}^{0-t_{660}}\right|$ and u_{rift}, it is found that the results match well with the stretching state observed. i) If $u_{\mathrm{max}} < u_{\mathrm{rift}}$ then the overriding plate lithosphere has little extension and max $\dot{\varepsilon}_{II}$ is $3 \times 10^{-14}\,s^{-1}$. ii) If $u_{\mathrm{max}} \approx u_{\mathrm{rift}}$ the overriding plate rifts but would neither be torn apart nor spread, when $\dot{\varepsilon}_{II}$ ranges from $3 \times 10^{-14}\,s^{-1}$ to $3 \times 10^{-13}\,s^{-1}$. iii) If $u_{\mathrm{max}} > u_{\mathrm{rift}}$, the back-arc region rifts when the trench retreat rate reaches u_{rift}, then it breaks up into two parts and spreads after it exceeds u_{rift} with $\dot{\varepsilon}_{II}$ simultaneously exceeding $3 \times 10^{-13}\,s^{-1}$.

3.4 Discussion

3.4.1 Origin of the three stretching states in the overriding plate

The driving mechanism of how the trench retreats, and slab rollback induces extension within the overriding plate, remains debated. Trench suction and non-uniform basal traction are two basic driving mechanisms. The stress field results show that a compressional stress field next to the subduction interface on the overriding plate's side prevails during the non-steady state subduction (Figure 3.3, b). This indicates that shortening, rather than extension, is the dominant deformation there, which excludes a direct correlation between trench suction at the subduction interface with focused back-arc extension. Similar horizontal shortening deformation at the subduction interface as the trench retreats is also reported in other research (Chen et al., 2016; Schellart and Moresi, 2013). However, the velocity field does show that mantle flow underlying the overriding plate is sucked into the wedge as the slab rolls back (Figure 3.3, c). So 'deep slab suction' rather than 'trench suction' may contribute to the back-arc extension by facilitating the mobility of mantle flow in the mantle wedge.

To understand the origin of the three overriding plate stretching states developed in this research, it is essential to study the mantle circulation underlying the overriding

plate. During the non-steady state subduction, a strong anticlockwise poloidal flow develops underlying the overriding plate before the rift forms (Figure 3.3, c). Take models SP150_OP25, SP175_OP25 and SP200_OP25 for example, the flow could be decomposed into two components: focused upwelling from the transition zone; and trenchward horizontal flow underneath the overriding plate (Figure 3.7). These two differently directed flows correspond to the two end members of potential driving mechanisms accounting for the stretching state within the overriding plate: 1) upwelling thermal intrusion; and 2) lateral basal traction. As velocity difference is key to generate shear traction upon the overriding plate, the high velocity component areas ($\geq u_{rift}$) is filtered and their correlation with the development of three stretching states within the overriding plate is analysed.
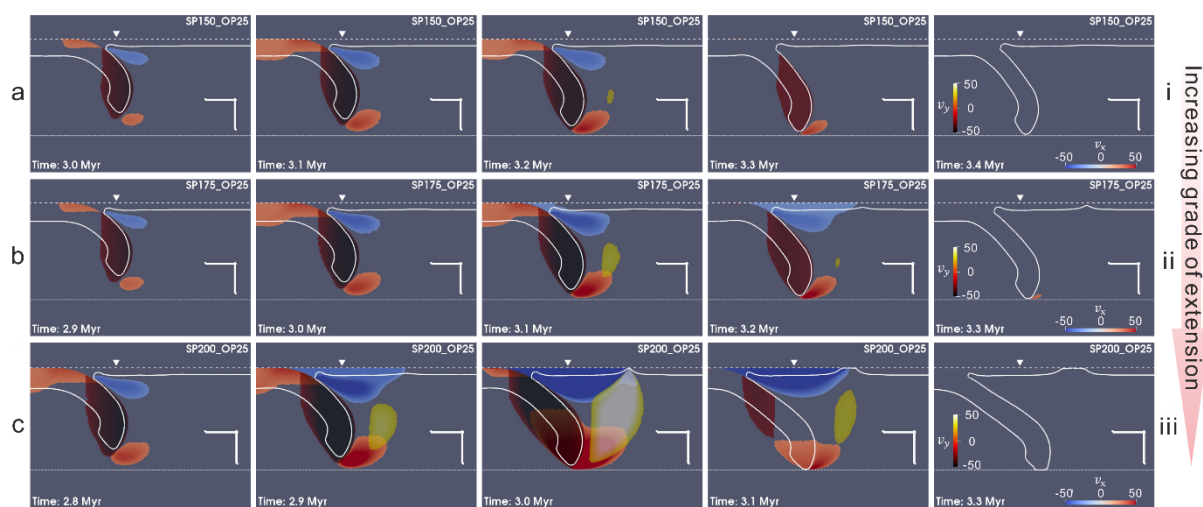
Figure 3.7 Snapshots of vertical and horizontal components of mantle circulation induced by slab roll-back. The vertical flow (u_y) and horizontal flow (u_x) are highlighted with two separate color legends (right most snapshot). Trenchward and downwelling motions are negative in the screenshots. Besides, all the visualised areas have a velocity magnitude higher than u_{rift} (~27 cm/yr for $Age_{OP}^0 = 25\ Myr$) in the corresponding direction, i.e. either $|u_y| \geq u_{rift}$, or $|u_x| \geq u_{rift}$. The models i, ii, iii corresponds to the three stretching states described in Figure 3.4. The loose dashed line marks the surface while the dense dashed line is at 660 km depth (the base of the transition zone).

3.4.1.1   Lateral basal traction

The fast horizontal flow prevails over the upwelling component among all snapshots in Figure 3.7. Initially, the trenchward horizontal flow forms in the mantle wedge underlying the overriding plate and extends laterally to ~500 km from the wedge corner (Figure 3.7). The spatial distribution indicates the existence of both lateral and vertical velocity gradient, which produce non-uniform magnitude of basal drag beneath the overriding plate. The wedge flow gradually drags the overlying overriding plate trenchward. This can be seen as the high velocity magnitude region extends up from the wedge to include the overriding plate (3.1 to 3.2 Myr in Figure 3.7, b and 2.8 to 3.1 Myr in Figure 3.7, c). Due to the non-uniform basal drag effect, the trenchward velocity difference within the overriding plate grows. This leads to a growing magnitude of accumulated extension which would end up with increasing stretching states within the overriding plate.

The magnitude of the horizontal flow can exceed 50 cm/yr for a short period (<1 Myr) in these models. Mineral texturing development analysis near the slab edges of Tonga and seismic anisotropy observations beneath Alaska subduction zones suggest comparable magnitude of rapid wedge flow, up to 50-90 cm/yr(Conder and Wiens, 2007; Jadamec and Billen, 2010). It is thus proposed here that the non-uniform basal drag of the rapid wedge flow driven by rapid trench retreat plays a vital role in producing back-arc opening during subduction.

3.4.1.2   Upwelling thermal intrusion

Figure 3.7 shows that fast-upwelling mantle flow is observed in all three models though it lasts for no more than 0.3 Myr. The size of the fast-upwelling mantle body grows with Age_{SP}^0, indicating a stronger return flow. In model SP200_OP25, the upwelling even appears under the rift before it fades away as the non-steady state subduction ends

(Figure 3.7, c). However, the high velocity upwelling flow is prone to strengthen the stretching within the overriding plate rather than initiating significant rifting extension. This is stated because it is not observed to interact with the overriding plate for model SP175_OP25 which starts to rift at 3.2 Myr (Figure 3.7, b).

In summary, the basal traction induced by trench retreat, or slab rollback, is the main driving force to account for different magnitude of extension within the overriding plate in the models. While the upwelling mantle component may reinforce the extension.

3.4.2   Comparing with other back-arc extension models

Previous research indicates that fixing the trailing boundary condition of the overriding plate can increase the degree of focused back-arc extension in contrast to models with a free mobile overriding plate (Capitanio et al., 2010; Chen et al., 2016; Hertgen et al., 2020; Nakakuki and Mura, 2013; Schellart and Moresi, 2013). While introducing heterogeneity, e.g. weak zone, in the overriding plate (Currie et al., 2008; Nakakuki and Mura, 2013; Yang et al., 2019) or lowering the strength of the whole overriding plate (Capitanio et al., 2010) can cultivate thinning lithosphere or even spreading back-arc extension (Figure 3.8). In brief, it usually takes a fixed or a weakened overriding plate to produce back-arc extension incorporating a rift. By contrast, this research demonstrates the capability of producing an opening back-arc in a homogeneous (i.e., without an arbitrary weak zone) mobile overriding plate by increasing the magnitude of non-uniform basal drag underlying the overriding plate as the trench retreats rapidly.
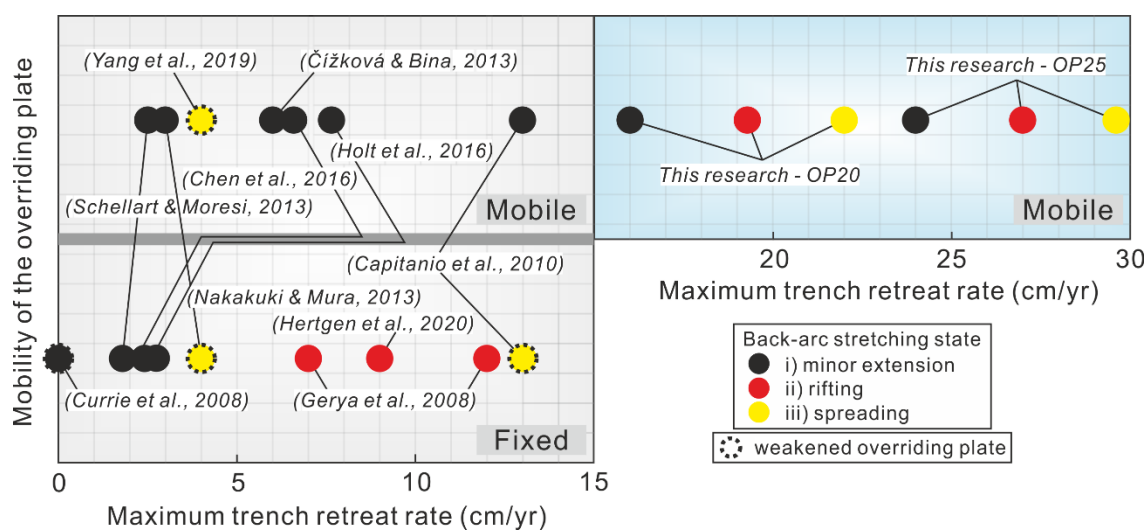
Figure 3.8 Summary of maximum trench retreat rate, mobility of the overriding plate and back-arc stretching state in previous research.

Previous models also indicate that maximum trench retreat is often reached at the end of non-steady state subduction when the slab starts to interact with the lower mantle (Capitanio et al., 2010; Schellart and Moresi, 2013). The maximum trench retreat rate achieved during previous research presented in Figure 3.8 is ~13 cm/yr, which is lower than that of ~16 cm/yr observed in Tonga (Bevis et al., 1995). Considering that more than 90% of slabs have reached the lower mantle (van der Meer et al., 2018), the non-steady state subduction is transient relative to the following steady state subduction and its evolving history is poorly constrained by observations. It is considered that the trench retreat rate can reach a high magnitude, at least for a short period (<1 Myr), during the non-steady state subduction phase, as produced in the models here. This allows us to suggest the existence of a minimum trench retreat rate to initiate back-arc opening for a given overriding plate. The results imply that the role of non-steady state subduction and transient rapid trench retreat in promoting deformation within the overriding plate may be underestimated.

3.4.3 Comparing with subduction zones on Earth

The results indicates that when the age of the subducting slab is old enough, it will allow the trench to retreat fast enough to initiate rift extension or even break-up extension in the back-arc region through non-uniform basal traction. This may explain why the subducting plate is always old, ranging from 55 Ma to 160 Ma, in subduction zones with a back-arc basin (Sdrolias and Müller, 2006).

A wide range of trench retreat rate is obtained by tuning Age_{SP}^0. However, modern observation shows that there is poor correlation between Age_{SP}^0 and trench retreat rate (Heuret and Lallemand, 2005). The result indicates that trench retreat rate loses its age dependency when the subducting slab starts to interact with the lower mantle. Considering that most subducting slabs on Earth have already reached or are approaching the lower mantle (van der Meer et al., 2018), it is then not surprising that a poor correlation is observed. The result suggests that different stages of subduction play an important role in controlling subduction kinematics and it may help us better understand observations on Earth.

This chapter replicates three back-arc stretching states with a wide range of trench retreat rate. The extent of back-arc extension exhibits positive correlation with trench retreat rate. This matches well with subduction zones where trench retreat rates are higher than 5 cm/yr on Earth (Heuret and Lallemand, 2005; Schellart et al., 2008). Take the Lau-Havre-Taupo back-arc system for example, the width of the back-arc region narrows southward from ~500 km in Lau Basin to ~100 km along the Havre Trough and terminates in Taupo Volcanic Zone (Parson and Wright, 1996). The trench retreat rate correspondingly slows down from ~16 cm/yr to ~0 cm/yr along the Tonga-Kermadec trench (Schellart et al., 2008). While the thickness of the crust increases

from ~5 km to ~25 km southward (Parson and Wright, 1996) and a high spreading rate is observed in northern Lau Basin at ~9.1 – 15.9 cm/yr (Bevis et al., 1995).

In the models that produce spreading back-arc, it is found that the opening seafloor stops spreading after trench retreat rate drops to a low constant magnitude of ~3 cm/yr during steady state subduction (Figure 3.4, c). This may explain why some spreading back-arc stop spreading even when subduction continues. For example, the back-arc in Japan sea opened at ~21 Ma and ceased spreading since ~14 Ma during the Pacific Plate subduction (Tatsumi et al., 1990). The Japan subduction zone is still active while the present trench retreat rate is low at only ~0 cm/yr (Schellart et al., 2008).

It is noted that the simplified models cannot reproduce the periodic opening process of the back-arc basin. Magnetic anomalies in opening back-arc regions indicate that the spreading tends to be periodic and consistent (Caratori Tontini et al., 2019; Eagles and Jokat, 2014) rather than abrupt and short-lived. During steady state subduction, the rifted back-arc region is likely to spread if high trench retreat rate is maintained rather than drops to the value of ~3 cm/yr seen in the models here. This may be attributed to the limitation imposed by the 2D models and the single suite of rheology laws excluding the melting process, which is discussed next.

3.4.4   Limitations

3.4.4.1   2D and 3D models

Trench retreat could generate convective mantle flow that includes poloidal and toroidal components. Two dimensional models, by their nature, can only produce poloidal flow. It is noted though, that poloidal flow is expected to dominate during the non-steady state subduction (Funiciello et al., 2004). That is when high trench retreat

rate develops in the models. Thus, a lack of toroidal flow might only have a limited impact on the formation of rapid trench retreat rate during non-steady state subduction.

However, as the subducting slab starts to interact with the lower mantle, trench retreat and upper mantle flow in 2D models are greatly inhibited (Figure 3.2, a, Figure 3.3, c). Trench retreat rate slows down by ~60% (Holt et al., 2015) and >70% in the models here. This occurs because the subducting slab, combining with the viscosity jump into the lower mantle, disconnects the upper mantle flow on either side of the slab. While in 3D models, toroidal flow could efficiently transport mantle flow from the subducting plate side towards the overriding plate side - around the edges of slabs. Slab interaction with the lower mantle only slows down the trench retreat by 0% to ~33% in 3D models (Chen et al., 2016; Schellart et al., 2011). In this case where the slab is interacting with the lower mantle, the lack of toroidal flow causes a significant slowing down effect on the trench retreat rate and potentially also simultaneously inhibits back-arc extension. Thus, the lack of toroidal flow may not be neglected when slab starts to interact with the lower mantle.

3.4.4.2   Absolute value of trench retreat rate and u_{rift}

This research aims to provide a guiding reference framework to correlate trench retreat rate and extent of extension in the back-arc region rather than provide precise predictions. Thus, the absolute value of trench retreat rate should be treated with caution. It is noted that while the older subducting plate ages (> 160 Ma) at trenches are presently not common on Earth (Müller et al., 2008), they provide us a way to self-consistently produce the varying trench retreat rates. Considering that there is a lot of uncertainty in terms of the strength of plates on Earth, the trench retreat rate it takes to initiate rift extension could vary greatly. Some of the models here yield much higher

trench retreat rates than observed, this may imply that either the rheology used here does not fully agree with real Earth or that current observation might be incomplete.

During non-steady state subduction, $\left|\overline{u_{trench}^{0-t_{660}}}\right|$ in the model (3.5-15.6 cm/yr) is in the same range as actual observations on Earth (0-16 cm/yr). While the maximum trench retreat rate obtained from the model (10-113 cm/yr) spans a much wider range than observations on Earth. The extremely high $\left|u_{max}^{0-t_{660}}\right|$ is achieved in spreading back-arc models after the back-arc lithosphere's rheology is reshaped by the emplaced rifting ridge. Similar abrupt acceleration is reported to exist in some rifting continental margins and it is controlled by the nonlinear decay of the strength force resisting rifting (Brune et al., 2016). It should be noted that the extremely high value of transient trench retreat rate might not match any real-world observations, which are often averaged rather than instantaneous values. The ever-increasing trench retreat rate correlates to a feedback weakening process as strain localises, which is quite common in numerical modelling.

The u_{rift} for $Age_{OP}^0 = 20\,Myr$ and $Age_{OP}^0 = 25\,Myr$ are ~19 cm/yr and ~27 cm/yr separately, hinting that it can be difficult to initiate rifting extension in models $Age_{OP}^0 > 20\,Myr$ with observed trench retreat rates on Earth.

There are several parameters that could potentially lower the u_{rift} which is not addressed in this research, for example, inhibiting the mobility of the overriding plate , incorporating melt weakening rheology or lowering the strength of the overriding plate.

3.5   Conclusion

The 2D thermo-mechanical self-consistent models demonstrate the capability of initiating back-arc rifting or spreading in a mobile and homogenous (no arbitrary weak zone) overriding plate with high enough trench retreat rate during subduction. A wide range of trench retreat rate is achieved by varying the initial age of the subducting plate at the trench for a given overriding plate. The models evolve from a non-steady state towards a steady state with the transition occurring when the subducting plate approaches the lower mantle. During non-steady state subduction, trench retreat rate accelerates and reaches its maximum value, which depends on the initial age of the subducting plate. In all, three types of stretching state were observed within the overriding plate: i) minor extension, where the overriding plate lithosphere remained generally unchanged; ii) rift extension, where the overriding plate would be rifted but not torn apart; iii) spreading extension, where back-arc is rifted and then breaks apart into two spreading parts. The results indicate that it takes a minimum trench retreat rate to initiate rift extension and a higher trench retreat rate to open the back-arc. The driving force in these models is suggested to be the non-uniform basal drag resulting from the mantle wedge flow driven by the rapid trench retreat. After the subducting plate reaches the lower mantle, the trench retreat rate drops to a constant magnitude around 3 cm/yr and loses the dependency on the initial age of subducting plate. Meanwhile, simultaneously the back-arc extension stops when trench retreat rate slows down during the steady state subduction. This suggests that different stages of subduction may play an important role in controlling subduction kinematics and it may help us better understand why there is poor correlation between trench retreat rate and the age of subducting plate.

In addition to the previous understanding of back-arc extension, it is proposed here that high enough trench retreat rate can initiate a rift or spreading back-arc extension through non-uniform basal drag even when the overriding plate is mobile.

Chapter 4 Progressive weakening within the overriding plate during dual inward dipping subduction

4.1 Introduction

Subduction can pose a fundamental tectonic overprint on the overriding plate by generating a volcanic arc (Perfit et al., 1980; Straub et al., 2020), back-arc basin (Uyeda, 1981), orogeny (Faccenna et al., 2021), or even continental breakup (Dal Zilio et al., 2018). Most subduction zones involve only one subducting slab. This research considers multiple subducting slabs, in particular dual inward dipping subduction. Dual inward dipping subduction, or bi-vergent subduction occurs when the overriding plate is decoupled with two subducting slabs dipping towards each other. It is one of the four most commonly described subduction zones with multiple slabs, i.e., inward-dipping, same-dip, outward-dipping and oppositely dipping adjacent subduction zones (Holt et al., 2017; Király et al., 2021).

Dual inward dipping subduction zones are often found in areas which exhibit complex geodynamic processes in their geological history. Seismic tomography shows that dual inward dipping subduction exists at the Caribbean plate between the Cocos slab and Lesser-Antilles subduction zone (Van Benthem et al., 2013), the Philippine islands between the Philippine trench and Manila trench (Wang and He, 2020), South-East Asia between the Philippine and the Sumatra subduction, and the region between

Tonga and New Hebrides subduction zones (Hall and Spakman, 2015; Huang et al., 2015; Maruyama et al., 2007; van der Meer et al., 2018). In combination with seismic tomography, recent plate reconstructions have made it more evident that dual inward dipping subduction could have existed in some regions in the past (Faccenna et al., 2010; Hall and Spakman, 2015) constrained by suture zone petrology demonstrating oceanic floor closure. A good example is the North China Craton (Figure 4.1). Suture zone studies reveal that multiple inward dipping subduction may have surrounded the North China Craton from Early Paleozoic to Tertiary (Santosh, 2010; Windley et al., 2010).

The global strain rate map shows that a high strain rate belt is often observed in the back-arc region of the single-sided subduction zone (Kreemer et al., 2014), while the distribution of high strain rate areas gets complex in dual inward dipping subduction zones. In detail, when the trenches between two subduction zones are far away from each other, the high strain rate belt is prone to stay with its nearest trench. While when the trenches are close to each other, a greater area of high strain rate region is observed. The difference implies that dual inward dipping subduction may be more efficient in generating a high strain rate area within the overriding plate.

Despite these observations, dual inward dipping subduction is still poorly understood in terms of how it differs from single sided subduction in deforming or weakening the overriding plate.

a) **Early Paleozoic**
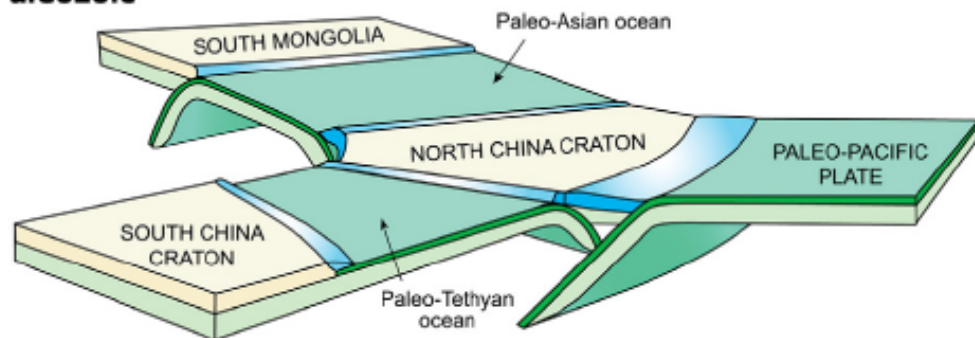
b) **Late Paleozoic to Early Triassic**
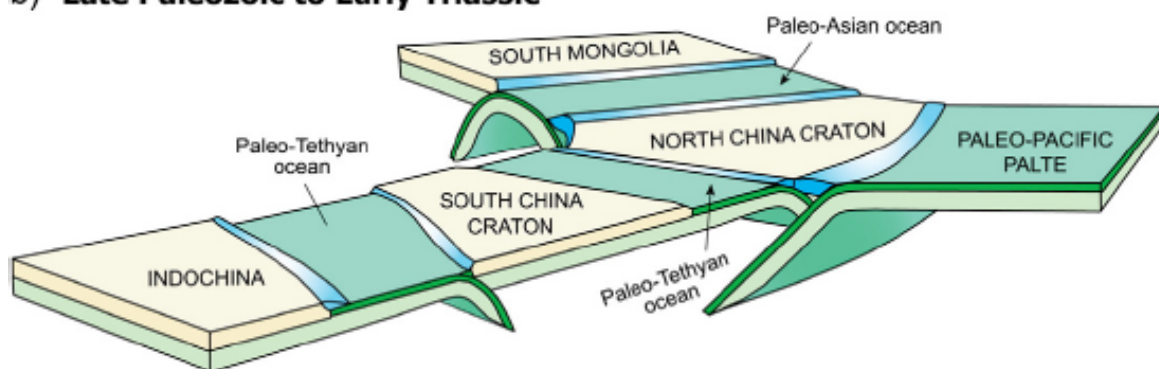
c) **Early Cretaceous to Tertiary**
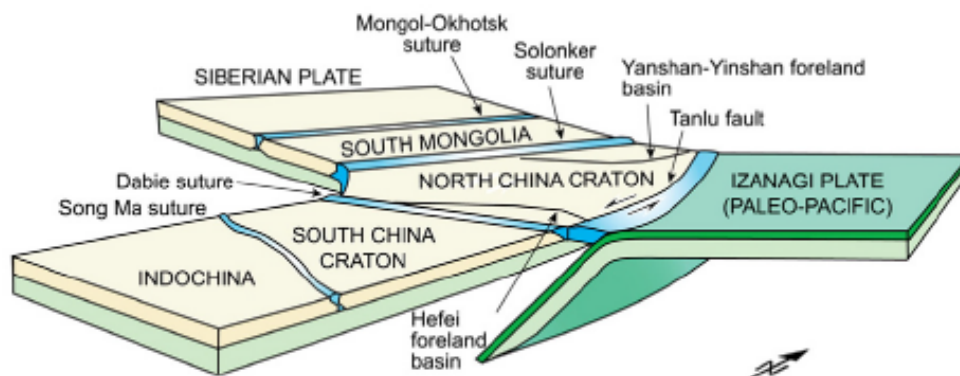
Figure 4.1 Multiple inward-dipping subduction surrounding the North China Craton from the Early Paleozoic to Tertiary revealed by suture zone studies (Adapted from Windley et al., 2010).

Numerical investigations have been conducted to understand the dynamics of dual inward dipping subduction. Research shows that the initial slab dip of the subducting plate affects the upper mantle dynamic pressure between the convergent slabs and stress state within the overriding plate (Holt et al., 2017). Varying the distance between

the trenches, convergence rate, and asymmetry of subducting plates can alter the topography of the overriding plate (Dasgupta and Mandal, 2018). The thickness of the plates and the lithosphere to asthenosphere viscosity ratio are all tested to investigate their effect on the slab geometry and the magnitude of mantle upwelling flow underlying the overriding plate (Lyu et al., 2019).

These pioneering investigations show that dual inward dipping subduction can generate a variety of upper mantle flow patterns which regulate the stress state and topography of the overriding plate. However, previous models all applied a simplified constant or linear viscous rheology for both plates and convective mantle flow, i.e., the viscosity is neither temperature nor stress-dependent. Mineral deformation experiments indicate that viscosity varies as a function of multiple parameters, e.g., temperature, pressure, stress, strain rate etc. (Bürgmann and Dresen, 2008; Burov, 2011; Hirth and Kohlstedt, 2003; Karato, 2010; Lynch and Morgan, 1987). Thus, previous dual inward dipping subduction models with simplified rheology were unable to fully reflect the weakening process, e.g., high strain rate in the back-arc region, due to slab rollback and/or induced mantle wedge flow.

Single sided subduction models incorporating composite rheology, e.g., dislocation creep, diffusion creep, yielding etc., has improved our understanding of subduction's impact upon the overriding plate (e.g., Alsaif et al., 2020; Čížková and Bina, 2013; Garel et al., 2014; Schliffke et al., 2022; Suchoy et al., 2021). It has not been investigated before, to the best of our knowledge, in terms of which rheology law dominates the weakening process observed in the overriding plate or how different deformation mechanisms interplay with each other during subduction.

In this research, a series of 2-D thermo-mechanical models incorporating composite rheology laws are run to investigate how dual inward dipping subduction differs from

single sided subduction in deforming the overriding plate. We also identify the dominant deformation mechanism that induces progressive weakening and investigate the interplay among different deformation mechanisms applied.

4.2 Methods

4.2.1 Model setup

Similar with the single sided subduction models in Chapter 3, the computational domain is 10,000 km by 2,900 km, with x (width) coordinates and z (depth) coordinates extending from the surface to the bottom of the lower mantle (Figure 4.2). Such a wide domain reduces the influence of side and bottom boundary conditions (Chertova et al., 2012). The thermal boundary conditions at the surface and bottom are defined by two isothermal values: $T = T_s$ and $T = T_m$ for surface and base of lower mantle respectively, while the sidewalls are insulating. As for mechanical boundary conditions, a free-surface is applied at the top boundary to facilitate trench mobility, while the other boundaries are free-slip.
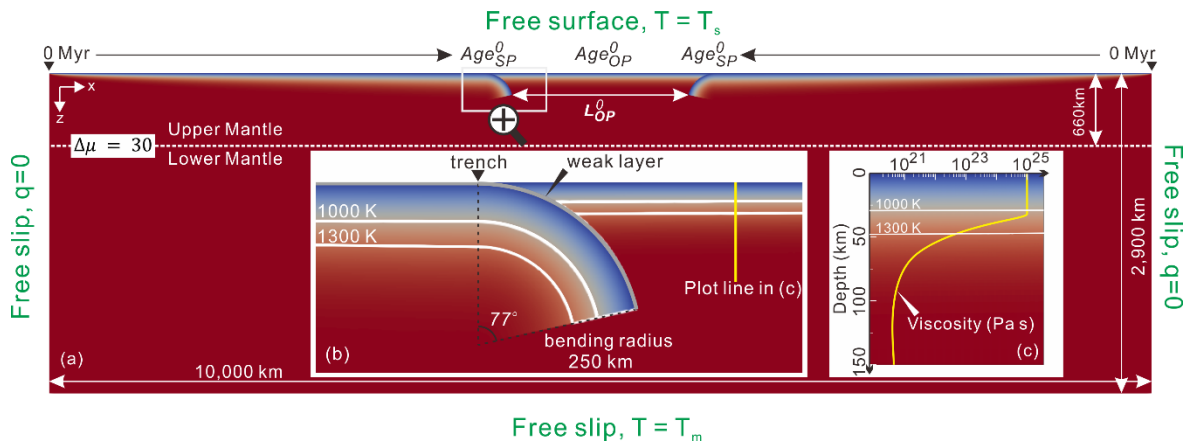
Figure 4.2 Dual inward dipping model geometry and initial setup illustrated with the initial temperature field as the background. (a) The whole computational domain. Age_{SP}^0 and Age_{OP}^0 represent the initial ages of subducting plate and overriding plate at trench. The viscosity jump ($\Delta\mu$) between upper and lower mantle at 660 km transition zone is set up with a fixed value of 30. To be noted, L_{OP}^0 represents the distance between the leading tip edges of the slabs initially penetrating into the upper mantle. L_{OP}^0 roughly equals the length of the overriding plate with constant thickness, excluding the overriding plate above the interface with the bending slab. (b) Enlarged area of the trench zone where the bending slab meets the flat overriding plate. The 1100 K and 1300 K isotherms are marked in white contours. (c) Vertical profile of viscosity against depth within the overriding plate. The plot line is 400 km away from the initial trench.

To simplify the complexity of the model, a laterally symmetric dual inward dipping subduction is applied, i.e., the model is strictly symmetric along the vertical middle line of the domain (5000 km away from the side boundaries) in all aspects, e.g., the geometry and rheology properties. Age_{SP}^0 and Age_{OP}^0 represent the initial ages of subducting plate and overriding plate at the trench, where the two plates meet at the surface. Laterally on the surface, the age of the subducting plates increases linearly with their distance away from the mid-ocean ridge on either side. While vertically, the age of the plate at surface defines the initial thermal structure through a half-space cooling model (Turcotte and Schubert, 2014),

$$T(x,z) = T_s + (T_m - T_s)erf\left(\frac{z}{2\sqrt{\kappa Age^0(x)}}\right), \tag{4.1}$$

with x the distance away from the mid-ocean ridge, *erf* the error function, z the depth, κ the thermal diffusivity. All parameters are listed in Table 2.1. The whole overriding plate is set up with a constant age. Thus, the thermal structure within the overriding plate is laterally homogeneous. The bottom of thermal lithosphere is defined as the isotherm of 1300 K, where the temperature gradient starts to drop quickly (Garel and Thoraval, 2021). The initial thickness of the subducting plate (H_{SP}^0) and overriding plate (H_{OP}^0) can be calculated using

$$H_{Plate}^0 = erfinv((T_{1300K} - T_s)/(T_m - T_s)) * 2 * \sqrt{\kappa * Age_{Plate}^0(x)}, \qquad (4.2)$$

where H_{Plate}^0 is the initial thickness of plate thermal lithosphere and *erfinv* is the inverse error function.

The free surface boundary condition together with the mid-ocean ridge setup allows the subducting slabs, the overriding plate and therefore the trench to move freely as subduction evolves. To initiate self-driven subduction without implementing external forces, the subducting plate is set up with a bend into the mantle and an 8 km thick low-viscosity decoupling layer on the top. This weak layer has the same rheology as the rest of the domain, other than its maximum viscosity is 10^{20} Pa s, and its friction coefficient is 0.02 (i.e., an order of magnitude lower). The initial bending radius is 250 km and the slab bends over 77 degrees from the trench (Figure 4.2).

As indicated in the methods, the whole model domain shares the identical composite rheology law incorporating four deformation mechanisms. During each simulation, the viscosity governed by each deformation mechanism will be calculated and compared throughout the domain. The one that yields the least viscosity is the dominant deformation mechanism. It is worth repeating that the model combines the individual

viscosities in "parallel" to give the effective viscosity (see equation 2.7). The key rheology difference of the model setup with previous dual inward dipping subduction models (Dasgupta and Mandal, 2018; Holt et al., 2017; Lyu et al., 2019) is that the magnitude of viscosity throughout the model can self-consistently vary with time as the model evolves.

4.2.2   Model variables

Three variables are investigated here: the initial length of the overriding plate (L_{OP}^0), the initial thickness of the subducting plate (H_{SP}^0) and overriding plate (H_{OP}^0) (Table 4.1). These are parameters varied in previous research and therefore allow easier comparison. H_{SP}^0 and H_{OP}^0 are dependent on plate age and calculated using Equation (5.3). The magnitude of L_{OP}^0 that has been tested in previous models ranging from 500 km to 4000 km (Dasgupta and Mandal, 2018; Holt et al., 2017; Lyu et al., 2019), and the result shows that L_{OP}^0 greater than 2500 km has little impact on the result (Lyu et al., 2019). Here L_{OP}^0 is tested in the range from 500 km to 1600 km. The values of H_{SP}^0 and H_{OP}^0 that has been tested before ranges from 75-125 km and 75-150 km separately and those models suggest that H_{SP}^0 is more important in deciding the magnitude of upwelling mantle flow than H_{OP}^0 (Lyu et al., 2019). So the range of H_{SP}^0 is extended to 94-141 km while the range of H_{OP}^0 is narrowed down to 67-100 km.

Table 4.1 List of model setup.

Model name	L_{OP}^0 (km)	H_{SP}^0 (km)	Age_{SP}^0 (Ma)	H_{OP}^0 (km)	Age_{OP}^0 (Ma)
$H_{SP}^0 = 94\ km$	500	94	90	67	45
$H_{SP}^0 = 100\ km$	500	100	100	67	45
$H_{SP}^0 = 111\ km$	500	111	125	67	45
$H_{SP}^0 = 122\ km$	500	122	150	67	45
$H_{SP}^0 = 141\ km$	500	141	200	67	45
$H_{OP}^0 = 67\ km$	500	141	200	67	45
$H_{OP}^0 = 70\ km$	500	141	200	70	50
$H_{OP}^0 = 74\ km$	500	141	200	74	55
$H_{OP}^0 = 77\ km$	500	141	200	77	60
$H_{OP}^0 = 100\ km$	500	141	200	100	100
$L_{OP}^0 = 500\ km$	500	141	200	67	45
$L_{OP}^0 = 600\ km$	600	141	200	67	45
$L_{OP}^0 = 700\ km$	700	141	200	67	45
$L_{OP}^0 = 800\ km$	800	141	200	67	45
$L_{OP}^0 = 1000\ km$	1000	141	200	67	45
$L_{OP}^0 = 1200\ km$	1200	141	200	67	45
$L_{OP}^0 = 1600\ km$	1600	141	200	67	45

Models are named with the variable tested, e.g., $H_{SP}^0 = 94\ km$ and $H_{SP}^0 = 122\ km$ corresponds to the initial subducting plate thickness of 94 km and 122 km separately, while the initial overriding plate length and thickness in both models remain the same as 500 km and 67 km.

4.3 Results

4.3.1 Varying viscosity in an evolving model: an example

The thermal-mechanical model setup of this research enables self-consistent subduction. Similar to the self-consistent single subduction numerical and analogue models, subduction starts with a non-steady state phase where negative buoyancy pulls the slab to sink into the deeper mantle (Capitanio et al., 2010; Gerya et al., 2008; Schellart and Moresi, 2013). Following this short period of adjustment, the slab interacts with the lower mantle and steady state subduction ensues. Take model '$L_{OP}^0 = 1200\ km$' for example, the dynamic evolution process of dual inward dipping subduction is described in detail.

4.3.1.1   Non-steady state subduction

During the non-steady state subduction, symmetric subduction develops about the midline of the overriding plate (~5000km away from the side boundaries). As more slab is pulled into the mantle, the negative buoyancy grows gradually. It takes ~5.8 Myr before the slab starts to interact with the lower mantle (Figure 4.3).

Convective mantle wedge flow is generated as the subducting slab bends and sinks in the upper mantle. The size of the convective cell grows with time and forms a crescent shape as wide as ~500 km before the slab reaches the depth of lower mantle. The convective cell is composed of a narrow downwelling flow coupling close to the sinking slab and a wide upwelling flow further away. The upwelling flow fades gradually as its distance away from the subducting slab increases. In the model '$L_{OP}^0 = 1200 \, km$', the two sets of wedge flow have little interaction and can be considered as two separate units. This is because the length of the overriding plate is 1200 km, which is greater than two times the width (~500 km) of a convection cell.

The overriding plate exhibits a widespread extensional stress field as a result of continuous subduction and the induced convective mantle wedge flows. Only a limited area close to the interface with the bending slabs develops compression (Figure 4.3, a). The widespread extensional stress field implies that the overriding plate has an overall stretching tendency. Within the overriding plate, the governing deformation mechanism is spatially layered (Figure 4.3, b). At depths shallower than 30 km within the overriding plate, yielding (brittle or plastic) deformation dominates. Underlying the yielding layer lies ~10 km thick Peierls creep layer. While for depths from ~40 km to the bottom of the thermal lithosphere deformation is dominated by dislocation creep. High strain rate areas are observed within and underneath the overriding plate (Figure

4.3, c). The thermal thickness of the overriding plate, defined by the 1300 K isotherm

contour, does not change much throughout the simulation.
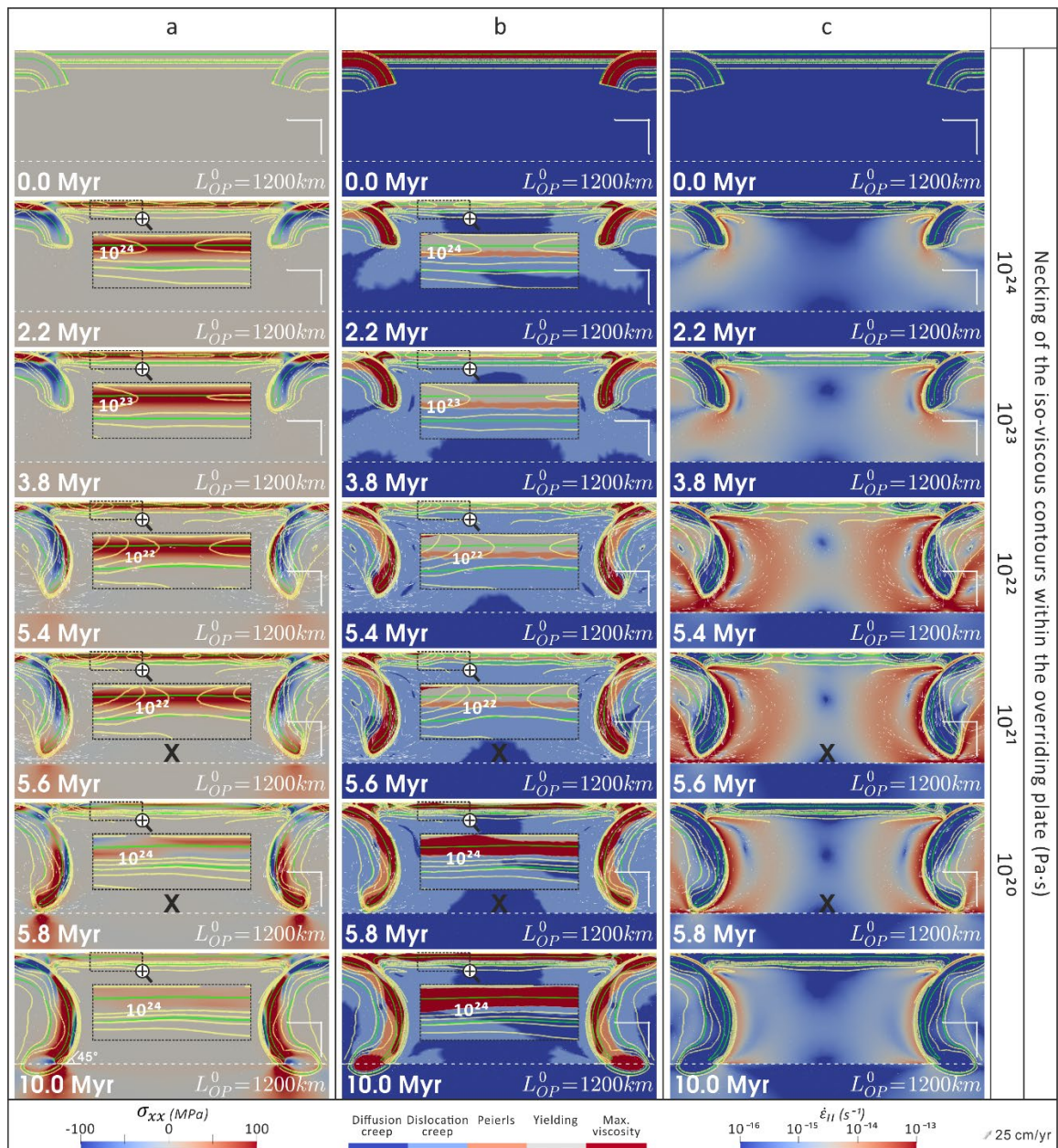
Figure 4.3 The Simulation screenshots of model '$L_{OP}^0 = 1200\ km$'. (a) Horizontal stress component where positive value represents stretching and negative value denotes compression. (b) The dominant deformation mechanism. (c) Magnitude of second invariant of strain rate. The progressive weakening process within the overriding plate is demonstrated by the necking of the iso-viscous contours. The 5 groups of yellow contours encompassing the plates in each screenshot are iso-viscous contours of $10^{20}, 10^{21}, 10^{22}, 10^{23}, 10^{24}\ Pa \cdot s$ from outward to inward. Screenshot with a bold 'X' underlying the overriding plate means there is no necking developing in that timestep for the iso-viscous contour whose value is noted on the right-hand side, e.g., $10^{21}\ Pa \cdot s$. The two sets of green solid lines are 700 K and 1300 K isotherm contours to image the geometry of the plate. The transition zone at the depth of 660 km is marked by the horizontal white dashed line. The white right-angle scale bar lying above the right end of the transition zone represents 200 km in both directions. The bottom left corner caption shows the elapsed simulation time and bottom right corner is the name of the model.

The non-Newtonian rheology laws applied define viscosity as a function of multiple variables, e.g., temperature, pressure, stress, strain rate etc. As subduction initiates, it creates rheology heterogeneities within what initially was a laterally homogeneous overriding plate, allowing part of it to become weaker than other parts. To visualize the variation in lithosphere viscosity, several levels of iso-viscous contours are plotted, e.g., $10^{24}, 10^{23}, 10^{22}, 10^{21} \, Pa \cdot s$ (Figure 4.3). Here, the overriding plate weakening level is defined as the maximum order of viscosity magnitude drop. That is, weakening level 'I', 'II', 'III', 'IV' represents that the iso-viscous contour $10^{24}, 10^{23}, 10^{22}, 10^{21} Pa \cdot s$ is necked within the overriding plate respectively. It shows that the homogeneous overriding plate is gradually segmented into three strong cores connected with two low viscosity necking regions. Strain is likely to localize upon these two necking areas and continuously lower the magnitude of viscosity therein. The minimum viscosity achieved in the overriding plate for model '$L_{OP}^0 = 1200 \, km$' is $10^{21} \sim 10^{22} \, Pa \cdot s$ (weakening level 'III'). The distance between these two necking regions is ~620 km (Figure 4.3, a, 3.8Myr). These necking regions match well with the high strain rate areas developed in the overriding plate. The initial result suggests that high strain rate may play an important role in softening the overriding plate during dual inward dipping subduction.

4.3.1.2 Steady state subduction

The steady state subduction process initiates after a short period of transition once slabs start to interact with the lower mantle. Due to the viscosity increase as the sinking slab enters the lower mantle at 660 km depth, it slows down, and the induced mantle wedge flow gets much weaker. After this, the model enters a steady state subduction process where mobility becomes slow and constant, and deformation reduces. Meanwhile, the necking of the iso-viscous contours is reversed by a cooling and healing process within the overriding plate (Figure 4.3). At the end of the 10 Myr

simulation, the dip between the top of bending slab and the transition zone is ~45° and the total trench retreat is ~100 km.

4.3.2 Length of the overriding plate

The first series of models investigate decreasing the initial length of the overriding plate (L_{OP}^0) from 1600 km to 500 km, while keeping the initial thickness of the subducting and overriding plate as 141 km and 67 km separately. As L_{OP}^0 decreases, the two symmetric subducting slabs become closer. The two separate convective mantle wedge flows start to combine with each other and form a stronger joint upwelling flow underneath the overriding plate (Figure 4.4). Consequently, as L_{OP}^0 is reduced, the two separate necking areas within the overriding plate get closer and merge into a single one in the end. Also as L_{OP}^0 is reduced it takes less time to lower each level of viscosity within the overriding plate during the non-steady state subduction. Besides, the progressive weakening process can go further and neck the $10^{21}\ Pa\ s$ iso-viscous contour (weakening level 'IV') when L_{OP}^0 reaches <= 800 km, initiating significant lithosphere thinning and even rifting or spreading extension within the overriding plate (Figure 4.4, b-c). The significant extension usually lasts less than 1 Myr before it gradually stops after the slab reaches the depth of the lower mantle, but it causes substantial changes to the dual inward dipping subduction system. For example, significant slab rollback starts to develop, creating a flattening slab geometry in the upper mantle and steepening dip angle (45° to 75°, Figure 4.4) at the transition zone depth by the end of the 10 Myr simulation.

It is noted that the continuous thinning of the thermal lithosphere only initiates when the iso-viscous contour of $10^{21}\ Pa\cdot s$ starts to neck. This implies a potential coupling of the thermal lithosphere and the rheology boundary layer (usually defined as the depth of $10^{21}\ Pa\cdot s$) in the model. All models necking $10^{21}\ Pa\cdot s$ will continue to neck

lower magnitudes of viscosity, e.g., $10^{20}, 10^{19}\ Pa \cdot s$. Simultaneously, the upwelling hot mantle flow can then ascend to fill the thinning region and create a new plate boundary (rifting extension) or even new sea floor (spreading extension) after it ascends to the surface. Thus, the ability to neck $10^{21}\ Pa \cdot s$ (or not) can be used as a key diagnostic to predict whether a new spreading ridge (new plate boundary) develops within the overriding plate (or just limited thinning).
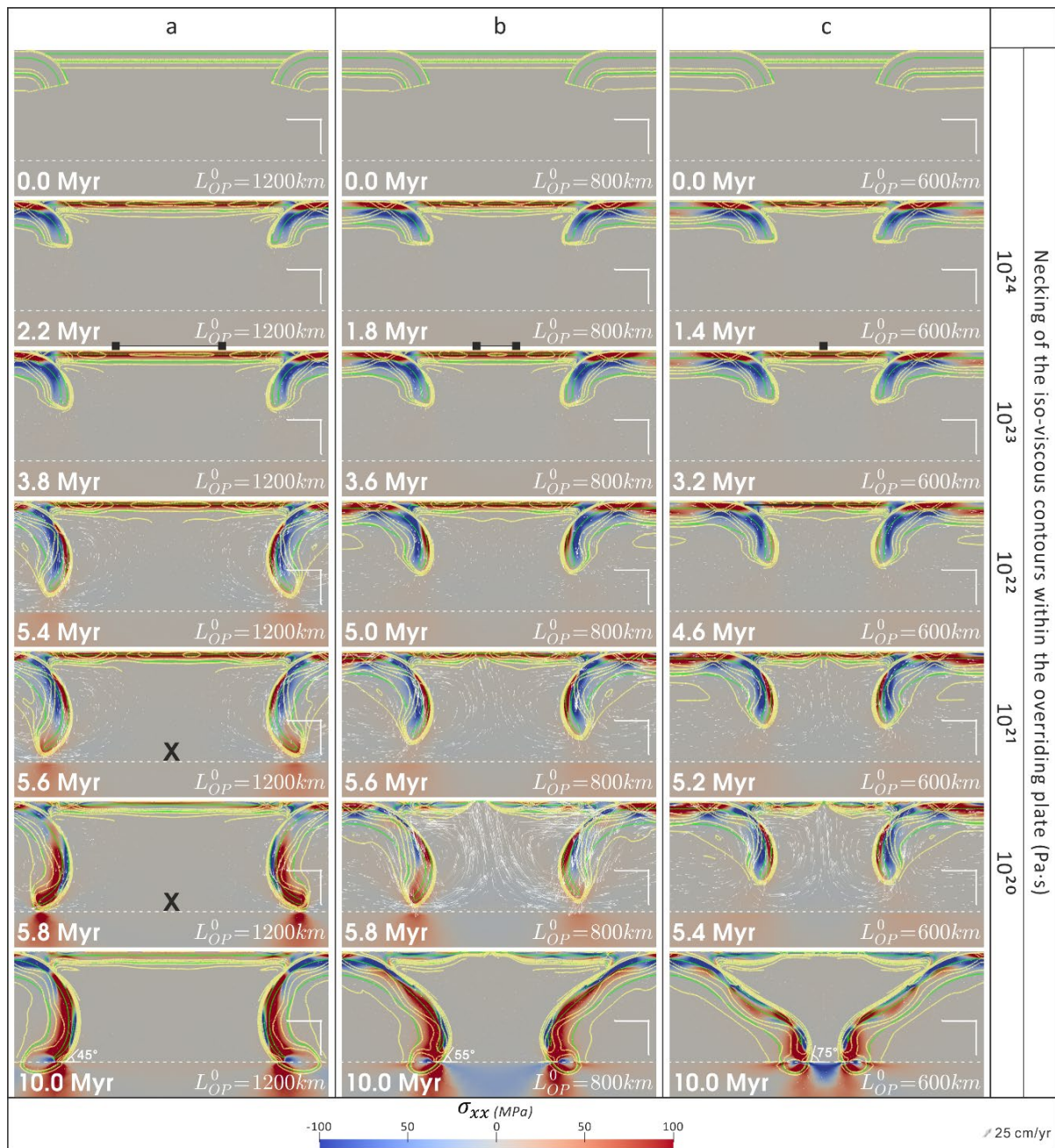
Figure 4.4 Progressive weakening of the overriding plate during dual inward dipping subduction with decreasing length of the overriding plate, (a) model '$L_{OP}^0 = 1200\,km$', (b) model '$L_{OP}^0 = 800\,km$', (c) model '$L_{OP}^0 = 600\,km$'. The location of necked regions in the overriding plate are marked with black squares. A detailed explanation of the contours and symbols could be found in the caption of Figure 4.3.

To take a closer look at the extension behaviour within the overriding plate, the evolving magnitude of viscosity at 5km depth is examined (Figure 4.5). The filled

region in the figure represents the overriding plate, therefore its widening represents extension within the overriding plate. As the initial length of the overriding plate (L_{OP}^0) decreases from 1600 km to 500 km, the total extension in the 10 Myr simulations increases from ~100 km (Figure 4.5, a-c) to 400~600 km (Figure 4.5, d-g). In detail, it is noted that extensional behaviour only become observable after the iso-viscous contour of $10^{23}\ Pa \cdot s$ is necked, i.e., after weakening level 'II' is achieved. Extension combining with lithospheric thinning only becomes significant when the iso-viscous contour $10^{21}\ Pa \cdot s$ is necked, i.e., when weakening level 'IV' is achieved. The highest weakening level achieved within the overriding plate increases from 'II' ($L_{OP}^0 = 1600\ km$) to 'III' ($L_{OP}^0 = 1000\ km$) and on to 'IV' ($L_{OP}^0 \le 800\ km$). During the spreading extension period, a highly centralised spreading centre (Figure 4.5, d, f-g), while multiple spreading centres are observed to accommodate the extension in model '$L_{OP}^0 = 700\ km$' (Figure 4.5, e).
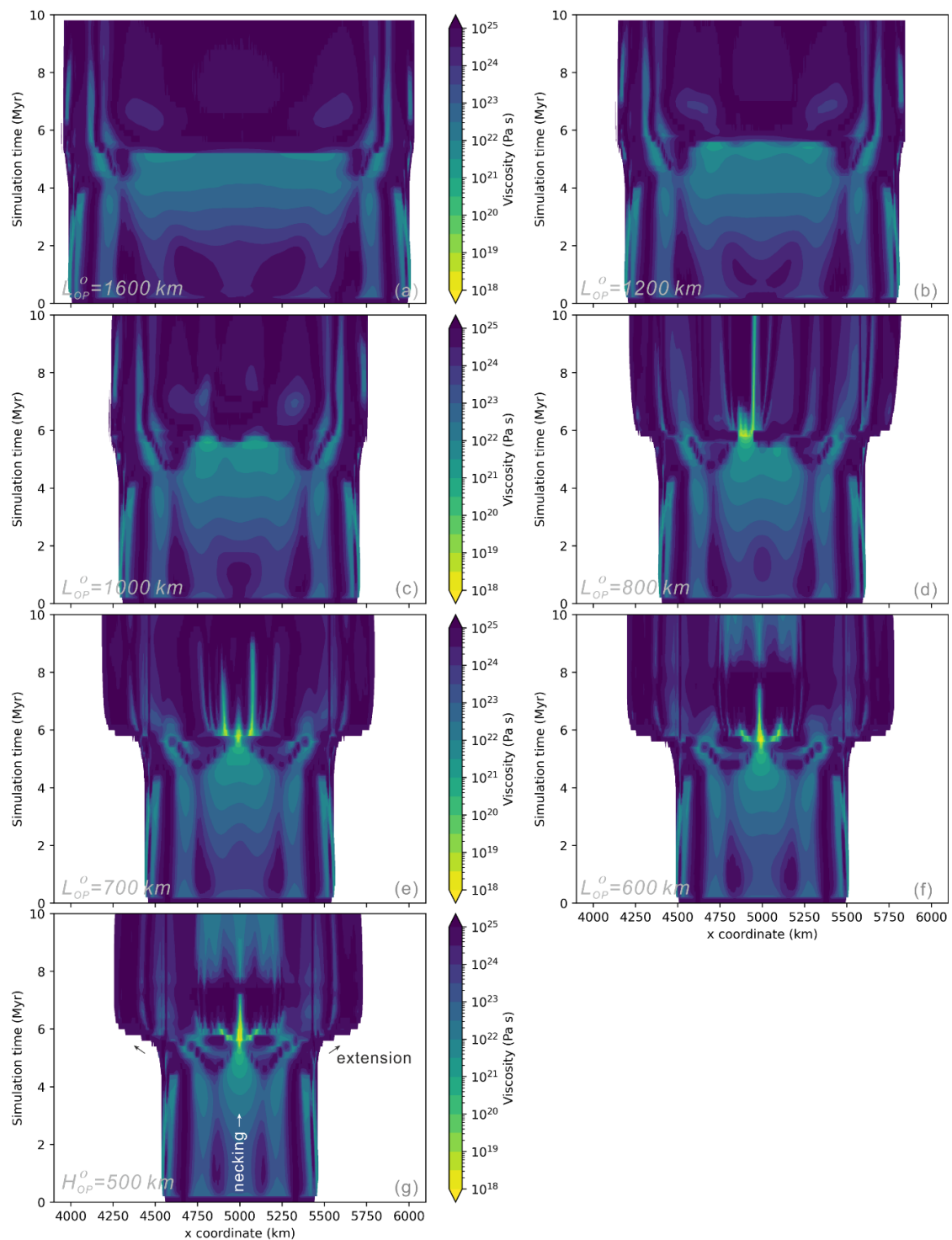
Figure 4.5 Temporal evolution of viscosity magnitude along the depth of 5 km within the overriding plate for models with different length of the overriding plate. (a) Model '$L_{OP}^0 = 1600\ km$'. (b) Model '$L_{OP}^0 = 1200\ km$'. (c) Model '$L_{OP}^0 = 1000\ km$'. (d) Model '$L_{OP}^0 = 800\ km$'. (e) Model '$L_{OP}^0 = 700\ km$'. (f) Model '$L_{OP}^0 = 600\ km$'. (g) Model '$L_{OP}^0 = 500\ km$'. All models have the same setup of H_{SP}^0 (141 km) and H_{OP}^0 (67 km). The edge of the filled contour in the lateral direction represents the interface between the overriding plate and subducting plate. The white arrows display the necking process of the overriding plate.

Apart from the necking regions that may develop into rifting extension within the overriding plate, there are some secondary necking regions developed close to the trench (Figure 4.5). The maximum weakening level is 'II' in these secondary necking regions and the viscosity reduction stops after ~4 Myr into the simulation. The lateral distance away from the nearest trench of these secondary necking regions are equal, showing little correlation with the varying L_{OP}^0.

4.3.3   Thickness of the overriding plate

The second series of models increase the initial thermal thickness (defined by the 1300 K contour) of the overriding plate (H_{OP}^0) from 67 km to 100 km (Figure 4.6), while keeping the subducting plate's thickness (H_{SP}^0) and the length of the overriding plate (L_{OP}^0) constant (Table 4.1). As H_{OP}^0 increases, the maximum weakening level developed within the overriding plate drops from 'IV' ($H_{OP}^0 = 67\ km$) to 'III' ($H_{OP}^0 = 74\ km$) and less than 'I' ($H_{OP}^0 = 100\ km$). The time it takes to lower each order of viscosity magnitude increases, indicating a slower progressive weakening.

Figure 4.6 Progressive weakening, illustrated by visualising the stress σ_{xx}, of the overriding plate during dual inward dipping subduction with increasing thickness of the overriding plate, (a) model '$H_{OP}^0 = 67\ km$', (b) model '$H_{OP}^0 = 74\ km$' and (c) model '$H_{OP}^0 = 100\ km$'. A detailed explanation of the contours and symbols could be found in the caption of Figure 4.3.

Besides, the total extension decreases from ~600 km ($H_{OP}^0 = 67\ km$, Figure 4.7, a) to ~350 km ($H_{OP}^0 = 70\ km$, Figure 4.7, b) and ultimately to ~0 km ($H_{OP}^0 = 100\ km$, Figure 4.7, c-e). The maximum viscosity reduction in both the primary and secondary necking

regions decreases as H_{OP}^0 increases, while the lateral distance away from the trench of necking regions are equal, showing no correlation with H_{OP}^0.

Figure 4.7 Temporal evolution of viscosity along a horizontal line at the depth of 5km in the overriding plate. (a) Model '$H_{OP}^0 = 67\ km$'. (b) Model '$H_{OP}^0 = 70\ km$'. (c) Model '$H_{OP}^0 = 74\ km$'. (d) Model '$H_{OP}^0 = 77\ km$'. (e) Model '$H_{OP}^0 = 100\ km$'. All models have the same H_{SP}^0 (141 km) and L_{OP}^0 (500 km). The edge of the contour filling in the lateral direction represents the interface between the overriding plate and subducting plate.

To investigate the details of the progressive weakening in the necking region, 6 diagnostics are evaluated along the vertical slice in the middle of the overriding plate. This is where the necking belt develops in models with L_{OP}^0 of 500 km. The diagnostics are integrated along the vertical slice and then divided by the thickness of the plate (Equation (4.3)),

$$\overline{D} = \frac{1}{H_{OP}} \int_0^{H_{OP}} D \ dy, \tag{4.3}$$

in which D represent the diagnostic. The averaged results include magnitude of viscosity ($\bar{\mu}$), second invariant of strain rate ($\overline{\dot{\varepsilon}_{II}}$), lithosphere thickness ($\overline{d_{OP}}$), horizontal stretching stress component ($\overline{\sigma_{xx}}$), vertical velocity component ($\overline{v_y}$), and temperature ($\bar{T}$).

Take the model '$H_{OP}^0 = 67 \ km$' for example (blue line), the evolution of the 6 diagnostics during dual inward subduction is analysed (Figure 4.8). There is linear increase of $\overline{\dot{\varepsilon}_{II}}$ and $\overline{\sigma_{xx}}$, and linear decrease of $\bar{\mu}$ during the simulation between 1 Myr to 4 Myr. While $\overline{d_{OP}}$, $\bar{T}$ and $\overline{v_y}$ remains nearly constant. From 4 Myr to 5 Myr, $\overline{\dot{\varepsilon}_{II}}$ and $\bar{\mu}$ keep a similar linear trend as before. But $\overline{\sigma_{xx}}$ stops increasing and starts to decrease gently. $\overline{v_y}$ starts to increase and $\overline{d_{OP}}$ starts to decrease, while $\bar{T}$ experiences little change. During the rifting and spreading extension between 5 Myr to 6 Myr, all diagnostics are varying more rapidly, with $\bar{\mu}$, $\overline{d_{OP}}$ and $\overline{\sigma_{xx}}$ dropping and $\overline{\dot{\varepsilon}_{II}}$, $\overline{v_y}$ and $\bar{T}$ climbing steeply. Afterwards, the model enters the steady state subduction stage, and the weakening process is replaced by a healing process where $\bar{\mu}$ and $\overline{d_{OP}}$ both increase while $\overline{\dot{\varepsilon}_{II}}$ and $\overline{v_y}$ decrease gradually.

As the thickness of the overriding plate increases from 67 km to 100 km, the magnitude of viscosity drop in the necking area decreases. In detail, the plotting shows that if $\bar{\mu}$

in the necking area of the overriding plate is above $\sim 2 \times 10^{22} \, Pa \cdot s$ (Figure 4.8, a, grey dashed line), there is no lithospheric thinning in the necking region (Figure 4.8, c, purple and red lines). In the timesteps when $\bar{\mu}$ is in the range of $10^{21} \sim 2 \times 10^{22} \, Pa \cdot s$, thinning starts to build up, but it's not weak enough to have rifting extension (Figure 4.8, c, green line). Only when the $\bar{\mu}$ drops below $10^{21} \, Pa \cdot s$ does significant thinning develop within the overriding plate (Figure 4.8, c, blue and orange lines). The results of $\bar{\mu}$ confirms that the iso-viscous contour $10^{21} \, Pa \cdot s$ can be used to predict if rifting or spreading extension develops during the dual inward subduction. It also reveals a more precise maximum viscosity below which the thinning of lithosphere develops.
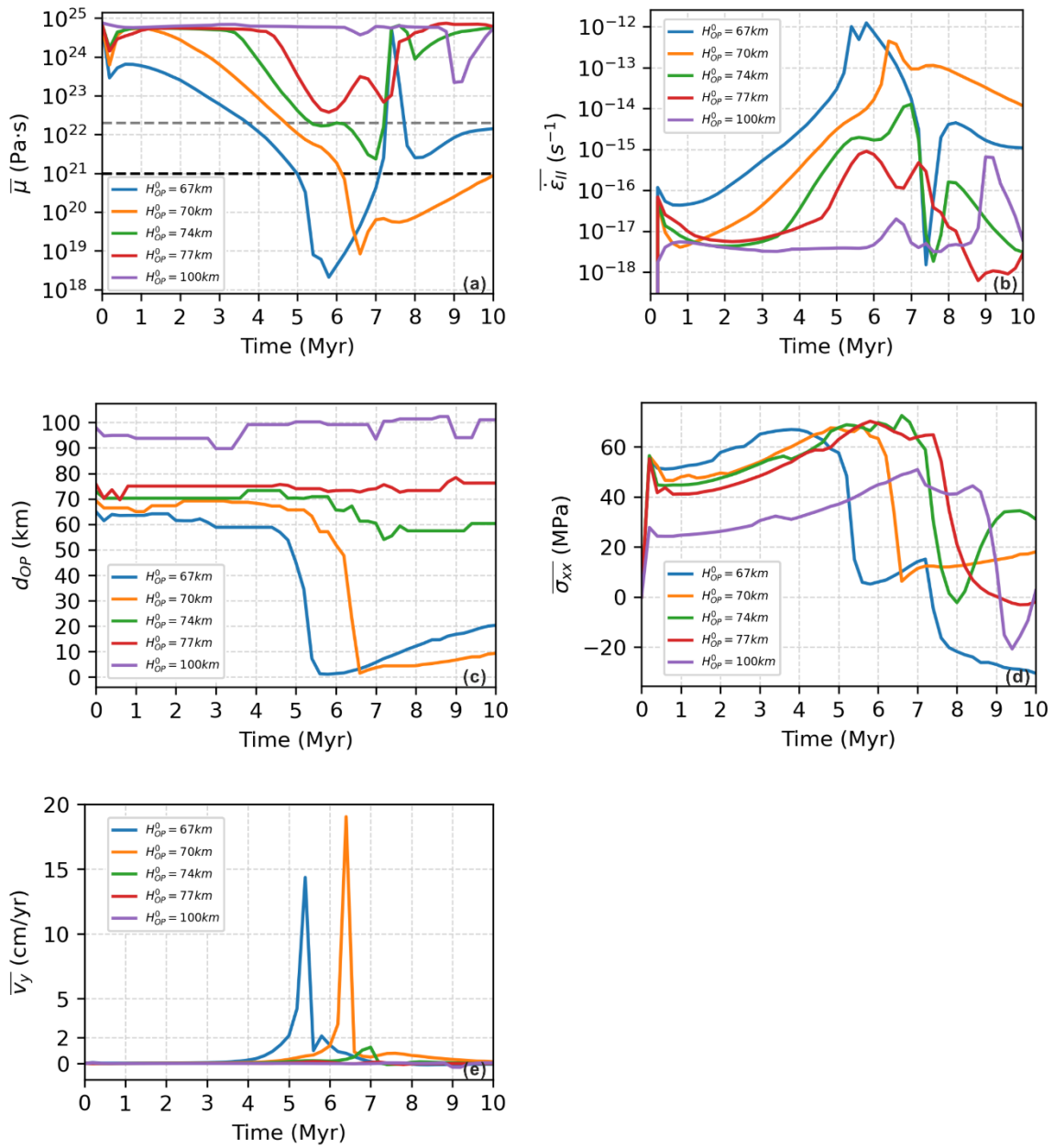
Figure 4.8 Temporal evolution of averaged diagnostics along the vertical slice in the middle of the overriding plate, (a) viscosity ($\bar{\mu}$), (b) second invariant of strain rate ($\overline{\dot{\varepsilon}_{II}}$), (c) lithosphere thickness ($\overline{d_{OP}}$), (d) horizontal stretching stress component ($\overline{\sigma_{xx}}$), and (e) vertical velocity component ($\overline{v_y}$). Positive value of $\overline{v_y}$ represent upward motion.

4.3.4 Thickness of the subducting plate

The third series of models investigate increasing the initial thermal thickness (again as defined by the 1300 K contour) of the subducting plate (H_{SP}^0) from 94 km to 141 km

(Figure 4.9), while keeping the overriding plate's thickness (H^0_{OP}) and the length of the overriding plate (L^0_{OP}) constant. As H^0_{SP} increases, the maximum weakening level developed within the overriding plate increases from 'I' ($H^0_{SP} = 94\ km$) to 'III' ($H^0_{SP} = 122\ km$) and 'IV' ($H^0_{SP} = 141\ km$). The time it takes to lower each order of viscosity magnitude decreases, indicating a faster progressive weakening.
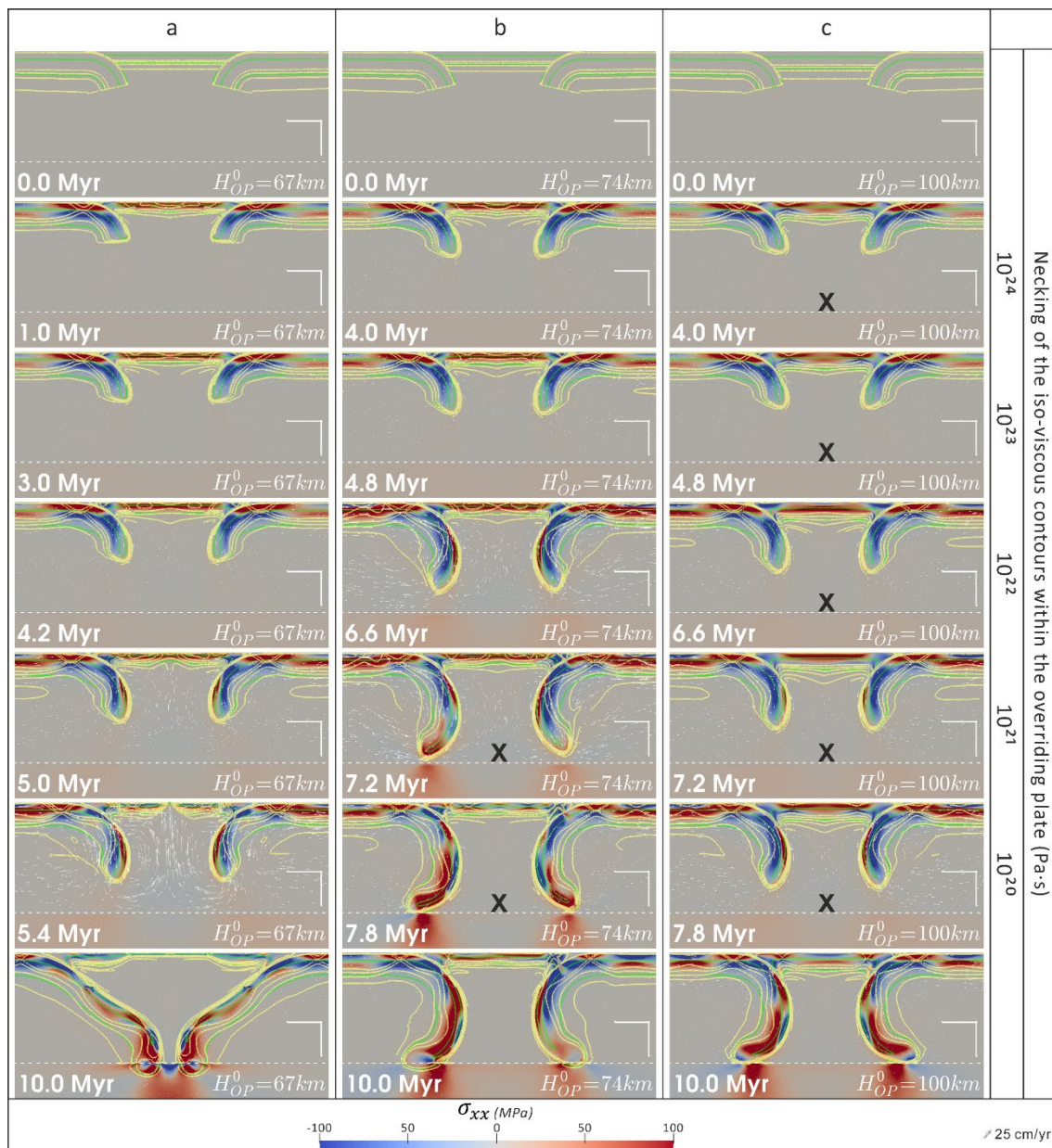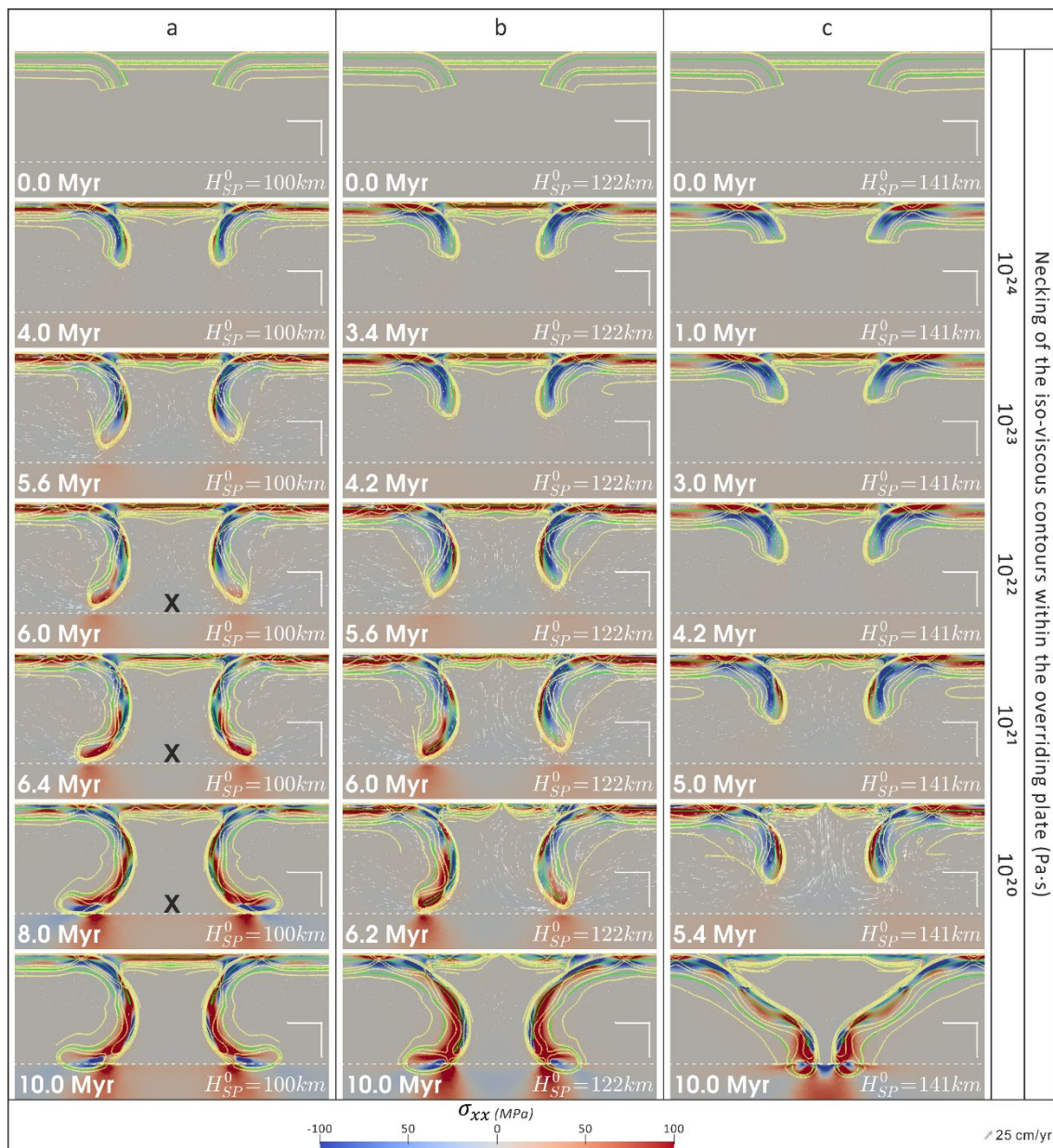

Figure 4.9 Progressive weakening of the overriding plate during dual inward subduction with increasing age of the subducting plate. (a) Model '$H^0_{SP} = 100\ km$'. (b) Model '$H^0_{SP} = 122\ km$'. (c) Model '$H^0_{SP} = 141\ km$'. A detailed explanation can be found in the caption of Figure 4.3.

Besides, the total extension increases from ~0 km ($H^0_{SP} \leq 111\ km$, Figure 4.10, a-c) to ~200 km ($H^0_{SP} = 122\ km$, Figure 4.10, d) and ultimately to ~600 km ($H^0_{SP} = 141\ km$, Figure 4.10, e). The maximum viscosity reduction in both the primary and secondary necking regions increases as H^0_{SP} increases, while the lateral distance away from the trench of necking regions are equal, showing little correlation with H^0_{SP}.
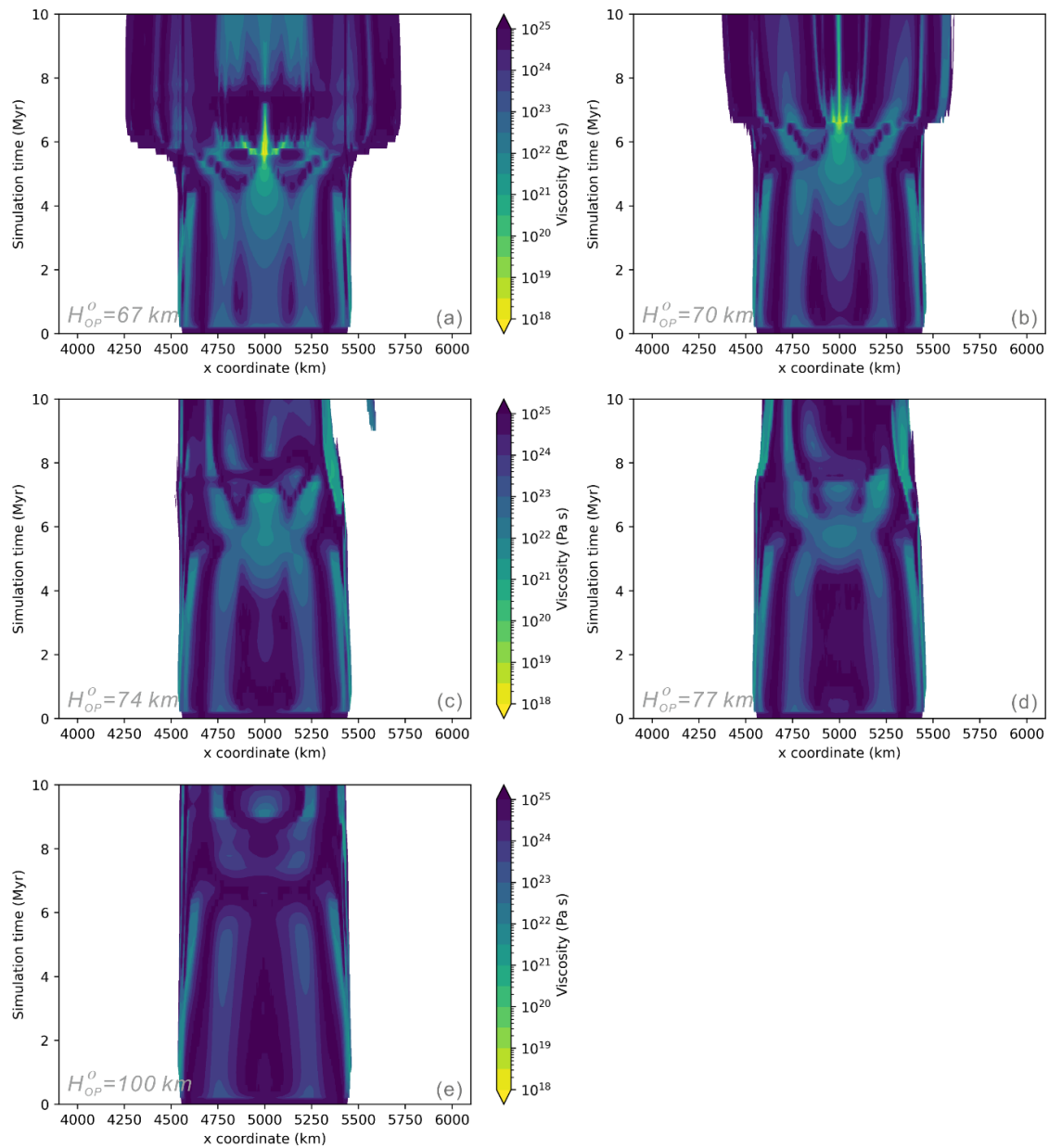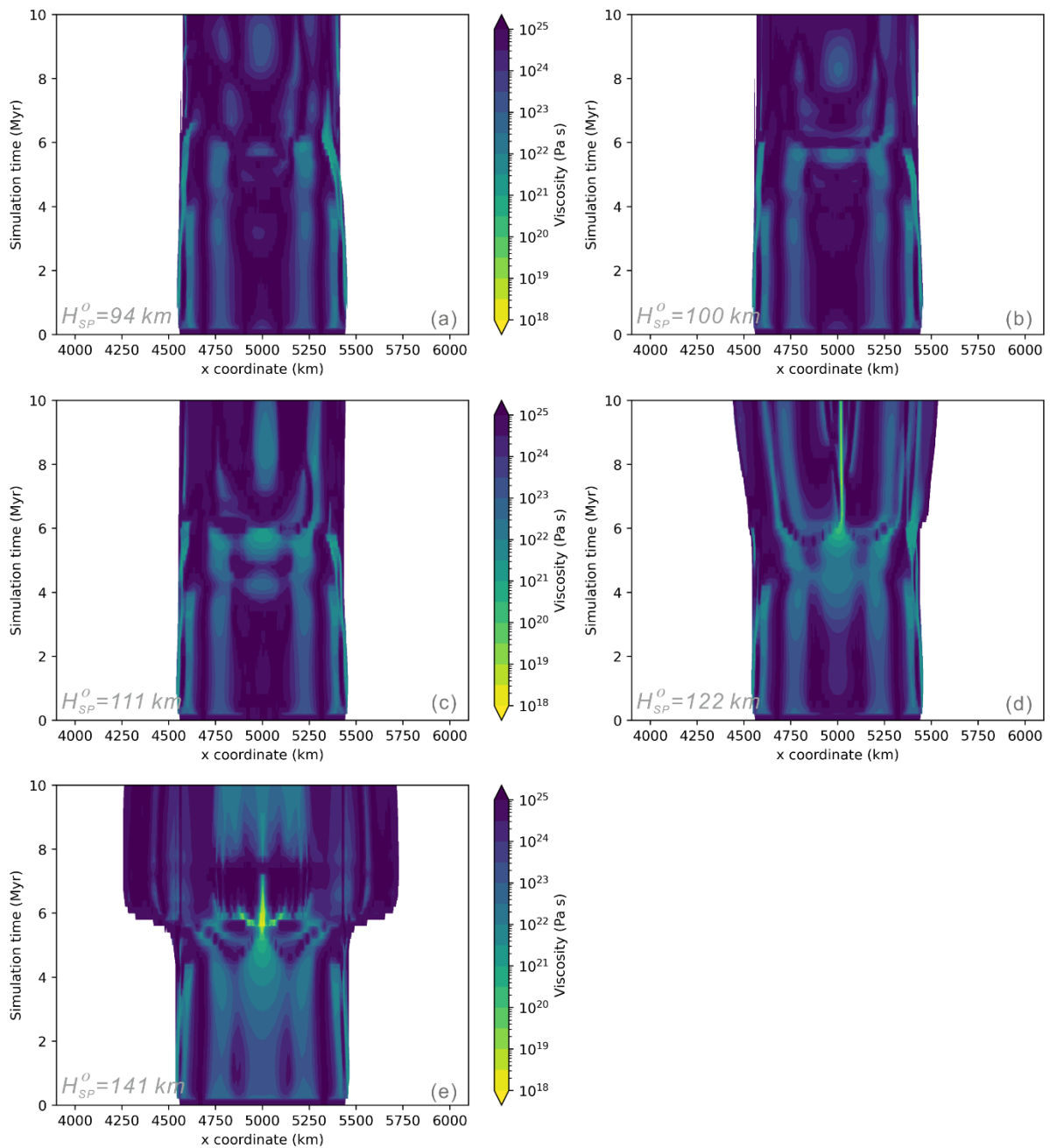
Figure 4.10 Temporal evolution of viscosity along a horizontal line at the depth of 5km in the overriding plate. (a) Model '$H_{SP}^0 = 94\ km$'. (b) Model '$H_{SP}^0 = 100\ km$'. (c) Model '$H_{SP}^0 = 111\ km$'. (d) Model '$H_{SP}^0 = 122\ km$'. (e) Model '$H_{SP}^0 = 141\ km$'. Both models have the same H_{OP}^0 (67 km) and L_{OP}^0 (500 km). The edge of the contour filling in the lateral direction represents the interface between the overriding plate and subducting plate.

4.3.5 Regime of stretching state

A variety of deformation patterns and stretching state within the overriding plate have been observed when varying L_{OP}^0, H_{OP}^0 and H_{SP}^0. Several diagnostics are reported together to quantify the deformation developed within the overriding plate during the 10 Myr simulation (Table 4.2). The detail of each diagnostic is described as follows.

Table 4.2 Summary of diagnostics for all models.

Model name	weaken level	t_{rift} (Myr)	t_{660} (Myr)	$\bar{v}_{sink}$ (cm/yr)	l_{n2n} (km)	l_{n2t} (km)	total strain
$H_{SP}^0 = 94\ km$	I	-	6.6	7.0	0	341	1%
$H_{SP}^0 = 100\ km$	III	-	6.4	7.2	0	341	2%
$H_{SP}^0 = 111\ km$	III	-	6.4	7.2	0	341	21%
$H_{SP}^0 = 122\ km$	IV	6.2	6.4	7.2	0	341	110%
$H_{SP}^0 = 141\ km$	IV	5.4	6.0	7.7	0	341	2800%
$H_{OP}^0 = 67\ km$	IV	5.4	6.0	7.7	0	341	2800%
$H_{OP}^0 = 70\ km$	IV	6.4	6.6	7.0	0	341	1300%
$H_{OP}^0 = 74\ km$	III	-	7.2	6.4	0	341	30%
$H_{OP}^0 = 77\ km$	II	-	7.6	6.1	0	341	4%
$H_{OP}^0 = 100\ km$	I	-	8.8	5.2	0	341	1%
$L_{OP}^0 = 500\ km$	IV	5.4	6.0	7.7	0	341	2800%
$L_{OP}^0 = 600\ km$	IV	5.4	6.0	7.7	0	384	690%
$L_{OP}^0 = 700\ km$	IV	5.6	6.0	7.7	0	371	630%
$L_{OP}^0 = 800\ km$	IV	5.8	6.0	7.7	231	364	14%[a]
$L_{OP}^0 = 1000\ km$	III	-	6.0	7.9	282	369	15%
$L_{OP}^0 = 1200\ km$	III	-	5.8	7.9	621	370	11%
$L_{OP}^0 = 1600\ km$	II	-	5.4	8.5	937	411	4%

[a] The total strain listed here is calculated along the middle vertical slice (5000 km away from side boundaries). For models $L_{OP}^0 \geq 800\ km$, the necking zones are away from this middle vertical slice. So, the total strain could be underestimated for these models. Considering that only model '$L_{OP}^0 = 800\ km$' achieved weakening level 'IV', the corrected total strain along its necking zone is ~600%. While the underestimation for other models is moderate and will not change the conclusion of this research.

As introduced in section 4.3.1.1, weakening levels 'I', 'II', 'III', 'IV' are determined by the minimum viscosity contour which is necked in the overriding plate during subduction. The higher the weakening level, the stronger the localised rheology modification observed within the overriding plate. All three groups of dual inward dipping subduction models manage to yield a variety of weakening levels in the overriding plate (Figure 4.11, a-c).

t_{rift} indicates the timestep when the overriding plate develops rifting extension (weakening level 'IV'), and a void value means that model fails to generate rifting extension within the overriding plate. It shows that only models achieving weakening level 'IV' develop rifting extension. t_{rift} increases with thicker or longer overriding plate, and decreases with thicker subducting plate.

t_{660} equals how much time the subducting plate (defined by its 1300 K isotherm) takes to sink to the depth of 660km. It is most sensitive to the variation of H_{OP}^0, while varying L_{OP}^0 and H_{SP}^0 generates less than ~1 Myr difference of t_{660} compared with a ~3 Myr difference when modifying H_{OP}^0. $\bar{v}_{sink}$ equals 460 km (the vertical distance from the initial slab tip depth to the depth of 660 km) divided by t_{660}. $\bar{v}_{sink}$ ranges from 5.2 to 8.5 cm/yr and the magnitude does not correlate with the weakening level or t_{rift}, i.e., high sinking rate does not necessarily lead to higher weakening level or faster rifting extension.

l_{n2n} is the horizontal distance between necking centres which may develop rifting extension during dual inward dipping subduction, i.e., secondary necking regions are excluded. The value of l_{n2n} is 0 km if there is only one necking centre within the overriding plate. l_{n2n} starts to increase with L_{OP}^0 when L_{OP}^0 is greater than ~700 km. l_{n2n} in Table 4.2 is recorded at the timestep of 4.4 Myr. It should be noted that, l_{n2n} may vary with time and the difference is at most ~250 km (Figure 4.5).

l_{n2t} marks the lateral distance from the centre of the necking area to its nearest trench at the 4.4 Myr timestep. For all simulations, l_{n2t} is in a narrow range of ~340-410 km and the variation is likely to originate from the fact that l_{n2t} is also time dependent. Since the average sinking rate is different for these models, different models may behave differently at the same timestep.

Total strain is calculated by integrating the average strain rate ($\overline{\dot{\varepsilon}_{II}}$ based on Equation (4.3)) with time throughout the 10 Myr simulation. All three groups of models generate a variety of total strain at the end of the simulation. For all models that develop rifting extension, the total strain is greater than 100%. Total strain in the range of 5% to 100% is observed from limited thinning up to significant extension. For models where the total strain is less than 5%, the weakening deformation is hardly observable in the overriding plate.
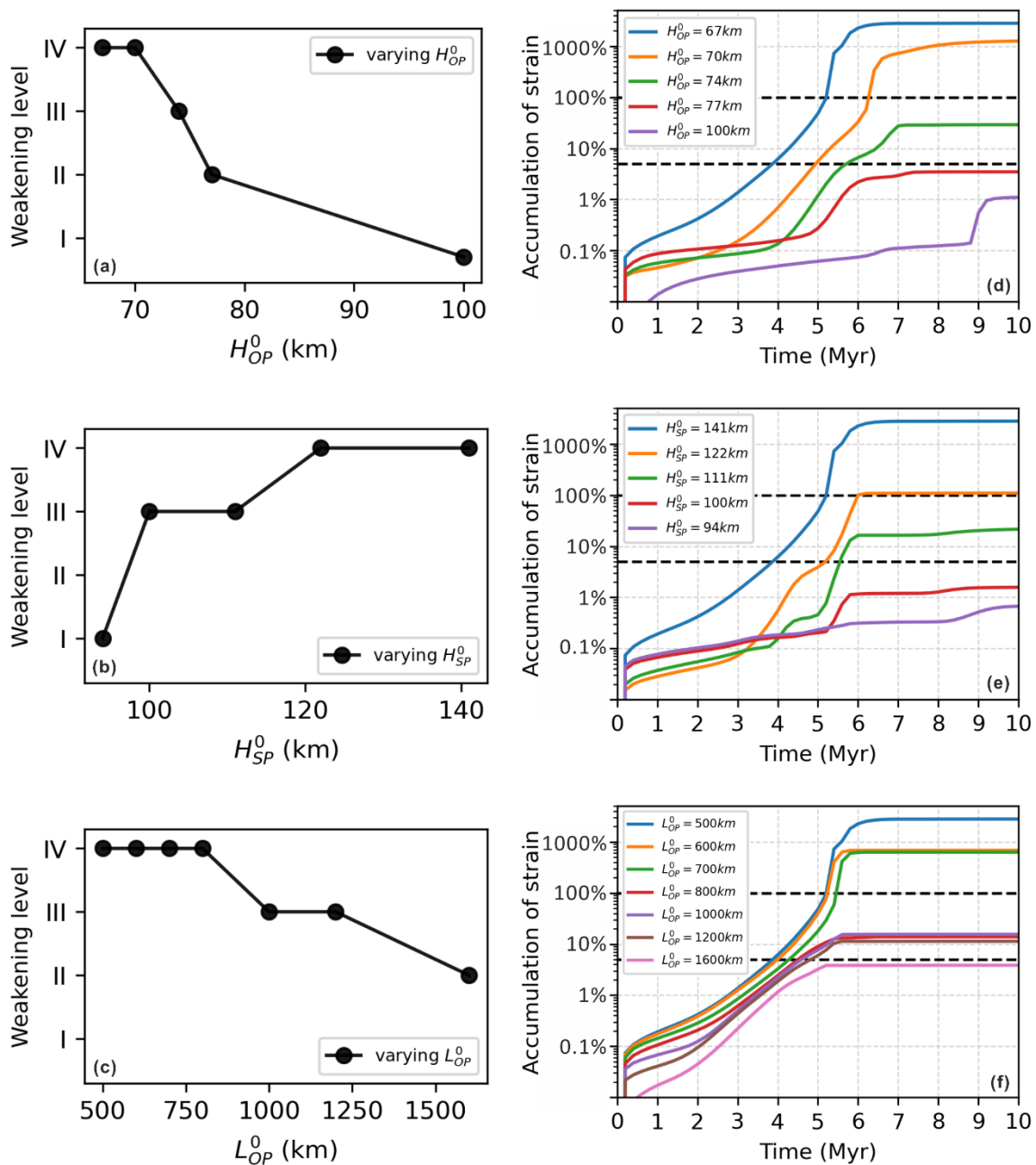
Figure 4.11 Key diagnostics used to characterise the rheology modification within the overriding plate. (a-c) Weakening level developed within the overriding plate. (d-f) Accumulation of strain in the middle of the overriding plate (5000 km away from the side boundaries).

By combing all the qualitative and quantitative diagnostics presented in these results, three stretching states are classified: 1) little or no lithosphere thinning and extension, discriminated by low weakening level up to level 'II', little total strain up to 5% and

almost no thermal lithosphere thinning in the necking area; 2) limited lithosphere thinning and extension, identified by medium weakening level up to level 'III', medium total strain up to 30%, and limited thermal lithosphere thinning, e.g., ~15 km thinning for model '$H_{OP}^0 = 74 \, km$' (Figure 4.8, c); 3) rifting and spreading extension, characterised by high weakening level up to level 'IV', high total strain over 100%, and total thinning of the thermal lithosphere during rifting extension.

4.4   Discussion

The results show that the non-steady state subduction provides a time window to develop progressive weakening within a uniform overriding plate. With appropriate conditions, tested in this research, e.g., thick enough H_{SP}^0, thin enough H_{OP}^0, short enough L_{OP}^0, different levels of stretching state, ranging from no thinning nor extension to rifting and spreading extension, can develop within the homogeneous overriding plate. The role that dual inward dipping subduction plays during the progressive weakening and the origin of the softening process are worth discussion.

4.4.1   The role dual inward subduction plays

4.4.1.1   Creating fixed trailing boundary condition for the overriding plate

Due to the symmetric model setup, subducting plates on both sides are prone to advance or retreat simultaneously. This creates roughly equal and symmetric competing force from both ends of the overriding plate during subduction. As a result, the mobility of the overriding plate is inhibited, and in comparing to single-sided subduction, it would be as if the mechanical boundary condition on the overriding plate was fixed (Figure 4.12, a-c). This helps cultivating an ever-increasing stretching stress

field and forming localised necking weak zones within the middle plate during non-steady state subduction. This is unlike the single sided subduction cases, where the mobile overriding plate can move as a whole to slow down the build up of deviatoric stress within the plate (Garel et al., 2014). Thus, the lack of mobility of the overriding plate plays a key role in the weakening process during the symmetric dual inward dipping subduction.
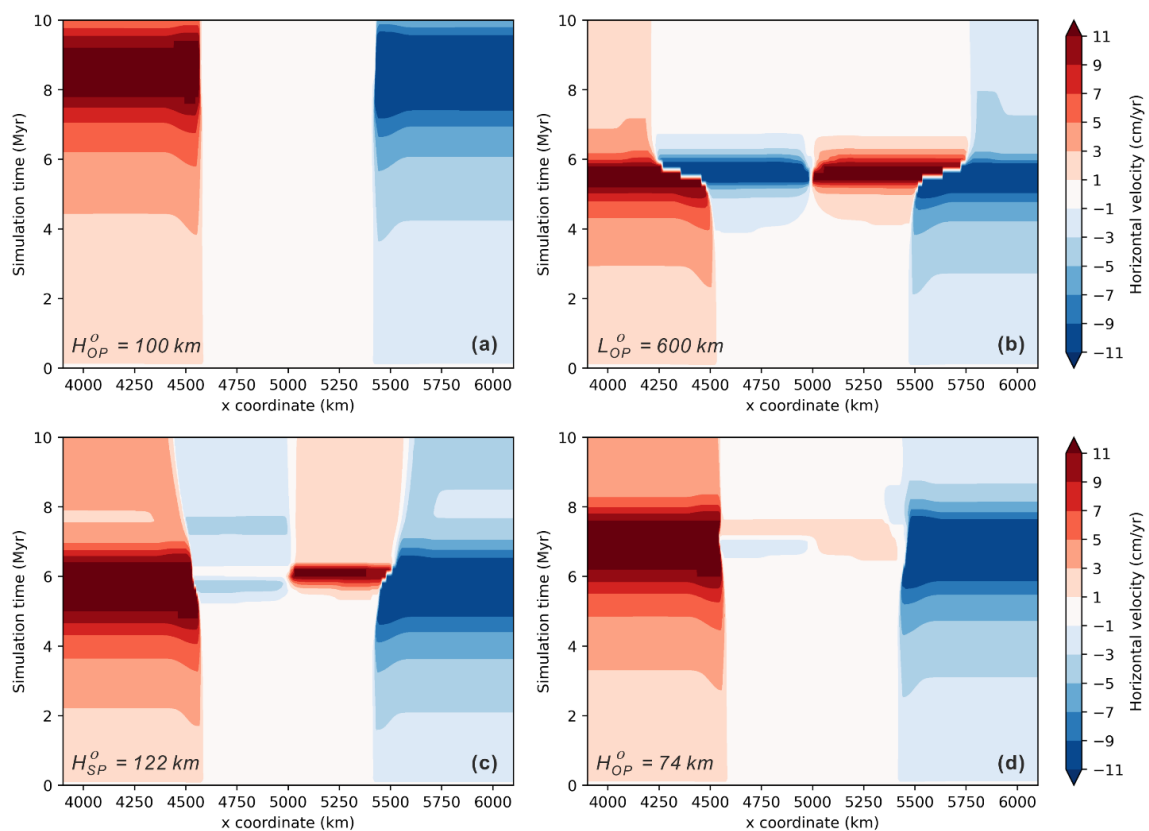
Figure 4.12 Temporal evolution of horizontal velocity along a lateral slice, x coordinate from 3900km to 6100 km, at the depth of 20 km from the surface. (a) model '$H_{OP}^0 = 100\ km$', (b) model '$L_{OP}^0 = 600\ km$', (c) model '$H_{SP}^0 = 122\ km$', (d) model '$H_{OP}^0 = 74\ km$'. The contour filling represents the variation of horizontal component of velocity vector throughout the 10 Myr simulation. Positive value means right-ward motion and negative value is left-ward motion. The white area represents that the plate is nearly stagnant. And the edge of the white area marks the interface between the subducting plate and overriding plate or rifting and spreading centre within the overriding plate.

The fixed boundary condition environment is likely to be favoured as long as on both sides the slab has symmetric trench motion tendencies. Once one side is prone to advance, or move slower than the other, then the fixed boundary condition effect is likely to weaken and the magnitude of the velocity of the overriding plate can increase from ~0 cm/yr to 1-3 cm/yr (Figure 4.12, d). But still, the overriding plate is not as mobile as a free mobile boundary condition in single subduction models, where the overriding plate can move as fast as 5 cm/yr or more during the non-steady state subduction.

In previous subduction models, a fixed boundary condition is achieved on the overriding plate by extending the overriding plate to the side boundary and applying a fixed velocity to the plate. It is suggested that such a boundary condition is responsible for the increased degree of deformation in the overriding plate compared with mobile plates (Chen et al., 2016; Erdős et al., 2021; Yang et al., 2019). A comparable effect is achieved by bringing in another subducting plate at the other end of the overriding plate. The fixed boundary condition effect is also observed in previous dual inward dipping subduction models (Dasgupta and Mandal, 2018; Holt et al., 2017; Lyu et al., 2019), but its role in affecting the weakening of the overriding plate was not addressed since the viscosity was only composition-dependent and did not change with evolving stress or temperature.

4.4.1.2   Stronger poloidal return flow

The result shows that varying the size of the plate can affect the degree of extension within the overriding plate. Previous research shows that subduction can induce poloidal mantle return flow, which has been suggested to account for extensional deformation within the overriding plate, e.g. back-arc extension, supercontinent breakup (Chen et al., 2016; Dal Zilio et al., 2018; Sleep and Toksöz, 1971). Single

sided subduction modelling indicates: a) increasing the thickness of the subducting plate (H_{SP}^0) can increase the net negative buoyancy which is proportional to slab pull force, thus leading to a stronger poloidal flow (Figure 3.7); b) lowering the thickness of the overriding plate (H_{OP}^0) can not only increase the net negative buoyancy by increasing the hanging slab area in the upper mantle, but also reduces the resistance during subduction along the interface between two plates (Erdős et al., 2021). These two mechanisms also come into play for dual inward dipping subduction models.

In addition, dual inward dipping subduction models can yield a third way to strengthen the return flow. This is by combining the two separate poloidal convection flows, one from each subducting plate, as the length of the overriding plate (L_{OP}^0) shortens (Figure 4.4). This is shown for example by the velocity variation in both the horizontal (v_x) and vertical (v_y) direction at the depth of 75 km (Figure 4.13). For all dual inward dipping subduction models, the magnitude of v_x decreases gradually from ~2.5 cm/yr in the mantle wedge corner to 0 cm/yr underlying the middle part (~5000 km away from side boundaries) of the overriding plate (Figure 4.13, a). As L_{OP}^0 changes, models with shorter overriding plate have greater v_x gradient along the lateral slice (Figure 4.13, b). The maximum magnitude of v_y increases from ~0.25 cm/yr to ~1.3 cm/yr, implying a faster upwelling flow, as the length of the overriding plate (L_{OP}^0) shortens (Figure 4.13, c-d). It is also noted that the necking area developed within the overriding plate (eg. Figure 4.4) lies right above the maximum upwelling component of the return flow (Figure 4.13, c). The observation indicates a spatial correlation between the stronger poloidal return flow and the progressive weakening in the overriding plate.
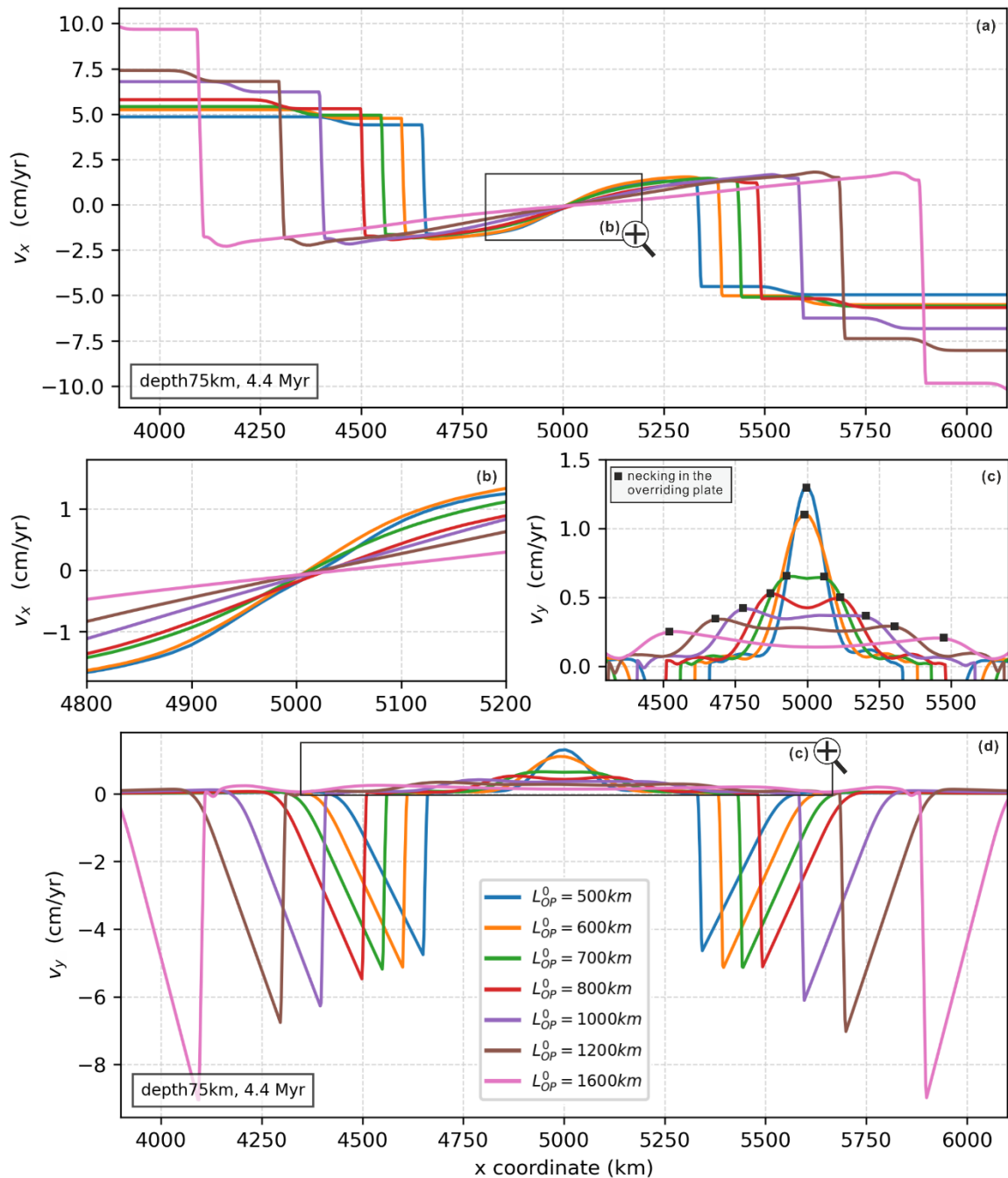
Figure 4.13 Velocity variation along a slice at the depth of 75 km, which is ~8 km below the 1300 K isotherm of the overriding plate, after 4.4 Myr simulation. (a, d) Horizontal and vertical component of velocity along the slice. (b) and (c) are zoom-in of (a) and (d) under the middle part of the overriding plate (5000 ± 200 km and 5000 ± 650 km away from the side boundaries respectively). Positive value means rightward or upward motion, and negative value represents leftward or downward motion. In (c), the horizontal coordinate of the necked region in the overriding plate is plotted as black square to visualize its spatial correlation with upwelling component of mantle wedge flow. All plots share the same legend listed in (d).

Previous research on subduction-induced continental breakup implies that spreading extension develops above where the upwelling mantle flow diverges, flow which creates the highest shear stress gradient at the bottom of the overriding plate (Dal Zilio et al., 2018). This does not fully agree with the simulation results with varying L_{OP}^0 here. The divergent return flow is defined as the place where v_x changes direction. It always lies under the middle part (~5000 km away from the side boundaries) of the overriding plate for all models (Figure 4.13, a). However, the weakening area does not always develop in the middle of the overriding plate, e.g., when $L_{OP}^0 \geq 800\ km$. Instead, it correlates better in space with the highest upwelling mantle flow velocity (Figure 4.13, c). The lateral distance from the highest upwelling component to the nearest trench is measured (Figure 4.13, d), and it is noted that the distance remains relatively constant at ~370 km for all models at 4.4 Myr. This suggests that the wavelength of the slab induced mantle wedge flow is not related with varying L_{OP}^0. Others have found that the wavelength of the mantle wedge flow is strongly controlled by the depth to the viscosity jump at the upper-lower mantle boundary (Dal Zilio et al., 2018; Toksöz and Hsui, 1978). Investigating the impact of varying the rheology parameters on the length scale of this flow is a topic for future work.

An interesting observation is that the subducting slab's sinking velocity increases (t_{660} decreases) with longer L_{OP}^0 (Table 4.2), while the poloidal mantle flow gets weaker and the maximum weakening level in the overriding plate decreases. From the perspective of energy conservation, all the dynamic processes, e.g., plate motion, mantle convection, internal deformation etc., originates from the potential energy of the subducting slabs. This implies that more of the potential energy transfers into kinetic energy of the subducting plates instead of being consumed as dissipation energy in the overriding plates, as L_{OP}^0 increases.

4.4.2 Overriding plate weakening mechanism

As introduced in the methods, this research applied composite rheology which incorporates four deformation mechanisms everywhere in the simulation domain. Here, the dominant deformation mechanism (DDM) is defined as the rheology law that yields the minimum magnitude of viscosity at a certain point. The first subsection tries to understand the temporal and spatial evolution of the DDM within the overriding plate, especially in the region where strain localisation takes place. The second subsection tries to evaluate the contribution of each deformation mechanism in promoting strain localisation within the overriding plate.

4.4.2.1   Dominant deformation mechanism analysis

The reference model '$L_{OP}^0 = 1200\ km$' with limited extension has shown that the DDM is stratified with yielding, Peierls creep and dislocation creep as the depth increases within the overriding plate (Figure 4.3, b). Here, further investigation is conducted to understand how the DDM evolves in models that develop rifting and spreading extension within the overriding plate, e.g., model '$H_{OP}^0 = 70\ km$'. Therein, the temporal phases show that the DDM is also spatially layered (Figure 4.14), with yielding initially dominating from the surface to the depth of ~35 km, underlain by Peierls creep dominating for the next ~10 km and then dislocation creep dominating for ~25 km (Figure 4.14, b-d). Among all the DDM at different depths throughout the simulation, yielding is always the thickest and dislocation creep comes as the second. To be noted, the DDM of diffusion creep with limited area is observed around the bottom of the overriding plate during the initial plate weakening (Figure 4.14, b), and it is completely replaced by dislocation creep after 3.6 Myr. During the thinning process of the overriding plate, the deformation mechanism of Peierls creep gives way to yielding

and dislocation creep as DDM (Figure 4.14, d-g). The replacement and interplay among different DDM will be discussed in the next subsection. (Figure 4.14, a-b).
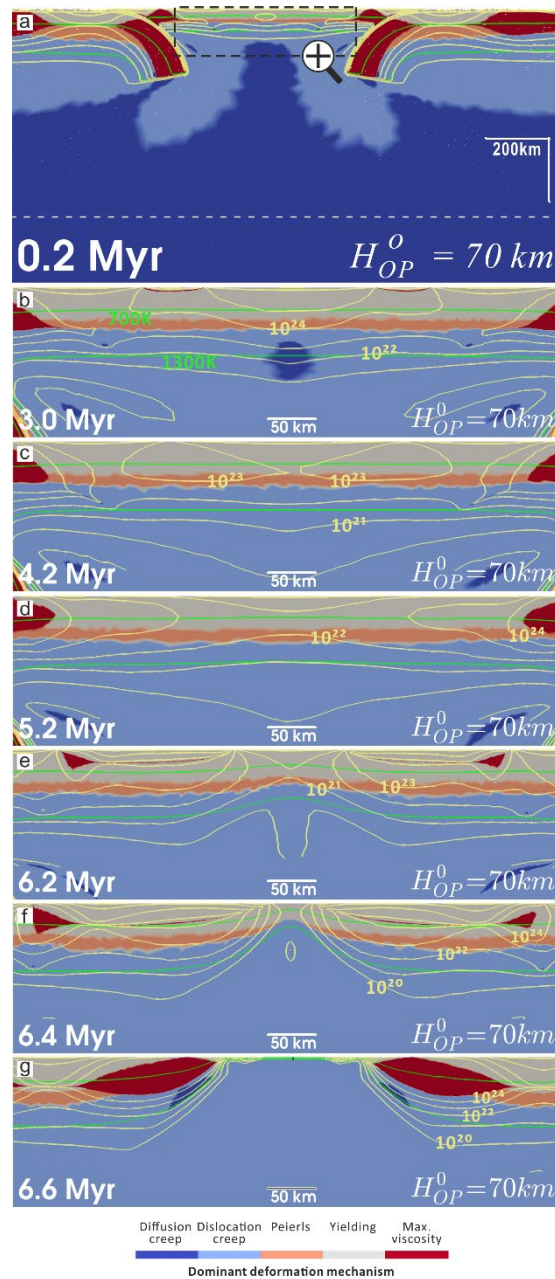
Figure 4.14 Temporal evolution of the dominant deformation mechanism within the overriding plate in model $H_{OP}^0 = 70\ km$. The dashed zoom-in block in (a) shows the location of screenshots in (b-g). The progressive weakening process within the overriding plate is demonstrated by the necking of the iso-viscous contours. The 5 groups of yellow contours encompassing the plates in each screenshot are iso-viscous contours of $10^{20}, 10^{21}, 10^{22}, 10^{23}, 10^{24}\ Pa \cdot s$ from outward to inward. The two sets of green solid lines are 700 K and 1300 K isotherm contours to image the geometry of the thermal plate. The bottom left corner caption shows the elapsed simulation time and bottom right corner is the name of the model.

While the models do not implement a multi-material approach to define the rheology of different layers in the lithosphere, the uniform compositional rheology law self-consistently generates the layered structure in Figure 4.14. In detail, yielding only dominates over other creep mechanisms in the cold regions, corresponding to the crustal depth range. While dislocation and diffusion creep dominate over yielding in the hot bottom region, equivalent to the depth range of mantle lithosphere. The continuous necking process shows that the viscosity reduction initiates from the surface (yielding) and the bottom of the plate (dislocation creep). Then the viscosity contour necks in the middle depth of the plate as seen in Figure 4.14, (b-e). This suggests that yielding and dislocation creep play the dominant role in promoting the continuous weakening of the overriding plate.

4.4.2.2 Weakening contribution analysis

The previous section has shown that the DDM may vary at different depth range within the overriding plate. To evaluate the contribution of each DDM to inducing rifting and spreading extension for each timestep, the overriding plate is sliced vertically through its middle where the most intensive necking takes place. Then the points along the midline are grouped by the type of DDM. Two kinds of calculation are conducted. 1) For the points with the same DDM, the arithmetic average of the strain rate and temperature state are calculated at each timestep. These two variables can be used to compute the viscosity through Equation (2.8). 2) The minimum viscosity among all points along the midline is calculated, and the DDM that yields the minimum viscosity is defined as the Minimum Viscosity Dominant Deformation Mechanism (MVDDM). To be clear, the DDM is calculated at each point independent of other points, while the MVDDM is calculated using all relevant points along the midline.

One diagnostic to evaluate the contribution of deformation mechanisms to plate weakening is to quantify how much (order of) viscosity reduction each DDM achieves. For model '$H_{OP}^0 = 70\ km$', both yielding and dislocation creep reduces the viscosity to lower than $10^{21}\ Pa \cdot s$ (Figure 4.15, a), which is the critical magnitude to initiate rifting and spreading extension (Figure 4.8, a). While Peierls creep can reduce viscosity to the range of 10^{21}-$10^{22}\ Pa \cdot s$, which can enable limited thinning but it fails to induce rifting extension. Diffusion creep induces the least viscosity reduction to ~$5 \times 10^{22}\ Pa \cdot s$, which suggests that it only softens the plate for further deformation through limited viscosity reduction. For models that do not develop rifting or spreading extension, the temporal paths of the DDM are similar with model '$H_{OP}^0 = 70\ km$' except that the minimum viscosity is never less than $10^{21}\ Pa \cdot s$. Another diagnostic to evaluate the contribution of deformation mechanisms to plate weakening is how long it stays active. It is noted that yielding and dislocation creep are two types of DDM that are active throughout the simulation (Figure 4.15, a), while diffusion creep and Peierls creep disappears as DDM along the midline after 3.6 Myr and 6.4 Myr separately (Figure 4.14, b, f).
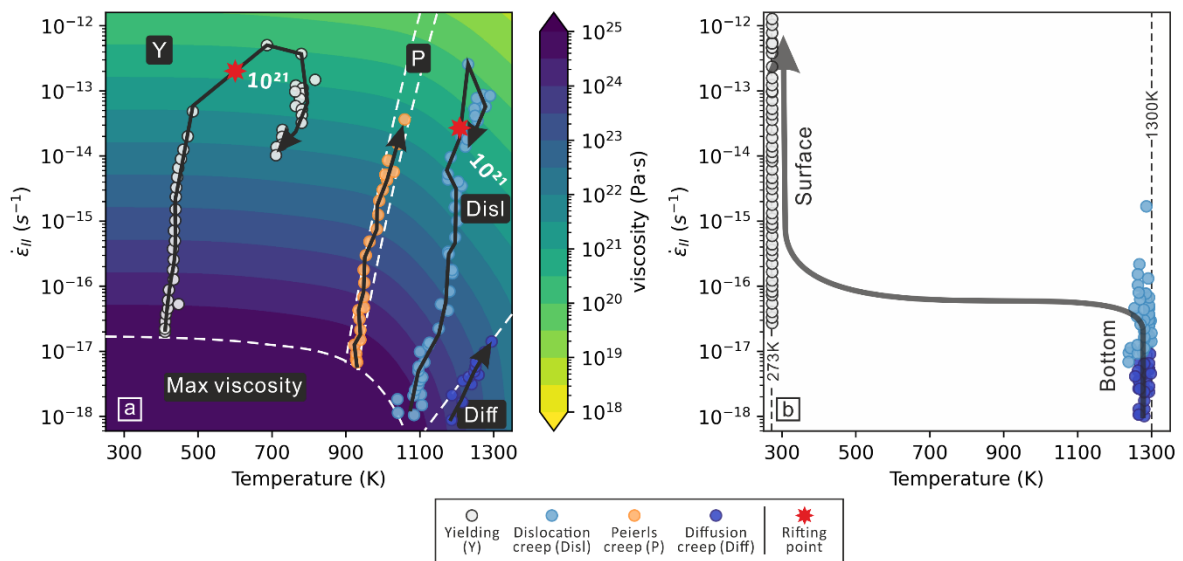
Figure 4.15 Scatter plots of the dominant deformation mechanism along the midline of the overriding plate (5000 km away from both side boundaries), i.e., the main necking region. (a) The temporal path of each dominant deformation mechanism (DDM) is plotted on a phase diagram, where the magnitude of viscosity is calculated based on Equation (2.7). The phase diagram is divided by the white dashed lines into four domains based on the calculation of which component deformation mechanism yields the minimum viscosity at the given strain rate, temperature and depth. The fifth domain marks the maximum viscosity. To be noted, the depth used to create the viscosity contour is 50 km, which may not reflect the complete temporal path, but it helps to demonstrate how viscosity will evolve. The scatter points are taken from the model '$H_{OP}^0 = 70\ km$', and each point is calculated by averaging the strain rate and temperature state at each timestep for the portion of the midline that holds the same dominant deformation mechanism. (b) The evolution of the dominant deformation mechanism that yields the minimum viscosity (MVDDM) throughout the midline of the overriding plate. Scatter points are taken from 5 models with varying thickness of the overriding plate (H_{OP}^0).

To be noted, an accelerating viscosity reduction in the range of 10^{20}-$10^{22}\ Pa \cdot s$ is observed for the DDM of yielding and dislocation creep (Figure 4.15, a). That is when plate thinning, rifting and spreading extension take place. The accelerating viscosity reduction suggests that the overriding plate falls into positive feedback weakening loops as strain localises in the necking region. Such self-strengthening weakening feedback loop when necking develops into rifting centre is also reported in previous research using power-law viscous creeping flow law with an exponent > 1 (Wenker and Beaumont, 2018). As in the case of uniaxial stretching, the plate strength is

proportional to $\bar{\mu} \times H_{OP}$ (Ribe, 2001), both of which in the models are reducing during the plate thinning process. Since the plate strength measures the very resistance to the underlying mantle flow, the reduction of viscosity and plate thickness will incur further plate weakening. The continuous plate strength reduction during dual inward dipping subduction may end up with the formation of new plate boundaries.

The location of the weakest point (with the least viscosity) along the midline migrates from the bottom of the overriding plate to the surface as dual inward dipping subduction proceeds (Figure 4.15, b). Correspondingly, the MVDDM changed from diffusion creep and dislocation creep at the bottom of the plate to yielding at the surface. Such a transition is observed no matter whether only rifting or full spreading extension develops within the overriding plate. The result indicates that the transition is enabled as long as the strain rate can keep increasing during subduction (Figure 4.15, b). Though, only a high enough strain rate ($\sim 10^{-13}\ s^{-1}$) can lower the viscosity ($\sim 10^{21}\ Pa \cdot s$) sufficiently through yielding and dislocation creep to induce rifting and spreading extension (Figure 4.15, a).

While the rheology law (Equation (2.8, 2.9)) of the four deformation mechanisms shows that the magnitude of viscosity is dependent on evolving temperature, strain rate, and lithostatic pressure, the diagram (Figure 4.15, a) indicates that the viscosity reduction is mainly driven by the ever-increasing strain rate relative to the much gentler impact of increasing thermal gradient and decreasing lithostatic pressure due to plate thinning. The dominant role of strain rate-induced weakening over thermal weakening is also reported in the interaction between upwelling plumes and overlying lithosphere (Burov and Guillou-Frottier, 2005). That is to say, the rheology and buoyancy parameters will be more important than the heat conduction parameters in producing different levels of rheology weakening within the overlying plate. The continuously growing strain rate can also explain the replacement of diffusion creep by dislocation

creep as the DDM at the bottom of the overriding plate. While the replacement of Peierls creep by yielding or dislocation creep as DDM during the plate thinning process is likely due to both increasing strain rate and temperature at the intermediate depth. In addition, the strain rate induced weakening is also a precondition to initiate thermal weakening, lithosphere thinning, strain localisation and formation of new plate boundaries (eg. Fuchs and Becker, 2021, 2019; Gueydan et al., 2014).

4.4.3 Limitations

The major contribution of this work is incorporating a composite rheology which depends on multiple parameters, e.g., temperature, lithostatic pressure and strain rate, for the dual inward dipping subduction models. However, previous research indicates that viscosity can also be affected by hydrous fluids, partial melting, and grain size of minerals in subduction zones (Bercovici et al., 2015; Braun et al., 1999; England and Katz, 2010; Montési and Hirth, 2003). In particular, grain size reduction is likely to take place when strain builds up and it may make diffusion creep become the dominant deformation mechanism, overtaking dislocation creep, in the mantle lithosphere (Gueydan et al., 2014; Ruh et al., 2022). Taking these parameters into consideration is likely to strengthen the feedback weakening process within the overriding plate during dual inward dipping subduction.

Subduction can generate convective mantle flow that includes both poloidal and toroidal components. The 2D models tested here neglect the effects of toroidal flow and the third dimension. This could amplify the magnitude of poloidal flow and its weakening effect applied within the overriding plate. Considering that poloidal component dominates over toroidal component during non-steady state subduction (Funiciello et al., 2004), and it is the poloidal cell that provides the relevant traction driving the deformation within the overriding plate (Király et al., 2017; Schellart and

Moresi, 2013), the lack of toroidal flow would only have limited impact on the progressive weakening presented.

In this research, to obtain the designed wide range of plate thicknesses (67 km to 141 km), the half-space cooling model is used instead of the plate model. Plate thickness in plate model flattens when the plate age is greater than ~80 Ma, thus it is not ideal for investigating the effect of thick plates investigated here. It is noted that there is still great uncertainty in terms of how oceanic lithosphere thickness evolves with ocean floor's age. Half-space cooling model was initially proposed to explain the age dependency of bathymetry and heat flow observed. However, this model does not fit these observations as well when the age of the oceanic plate is over 80 Ma. The plate model fits the flattening bathymetry and heat flow in older oceanic plates, but at the cost of applying an artificial temperature boundary condition at the bottom of lithosphere (Parsons and Sclater, 1977; Stein and Stein, 1992). Some question the existence of flattening seafloor bathymetry with age. There is research that indicates that excluding "anomalous oceanic crust", such as sea mountains and hotspots, from the bathymetry dataset can reduce the flattening behaviour and make a half-space cooling model fit well with plates over 80 Ma (Korenaga et al., 2021; Korenaga and Korenaga, 2008). Another hypothesis suggests that half-space cooling model fits well with bathymetry along mantle flow lines instead of age trajectories in the Pacific (Adam and Vidal, 2010). The uncertainty regarding how oceanic lithosphere thickness evolves with ocean floor age, and the 2D nature of the models, requires the results of this study to be interpreted carefully before applying to Earth.

Modern plate tectonic framework only provides limited examples of dual inward dipping subduction system (see examples listed in section 4.1). Even though it is becoming more evident that dual inward dipping subduction also exists throughout the plate tectonic history, the poor constraints on the state of paleo subduction zone

system, e.g., the thickness of the subducting and overriding plate, the distance between the trenches etc., makes an accurate and precise comparison with real-world or extinct dual inward dipping subduction zone very tricky. This research is designed as generic modelling rather than specific modelling. That is to say, the research does not try to match the results with any specific dual inward dipping subduction zone. Instead, it is designed to test the weakening potential dual inward dipping subduction can induce in the overriding plate under different model configuration.

Bearing all the limits in mind, this research cautiously compare the model predictions with observations in the North China Craton (NCC). The NCC provides a natural extinct dual inward dipping subduction case where the trenches are not parallel with each other, i.e., the length of the overriding plate changes laterally. The NCC is a good real-world example to compare with 'L_{OP}^0' models series, since the non-parallel trenches makes it possible to compare the role of varying length of the overriding plate in a single dual inward dipping subduction framework. Based on suture zone studies, the NCC may have experienced dual inward dipping subduction (Santosh, 2010; Windley et al., 2010). The Paleo-Asian Ocean subducts from the north of the craton, while to the southeast lies the subducting Pacific Plate. Surface wave tomography implies that the thickness of the overriding plate (H_{OP}^0), i.e., the NCC, decreases from ~150 km in the western block to ~70 km in the eastern block (Huang et al., 2009). The distance between the trenches of two subducting plates (L_{OP}^0) narrows beneath the eastern block. According to this work, it might suggest that the eastern block would suffer more weakening. This is consistent with the observation that rifting extension and magmatism intrusion, equivalent to weakening level 'IV', only develops in the eastern block, e.g., Bohai Bay Basin. So for now it is only speculated that a dual subduction driven weakening process might have played a role in modifying the rheology and resulting in a variety of deformation patterns within the eastern block of

the NCC, though to fully understand this would require further investigation utilising more advanced models, beyond the limits of this work.

4.4.4 Synoptic summary

The thermo-mechanical modelling here provides a generic understanding of the progressive weakening developed within a varying rheology overriding plate during dual inward dipping subduction. To summarize, dual inward dipping subduction holds a stronger tendency to weaken the overriding plate compared with single sided subduction. This is achieved by creating a fixed trailing boundary condition for the overriding plate and generating a stronger poloidal return flow underlying the overriding plate (Figure 4.16). The stronger poloidal mantle flow is exhibited as a higher horizontal velocity gradient and higher maximum magnitude of upwelling component underlying the overriding plate. It can also initiate a higher degree of viscosity reduction, strain localisation and lithosphere thinning or even spreading extension within the overriding plate. Besides, a dual inward dipping subduction system with thinner and shorter overriding plate, and thicker subducting plate is likely to induce a higher degree of viscosity reduction within the overriding plate (Figure 4.16, b-d).
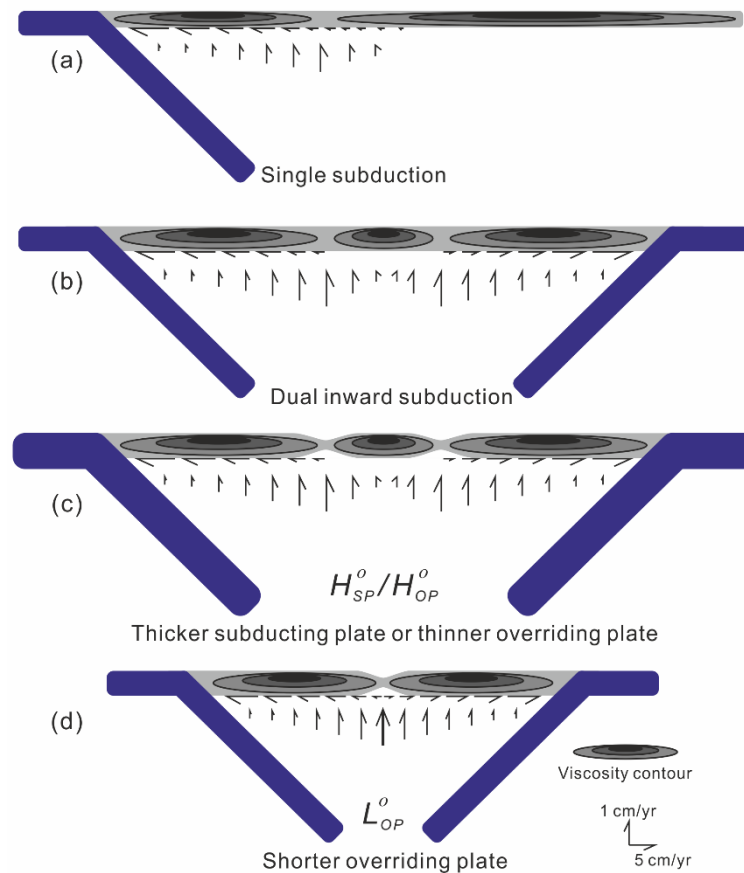
Figure 4.16 Synoptic comparison of different model setup's role in affecting the necking behaviour developed within the overriding plate. (a) Single sided subduction. (b) Dual inward dipping subduction. (c) Thickness of the subducting plate or overriding plate (H_{SP}^0, H_{OP}^0). (d) Length of the overriding plate (L_{OP}^0).

4.5 Conclusion

These 2-D thermo-mechanical numerical models demonstrate that dual inward dipping subduction can generate progressive weakening by lowering viscosity within the overriding plate on a ~10 Myr time scale. Three variables are investigated to understand what controls the maximum degree of weakening. It shows that the initial length (L_{OP}^0) and thickness (H_{OP}^0) of the overriding plate are negatively correlated with the maximum degree of weakening. While the initial thickness of the subducting plate (H_{SP}^0) positively relates to the maximum weakening level. The progressive weakening

can result in a variety of irreversible stretching states ranging from 1) little or no lithosphere thinning and extension, to 2) limited thermal lithosphere thinning, and 3) localised rifting followed by spreading extension.

Comparing with single-sided subduction, dual inward dipping subduction can reduce the magnitude of viscosity to a lower level within the overriding plate. Two aspects are analysed. On the one hand, a dual inward dipping subduction set-up effectively creates a dynamic fixed boundary condition for the middle (overriding) plate. This inhibits the mobility of the plate and helps promote localised strain to accommodate the slab rollback tendency on both sides. On the other hand, when the initial length of the overriding plate is short enough ($L_{OP}^0 \leq 800\ km$), dual inward dipping subduction can form a united upwelling mantle flow which interacts with the bottom of overriding plate and generates a stronger viscosity perturbation within it than single sided subduction models. As a result, dual inward dipping subduction can induce higher degrees of extension in the overriding plate compared with single sided subduction.

Yielding and dislocation creep are the dominant deformation mechanisms that initiates rifting and spreading extension. The progressive weakening is mainly driven by the ever-increasing strain rate, which is also a precondition for initiating thermal weakening, strain localisation, lithosphere thinning and formation of new plate boundaries.

Chapter 5 The role of heterogeneity within the overriding plate in affecting the location of extension during subduction

5.1   Introduction

It is widely observed that subduction can pose a variety of intrusive and extensional tectonic overprint upon the overriding plate by generating volcanic arcs (Mibe et al., 2011; Perfit et al., 1980; Straub et al., 2020), back-arc basins (Jolivet et al., 1994; Ruellan et al., 2003; Sdrolias and Müller, 2006; Uyeda, 1981), or even continental breakup (Dal Zilio et al., 2018; East et al., 2020; Ren et al., 2020; Zhang et al., 2018). Various characteristics of the oceanic subducting plate, e.g., its age, slab dip, crust thickness, dehydration process, rigidity, geochemical heterogeneity, fabric orientation, velocity, gravity anomaly, sediment thickness, and the number of slabs are commonly cited as important properties governing the slab geometry, mantle wedge flow patterns, slab stress state, deformation patterns, dynamics, mantle wedge melting degree, and hazard potential in subduction zones (Bassett and Watts, 2015; Becker and Faccenna, 2009; Billen and Hirth, 2007; Cross et al., 1982; Heuret and Lallemand, 2005; Király et al., 2018; Kusky, 2022; Lallemand et al., 2005; Leat et al., 2000; Schellart, 2007; Timm et al., 2013). Yet, the role of the overriding plate's properties, especially the structure of the heterogeneity within it, has not been rigorously tested. Here, the overriding plate is configured as a combination of both oceanic plate and a continental block. Its role in deciding the localisation of strain deformation, which ends up as the centre of extension, is tested.

Observations suggest that the structure of the overriding plate plays an important role in affecting the subduction zone's geometry and deformation patterns. For example

there is a close spatial relationship between plutonic intrusions and great seismicity events in the Nankai subduction zone (Arnulf et al., 2022). It is also observed that a volcanic arc, back-arc basin and extension centre can develop at different distances away from the trench ranging from ~170 km to ~850 km (Schliffke et al., 2022).

The inclusion of an overriding plate can significantly lower the trench retreat rate (Butterworth et al., 2012; Capitanio et al., 2010). The thickness of the overriding plate can affect trench mobility and subducting plate curvature (Hertgen et al., 2020; Holt et al., 2015b). Increasing the viscosity of the overriding plate ends up with faster trench-ward motion of the overriding plate and more deformation in the subducting plate (Butterworth et al., 2012). However, these previous investigations are all configured with a constant thickness overriding plate perpendicularly away from the trench. In the real world, subduction can take place underneath oceanic plates, continental plates or a combination of both plates. Thus, the thickness of the overriding plate is often heterogenous in the lateral direction perpendicular to the trench.

Some research uses a constant overriding plate thickness, but alters the internal rheology structure, e.g., setting up a weak zone within the overriding plate. The strength of the overriding plate can affect the formation of back-arc extension (Erdős et al., 2021). Weak orogenic lithosphere suturing two continents can be reactivated and guide the strain localisation during supercontinent break-up events (Dang et al., 2020). The presence of a low-viscosity mid-lithosphere discontinuity within the cratonic lithosphere may destabilize the plate during subduction (Shi et al., 2020).

In this research, a series of 2-D thermo-mechanical and self-consistently driven models are conducted to investigate what role adding heterogeneity to the overriding plate plays in altering the deformation patterns and location of extension centres within

the overriding plate. The underlying driving mechanism is also analysed and discussed.

5.2 Methods

5.2.1 Model setup

Similar with the subduction models in the previous two chapters, the computational domain is 10,000 km by 2,900 km, with x (width) coordinates and z (depth) coordinates extending from the surface to the bottom of the lower mantle (Figure 5.1). Such a wide domain reduces the influence of side and bottom boundary conditions (Chertova et al., 2012). The thermal boundary conditions at the surface and bottom are defined by two isothermal values: $T = T_s$ and $T = T_m$ for surface and base of lower mantle respectively, while the sidewalls are insulating. As for velocity boundary conditions, a free-surface is applied at the top boundary to facilitate trench mobility, while the other boundaries are free-slip.
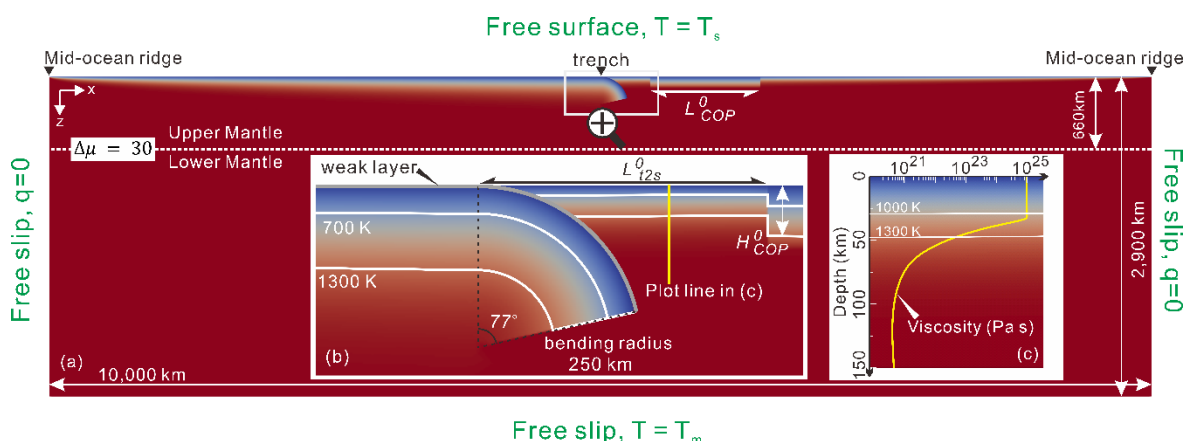
Figure 5.1 Model geometry of single sided subduction with a composite overriding plate illustrated with the initial temperature field as the background. (a) The whole computational domain. The viscosity jump ($\Delta\mu$) between upper and lower mantle at 660 km transition zone is set up with a fixed value of 30. L^0_{COP} is the initial length of the continental block. (b) Enlarged area of trench zone where bending slab meets the heterogenous overriding plate consisting of both oceanic and continental plates. 700 K and 1300 K isotherms are marked in white contours. L^0_{t2s} is the initial lateral distance from the thermal step to the trench. H^0_{COP} is the initial thickness of the continental block. (c) Vertical profile of viscosity against depth within the oceanic overriding plate. The profile (yellow line in (b)) is 300 km away from the initial trench location.

Continental plates have rock records that date back to ~4.5 Ga, which is much older than the oldest oceanic crust ~200 Ma. For the old cratons, this may result from continent's lighter density and higher viscosity which correlates with their highly depleted mantle lithosphere. Younger continental lithosphere can be more deformable and it is this type of lithosphere I consider in this chapter, where the continental block is configured with initial thickness (H^0_{COP}) and length (L^0_{COP}) replacing part of the homogeneous oceanic overriding plate at a certain distance away from the trench (L^0_{t2s}), see Figure 5.1. Within the continental block, the initial thermal structure is homogeneous in the lateral direction, and the vertical thermal profile is defined linearly by

$$T(z) = T_s + (T_m - T_s) * z/H^0_{COP}, \qquad (5.1)$$

where H_{COP}^0 is the initial thickness of the continental block (Turcotte and Schubert,

2014). The continent is usually much older than the oceanic plate, which means the

continent has experienced a long history of cooling. As a result, the continent tends to

form a constant thermal gradient (Turcotte and Schubert, 2014). The constant linear

correlation between temperature and depth applied here is flatter in the crustal depth

compared with the value observed in the real world. This will make the simulated

thicker thermal lithosphere a bit denser than actual continental plates (Equation 2.6),

as crustal and mantle lithosphere compositional difference is not considered in the

thermo-mechanical models. The limited difference is likely to modulate the velocity of

subduction, but it will not pose a significant impact upon the deformation in the

overriding plate, as yielding, a temperature independent deformation mechanism,

dominates the shallow depth of plates (Figure 4.14). Besides, the internal heating

effect is not included for all the plates since the simulation is run for only 10 Myr, which

is too short for internal heating to make a difference (Turcotte and Schubert, 2014).

Laterally along the surface, the age of the subducting plate and overriding oceanic

plate increases linearly with its distance away from the mid-ocean ridge on either side.

While vertically, the age of the plate at the surface defines the initial thermal structure

through a half-space cooling model (Turcotte and Schubert, 2014),

$$T(x, z) = T_s + (T_m - T_s)erf\left(\frac{z}{2\sqrt{\kappa Age^0(x)}}\right), \tag{5.2}$$

where x is the distance away from the mid-ocean ridge, *erf* is the error function, z the

depth, κ the thermal diffusivity. All these parameters are the same as in Chapter 3 and

Chapter 4, and they are listed in the second Chapter (Table 2.1).

The thermal lithosphere is defined as the material colder than 1300 K. So the initial thickness of the subducting plate (H_{SP}^0) and overriding plate (H_{OOP}^0) can be calculated through

$$H_{Plate}^0 = erfinv((T_{1300K} - T_s)/(T_m - T_s)) * 2 * \sqrt{\kappa * Age_{Plate}^0(x)}, \qquad (5.3)$$

where H_{Plate}^0 is the initial thickness of the plate thermal lithosphere and *erfinv* is the inverse error function. The density and viscosity are temperature dependent and they are determined with Equation (2.6) and Equation (2.7) separately.

The free surface boundary condition together with the mid-ocean ridge setup allows the subducting slab, overriding plate and trench to move freely as subduction evolves. To allow for a self-driven subduction without implementing external forces, the subducting plate is set up with a bend into the mantle and a 5 km thick low-viscosity decoupling layer on top. The initial bending radius is 250 km and the slab bends over 77 degrees from the trench (Figure 5.1).

As indicated in Chapter 2, the whole model domain shares the identical composite rheology law incorporating four deformation mechanisms. During each simulation, the viscosity governed by each deformation mechanism will be calculated and compared throughout the domain. The one that yields the least viscosity is the dominant deformation mechanism. It is worth repeating that I always combine the individual viscosities in "parallel" to give the effective viscosity in the simulations (Equation 2.7).

5.2.2 Model variables

The results in Chapter 3 show that the 132 km thick subducting plate (H_{SP}^0) can induce rifting extension within a 50 km thick oceanic overriding plate (H_{OOP}^0). Therefore, the

effect of a similar thickness subducting plate and the role of including a continental lithosphere block of different size and location within such an overriding plate is investigated here. In detail, the continental lithosphere is configured with either different initial distance away from the trench (L_{t2s}^0), or different initial extent (L_{COP}^0) or different initial thickness (H_{COP}^0), see Table 5.1. The subducting plate is tested with a variety of initial thickness (H_{SP}^0) at the trench ranging from 94 km to 132 km. Each series of models only changes one parameter at a time.

Table 5.1 List of model setup.

Model name	L_{t2s}^0 (km)	L_{COP}^0 (km)	H_{COP}^0 (km)	H_{SP}^0 (km)	Age_{SP}^0 (Ma)	H_{OOP}^0 (km)
$L_{t2s}^0 = 250\ km$ [a]	250	1000	100	132	175	50
$L_{t2s}^0 = 450\ km$ [b]	450	1000	100	132	175	50
$L_{t2s}^0 = 650\ km$	650	1000	100	132	175	50
$L_{t2s}^0 = 850\ km$	850	1000	100	132	175	50
$L_{t2s}^0 = 1000\ km$	1000	1000	100	132	175	50
$L_{t2s}^0 = 1250\ km$	1250	1000	100	132	175	50
$L_{COP}^0 = 500\ km$	250	500	100	132	175	50
$L_{COP}^0 = 1000\ km$	250	1000	100	132	175	50
$L_{COP}^0 = 1250\ km$	250	1250	100	132	175	50
$L_{COP}^0 = 1500\ km$	250	1500	100	132	175	50
$H_{COP}^0 = 60\ km$	250	1000	60	132	175	50
$H_{COP}^0 = 70\ km$	250	1000	70	132	175	50
$H_{COP}^0 = 100\ km$	250	1000	100	132	175	50
$H_{COP}^0 = 150\ km$	250	1000	150	132	175	50
$H_{SP}^0 = 132\ km$	450	1000	100	132	175	50
$H_{SP}^0 = 122\ km$	450	1000	100	122	150	50
$H_{SP}^0 = 111\ km$	450	1000	100	111	125	50
$H_{SP}^0 = 100\ km$	450	1000	100	100	100	50

L_{t2s}^0 is the initial distance from the trench to the thermal step. L_{COP}^0 and H_{COP}^0 are the initial length and thickness of the continental lithosphere. H_{SP}^0 and Age_{SP}^0 are the initial thickness and age of the subducting plate at trench. H_{OOP}^0 is the initial thickness of the oceanic overriding plate at the trench. H_{OOP}^0 is 50 km in all models and it is derived from a 25 Ma oceanic plate via Equation (5.3). Models are named with the variable tested, e.g. model '$L_{t2s}^0 = 250\ km$' and model '$L_{t2s}^0 = 450\ km$' correspond to L_{t2s}^0 of 250 km and 450 km separately, while all the other variables remains the same value in these two models.

[a] Reference model for models with varying L_{t2s}^0, L_{COP}^0 and H_{COP}^0.

[b] Reference model for models with varying H_{SP}^0.

5.3   Results

As with non-steady state models in the previous two chapters, all models tested initiate with a non-steady state subduction phase where slab subduction accelerates as a growing amount of slab enters the upper mantle. During the short period of interaction with the lower mantle, the net negative buoyancy within the slab is balanced with additional support from the lower mantle and the model then enters a steady state subduction phase.

5.3.1   Varying L_{t2s}^0

Within the range of L_{t2s}^0 from 250 km to 1250 km tested here, all models yield rifting or spreading extension within the overriding plate, characterised by localised necking of viscosity contour, thinning of the plate's thermal thickness and the development of a new spreading plate boundary (Figure 5.2). However, the position of extension varies.

As L_{t2s}^0 increases from 250 km to 450 km, the rifting or spreading centre jumps laterally from around the right margin of the continent (I will use 'right' to describe the region away from the trench, and 'left' for describing the region close to the trench, as seen in Figure 5.2) to above the mantle wedge corner which is on the left side of the continent (Figure 5.2, a, b). The total amount of lateral migration of the spreading centre can be as much as ~1400 km relative to the centre of the continental block. Notably, the magnitude of the stress field within the continental lithosphere drops dramatically when the spreading centre is on the left of the continental block compared with when it is on the right side of the block. The decreasing magnitude of the stress field indicates that much less stress is transmitted rightward through the continental block to the oceanic plate on the right side.

As L_{t2s}^0 increases from 450 km to 850 km, the spreading centre remains on the left side of the continental lithosphere while the centre migrates mildly rightward, keeping a relatively fixed distance (~200 km) away from the left edge of continental block (Figure 5.2, c, d). The magnitude of stress transmitted across the continental lithosphere is low and there is not much stress variation within the continental block for these models.

When L_{t2s}^0 is over 850 km, the stretching within the overriding plate degrades from spreading extension to rifting extension (Figure 5.2, e); and the stretching centre stops its rightward migration and keeps a relatively fixed distance of ~750 km away from the trench. The distance roughly equals that in the single sided subduction models in Chapter 3 (Figure 3.4), though the viscosity reduction on the right flank of the spreading centre is greater here. The nearly fixed location of rifting extension indicates that the continental lithosphere fails to affect the localisation of the stretching behaviour when the continent is too far away from the trench.
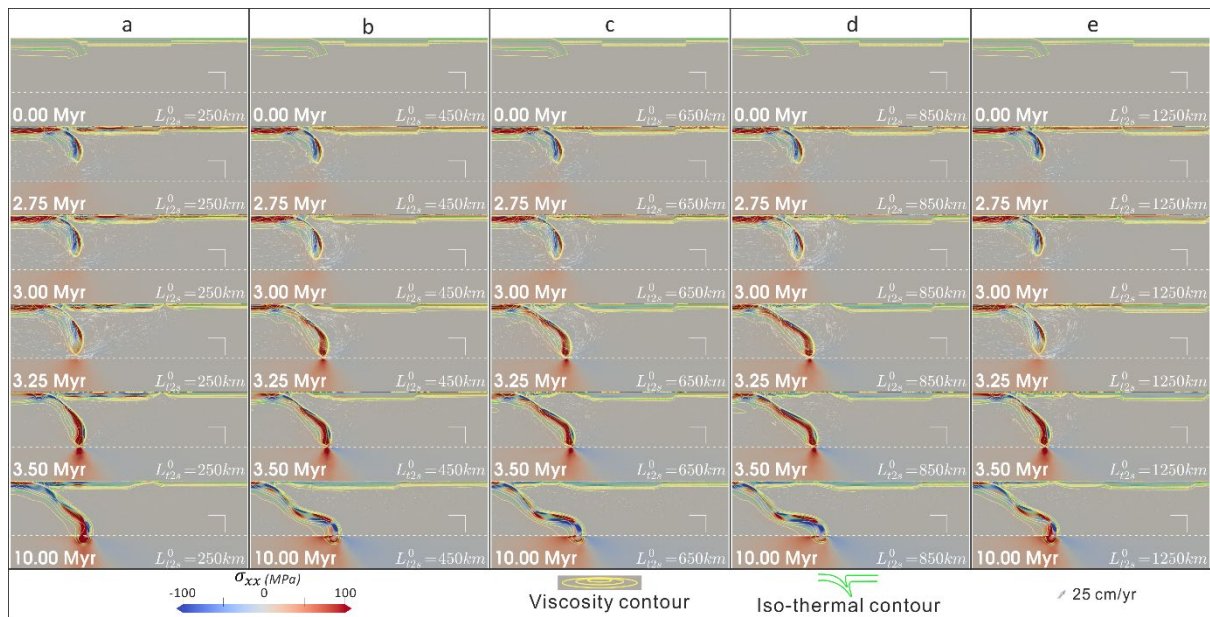
Figure 5.2 Simulation snapshots of models with varying L_{t2s}^0. (a) Model '$L_{t2s}^0 = 250\ km$'. (b) Model '$L_{t2s}^0 = 450\ km$'. (c) Model '$L_{t2s}^0 = 650\ km$'. (d) Model '$L_{t2s}^0 = 850\ km$'. (e) Model '$L_{t2s}^0 = 1250\ km$'. The progressive weakening process within the overriding plate is demonstrated by the necking of the iso-viscous contours. The 5 groups of yellow contours encompassing the plates in each screenshot are iso-viscous contours of $10^{20}, 10^{21}, 10^{22}, 10^{23}, 10^{24}\ Pa \cdot s$ from outward to inward. The iso-viscous contours at the bottom of the plate are quite close together, and hence can be hard to see individually. The two sets of green solid lines are 700 K and 1300 K isotherm contours to image the geometry of the thermal plate. The transition zone at the depth of 660 km is marked by the horizontal white dashed line. The white right-angle scale bar lying above the right end of the transition zone represents 200 km in both directions. The bottom left corner caption shows the elapsed simulation time and bottom right corner is the name of the model. Remember the view here is just a part of the computational domain.

Figure 5.3 shows the temporal evolution of viscosity along a horizontal slice at the depth of 20 km, from 4000 km to 7500 km away from the left side of the simulation box. In response to the migration of rifting extension from the right side of the continental block to its left side, viscosity necking behaviour on both sides of the continental block evolves as well. It is observed that the necking of the iso-viscous contours fades away gradually on the right side of the continental block as L_{t2s}^0 increases (Figure 5.3, a-f). While, at the same time, the width and the viscosity reduction of the necking area grows in magnitude on the left side of the continental

block. The strain localisation is well observed in the necking area of the iso-viscous contour map. The viscosity reduction initiates over a broad range within the overriding plate. Then the wide range narrows gradually and rifting extension initiates in a narrow zone (<50 km wide) and starts to grow immediately.

In Chapter 4, it was noted that the necking of 10^{21} $Pa \cdot s$ iso-viscous contour can be recognised as the initiation of rifting extension. Thus it is possible to use this contour (see Figure 5.3) to visualize the range and duration of extension developed as the model evolves. The results show that increasing L_{t2s}^0 not only modifies the location of rifting extension, but also produces rifting extension with different width and duration. When rifting extension develops on the right side of the continental block, the extension is highly focused and remains active until the end of the 10 Myr simulation, though the width of extension narrows gradually (Figure 5.3, a). While when rifting extension initiates on the left side of the continental block, the width of the extension is wider but weakens more quickly (Figure 5.3, b-d).
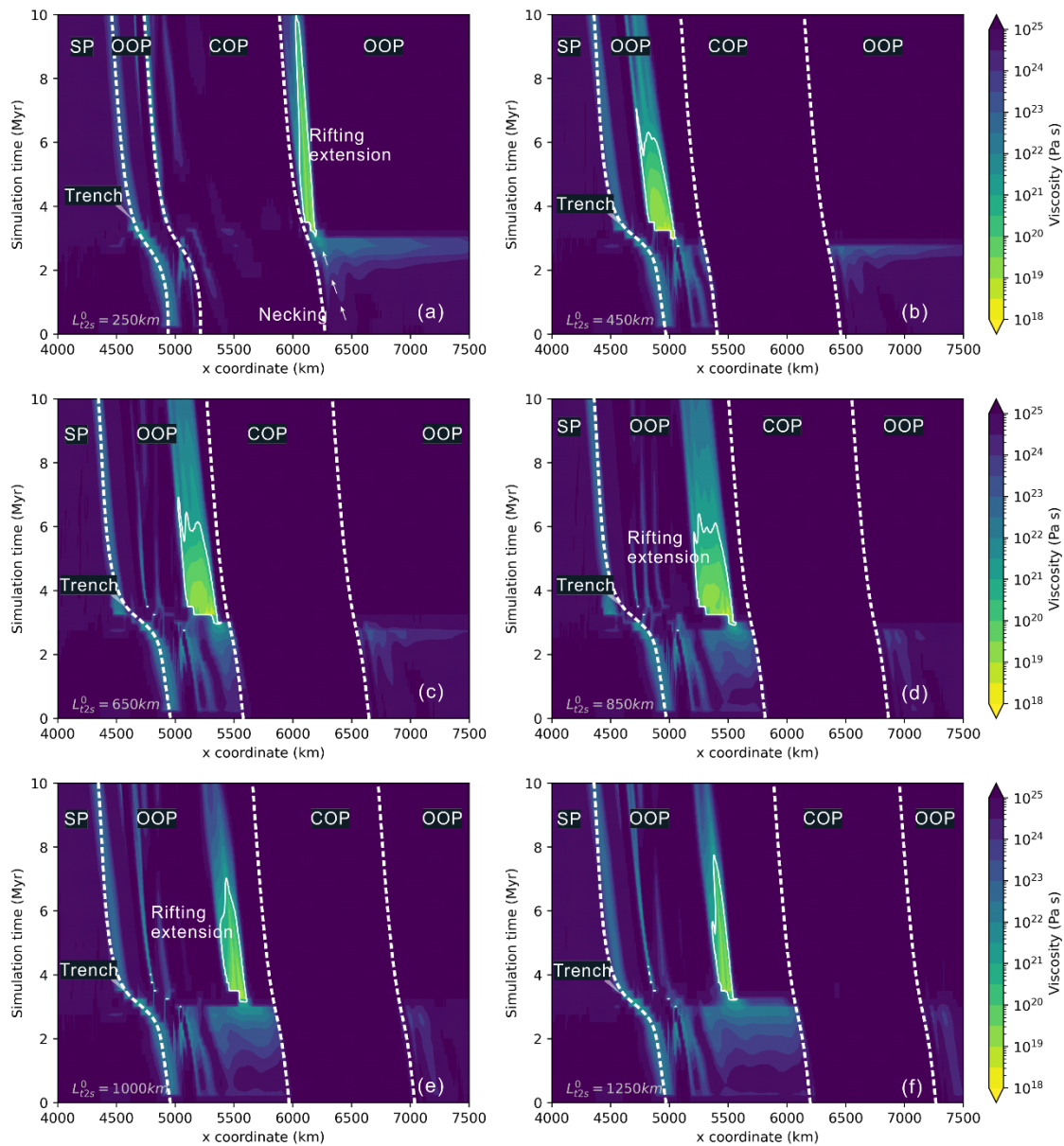
Figure 5.3 Temporal evolution of viscosity along a horizontal line at the depth of 20km. (a) Model '$L_{t2s}^0 = 250\ km$'. (b) Model '$L_{t2s}^0 = 450\ km$'. (c) Model '$L_{t2s}^0 = 650\ km$'. (d) Model '$L_{t2s}^0 = 850\ km$'. (e) Model '$L_{t2s}^0 = 1000\ km$'. (f) Model '$L_{t2s}^0 = 1250\ km$'. Dashed white line in (a) marks the migration trajectory of the trench as model evolves. The solid white iso-viscous contour ($10^{21}\ Pa \cdot s$) shows the temporal and spatial evolution of active rifting extension developed within the overriding plate.

The total trench retreat increases gradually from ~410 km to ~550 km at the end of 10 Myr simulation as L_{t2s}^0 increases from 250 km to 850 km (Figure 5.4). As L_{t2s}^0 goes

beyond 850 km the total trench retreat starts to decrease from ~550 km to ~520 km (model $'L_{t2s}^0 = 1000\ km'$) and to ~490 km (model $'L_{t2s}^0 = 1250\ km'$).

Figure 5.4 Total trench retreat throughout the 10 Myr simulation with varying L_{t2s}^0.

5.3.2 Varying L_{COP}^0

Here, the role of varying the initial length of the continental block (L_{COP}^0) is tested assuming L_{t2s}^0 is 250 km and H_{COP}^0 is 100 km. As L_{COP}^0 increases from 500 km to 1250 km, the extension centre remains on the right side of the continental block, while the total extension of the spreading centre decreases (Figure 5.5, a-c). As L_{COP}^0 increases to 1500 km, the model fails to generate rifting extension on the right side of the continental block (Figure 5.5, d). The magnitude of the stress field within the continental block decreases away from the trench as the length of the overriding plate increases, indicating that there is less stress transmitted through the continental block to its right boundary with the oceanic plate.
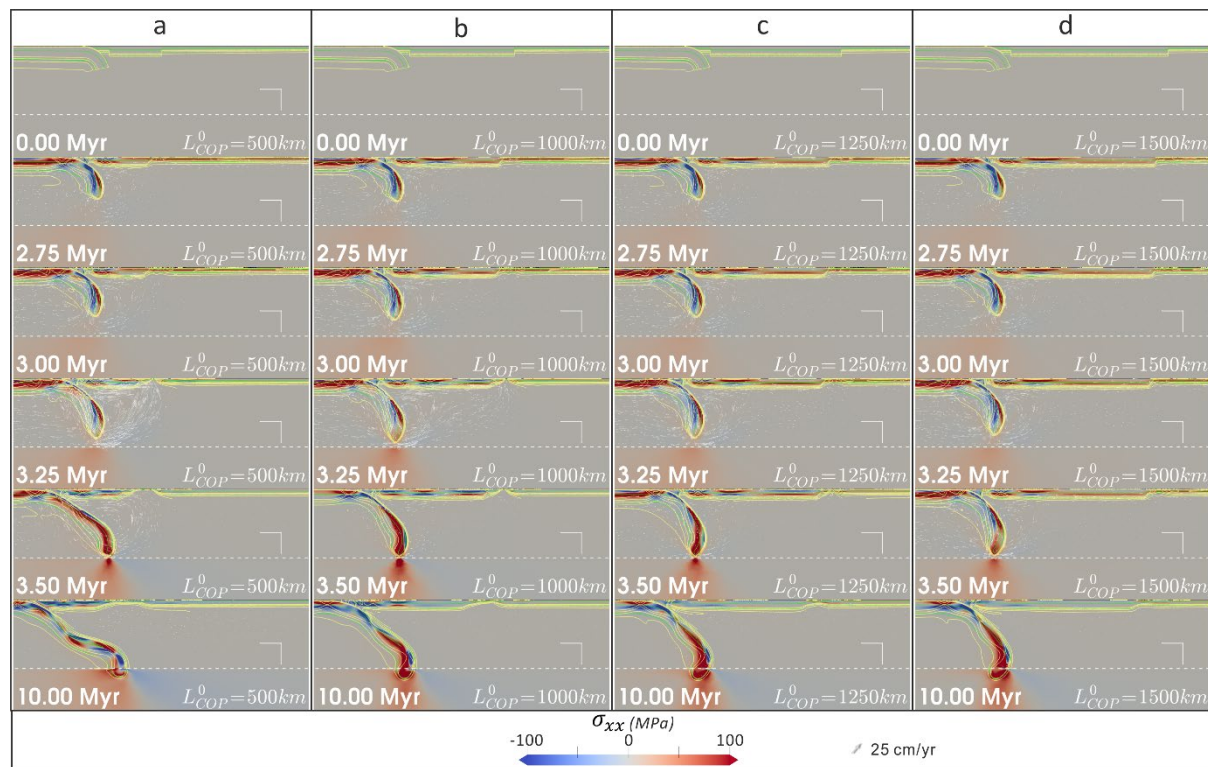
Figure 5.5 Simulation snapshots of models with varying L^0_{COP}. (a) Model '$L^0_{COP} = 500\ km$'. (b) Model '$L^0_{COP} = 1000\ km$'. (c) Model '$L^0_{COP} = 1250\ km$'. (d) Model '$L^0_{COP} = 1500\ km$'. A detailed explanation of the legends can be found in the caption of Figure 5.2.

To reveal more details of the deformation within the overriding plate, a contour map of the second invariant of strain rate and viscosity at the depth of 20 km are presented as a pair for each model (Figure 5.6). The strain rate contour map shows that subduction can induce multiple high strain rate belts even within the continental block (Figure 5.6, a). As L^0_{COP} increases, the number of high strain rate belts decreases and the magnitude of strain rate therein decreases as well (Figure 5.6, b-d). While all models initiate extension on the right side of the continental block, the width and duration of extension varies. The width of extension reduces from ~250 km (Figure 5.6, e) to ~100 km (Figure 5.6, f), ~50 km (Figure 5.6, g) and 0 km (Figure 5.6, h) as L^0_{COP} increases from 500 km to 1500 km. Meanwhile, a wide range of extension duration is observed in the overriding plate, ranging from ~1 to 7 Myr (Figure 5.6, e-g).
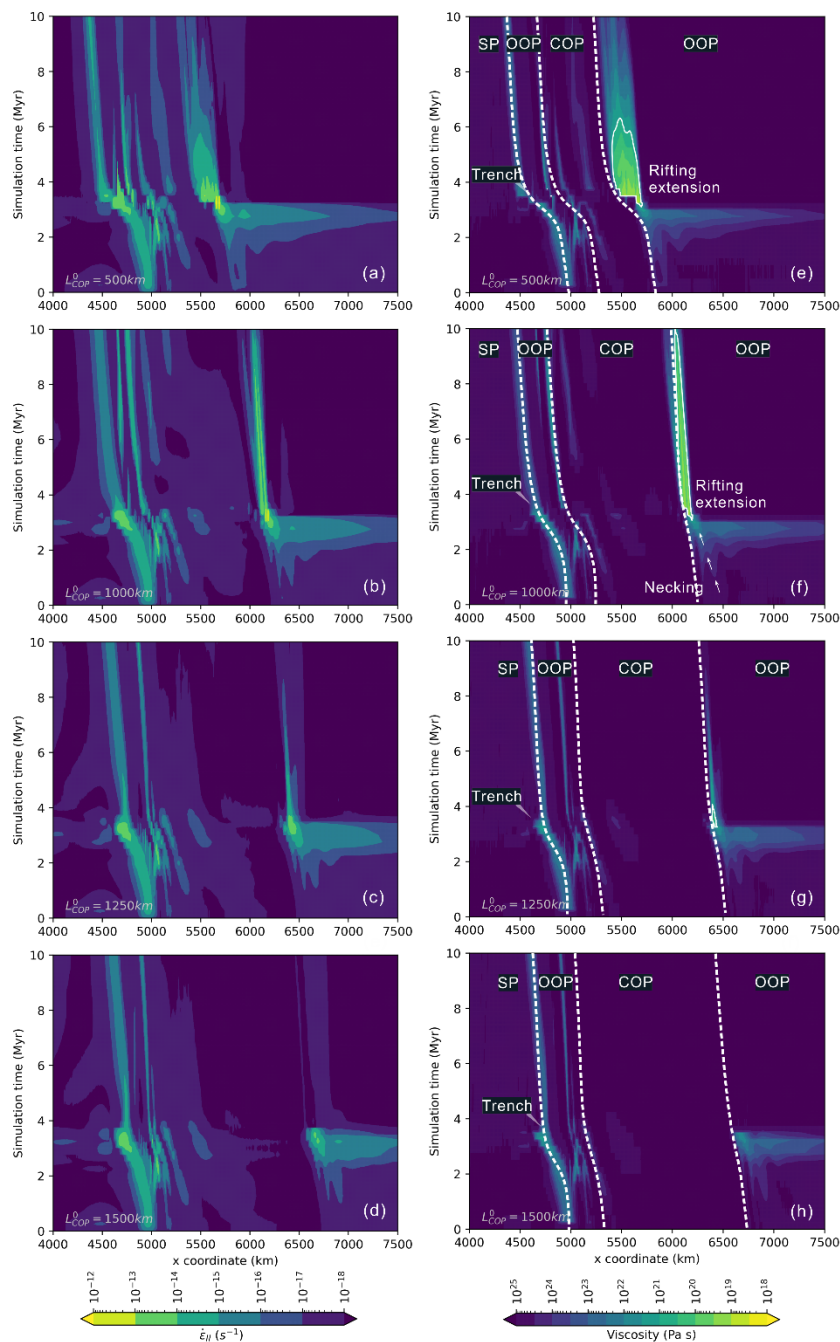
Figure 5.6 Temporal evolution of second invariant of strain rate (a-d) and viscosity (e-h) along a horizontal line at the depth of 20km. (a, e) Model '$L^0_{COP} = 500\ km$'. (b, f) Model '$L^0_{COP} = 1000\ km$'. (c, g) Model '$L^0_{COP} = 1250\ km$'. (d, h) Model '$L^0_{COP} = 1500\ km$'. Dashed white line in (f) marks the migration trajectory of the trench as the model evolves. The solid white iso-viscous contour ($10^{21}\ Pa \cdot s$) shows the temporal and spatial evolution of active rifting extension developed within the overriding plate.

The total trench retreat decreases gradually from ~510 km to ~280 km at the end of 10 Myr simulation as L^0_{COP} increases from 500 km to 1500 km. This group of models

suggests that increasing the initial length of the continental lithosphere (L_{COP}^0) can inhibit the rifting extension behaviour at the margin of the continental lithosphere.
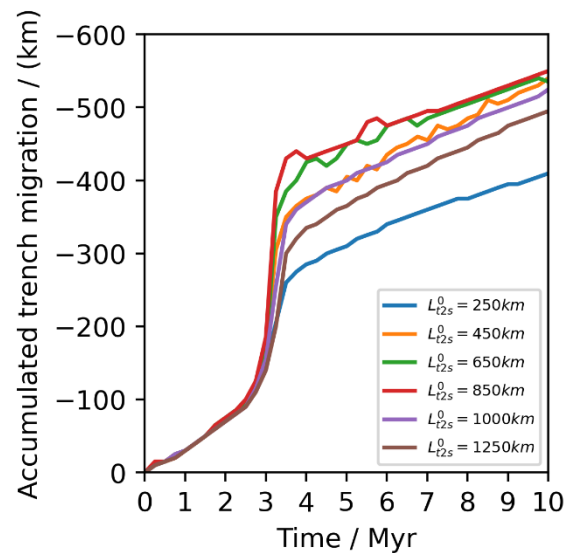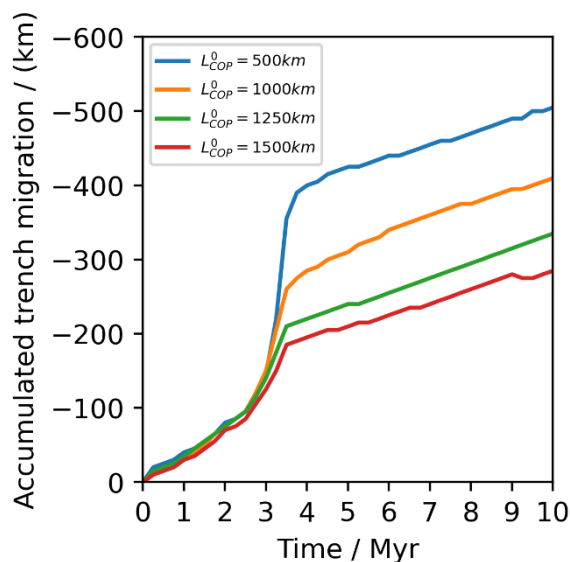

Figure 5.7 Total trench retreat throughout the 10 Myr simulation with varying L_{COP}^0.

5.3.3 Varying H_{COP}^0

Then, the role of varying the initial thickness of the continental block (H_{COP}^0) from 60 km to 150 km is tested assuming L_{t2s}^0 is 250 km and L_{COP}^0 is 1000 km (Figure 5.8). When H_{COP}^0 is 60 km, the spreading extension develops on the left side of the continental block (Figure 5.8, a). As H_{COP}^0 increases to 70 km, rifting extension develops on both sides of the continental block (Figure 5.8, b). When H_{COP}^0 is 100 km, rifting extension only develops on the right side of the continental block (Figure 5.8, c). These results show a rightward migration trend to the extension centre as H_{COP}^0 increases from 60 km to 100 km. The total amount of lateral migration of the extension centre can be as much as ~1200 km relative to the centre of continental block. There is no rifting extension observed in the model where H_{COP}^0 is 150 km thick.

Notably, the stress patterns within the continental lithosphere varies as H_{COP}^0 increases as well. When the continental block is 60 km or 70 km thick, the overall stress state is purely extensional within the continental block. While when H_{COP}^0 is 100 km or thicker, the stress state within the continental block alternates with extensional and compressional stress in both lateral and vertical direction. Meanwhile, the magnitude of alternating stress field decreases as H_{COP}^0 increases (Figure 5.8, c, d), indicating that much less stress is transmitted rightward through the continental block to the oceanic plate on the right side. Besides, there is a significant transition of stress field from overall extension to compression within the continental block as H_{COP}^0 thickens to 150 km.
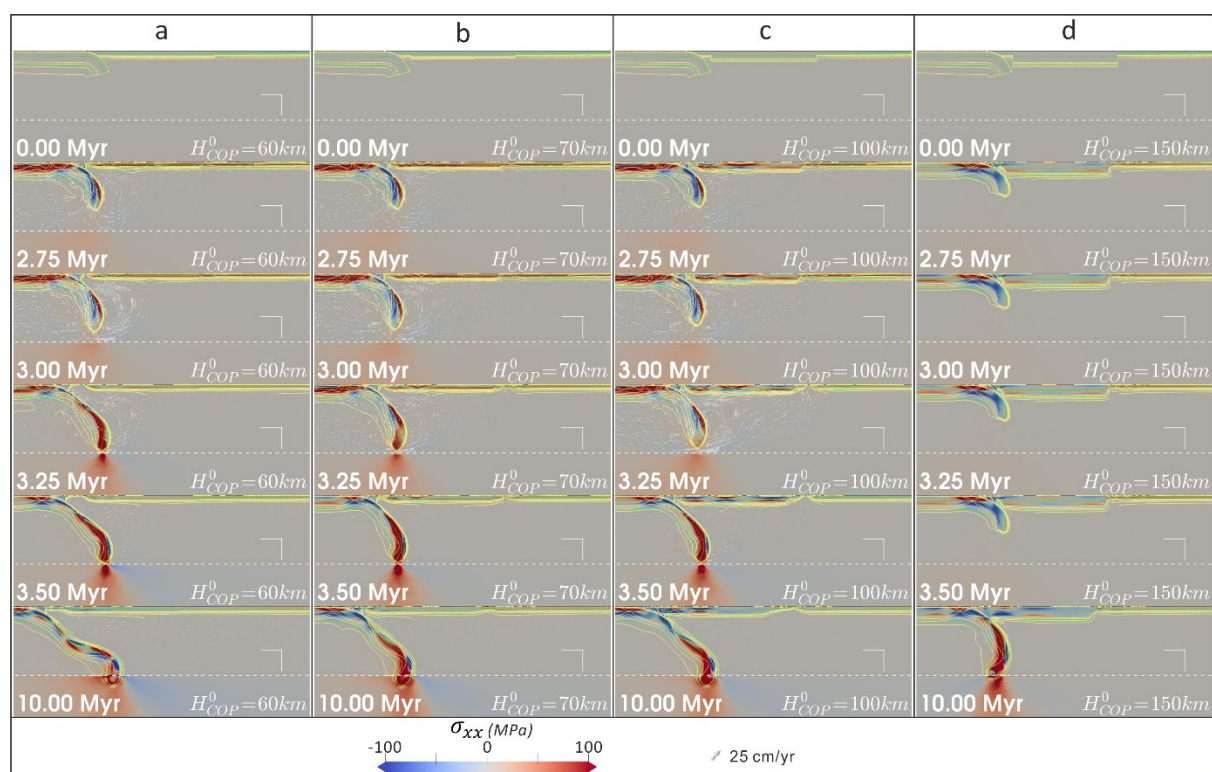
Figure 5.8 Simulation snapshots of horizontal normal stress of models with varying H_{COP}^0. (a) Model '$H_{COP}^0 = 60\ km$'. (b) Model '$H_{COP}^0 = 70\ km$'. (c) Model '$H_{COP}^0 = 100\ km$'. (d) Model '$H_{COP}^0 = 150\ km$'. A detailed explanation of the legends can be found in the caption of Figure 5.2.

The contour map in Figure 5.9 shows that as the rifting centre migrates from the left side of the continental block to its right side, the magnitude of strain rate and viscosity reduction increases on one side of the continental block as it decreases on the other side. The width and duration of extension varies as H^0_{COP} increases. The width of extension is ~150 km and stays active for ~3 Myr when H^0_{COP} is 60 km (Figure 5.9, e). It is noted that two minor extension centres, each with width of less than ~50 km, develop on both sides of the continental block and last for less than ~0.5 Myr when H^0_{COP} increases to 70 km (Figure 5.9, f). When H^0_{COP} increases to 100 km, the extension centre finishes rightward migration, and it only develops and stays active for ~7 Myr on the right side of the continental block (Figure 5.9, g). H^0_{COP} as thick as 150 km can significantly slow down the sinking of the subducting slab and inhibit the viscosity reduction within the whole overriding plate (Figure 5.9, h).

Figure 5.9 Temporal evolution of viscosity along a horizontal line at the depth of 20km. (a, e) Model '$H^0_{COP} = 60\ km$'. (b, f) Model '$H^0_{COP} = 70\ km$'. (c, g) Model '$H^0_{COP} = 100\ km$'. (d, h) Model '$H^0_{COP} = 150\ km$'. Dashed white line in (g) marks the migration trajectory of the trench as the model evolves. The solid white iso-viscous contour ($10^{21}\ Pa \cdot s$) shows the temporal and spatial evolution of active rifting extension developed within the overriding plate.

The total trench retreat decreases gradually from ~500 km to ~150 km at the end of 10 Myr simulation as L^0_{COP} increases from 60 km to 150 km. This group of models

suggests that increasing the initial thickness of the continental lithosphere (H_{COP}^0) can inhibit the rifting extension behaviour at the margin of the continental lithosphere.
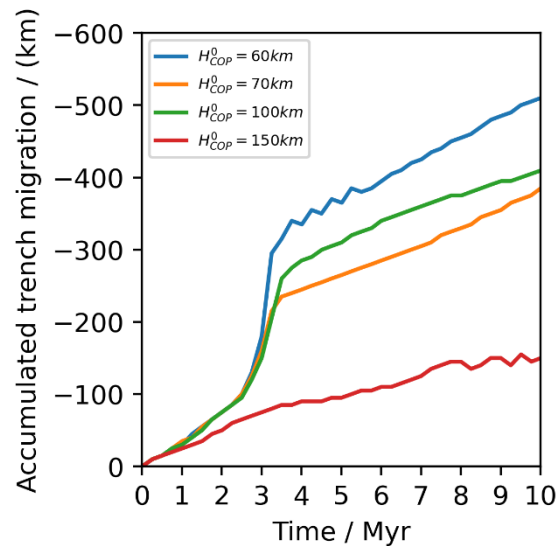
Figure 5.10 Total trench retreat throughout the 10 Myr simulation with varying H_{COP}^0.

5.3.4 Varying H_{SP}^0

Lastly, the role of varying the initial thickness of the subducting plate at the trench (H_{SP}^0) from 100 km to 132 km is tested assuming L_{t2s}^0 is 450 km, H_{COP}^0 is 100 km, and L_{COP}^0 is 1000 km (Figure 5.11). When H_{SP}^0 is 100 km, there is no rifting extension developing within the overriding plate (Figure 5.11, a). As H_{SP}^0 increases to 111 km or thicker values, the slab sinks faster and generates stronger mantle wedge flow at each timestep (Figure 5.11, b-d). Meanwhile, a growing extent of extension starts to develop on the left side of the continental block. To be noted, the distance from trench to the extension centre is fixed at ~200 km away from the trench for all models (Figure 5.11, b-d), suggesting that H_{SP}^0 does not regulate the position of the extension centre.
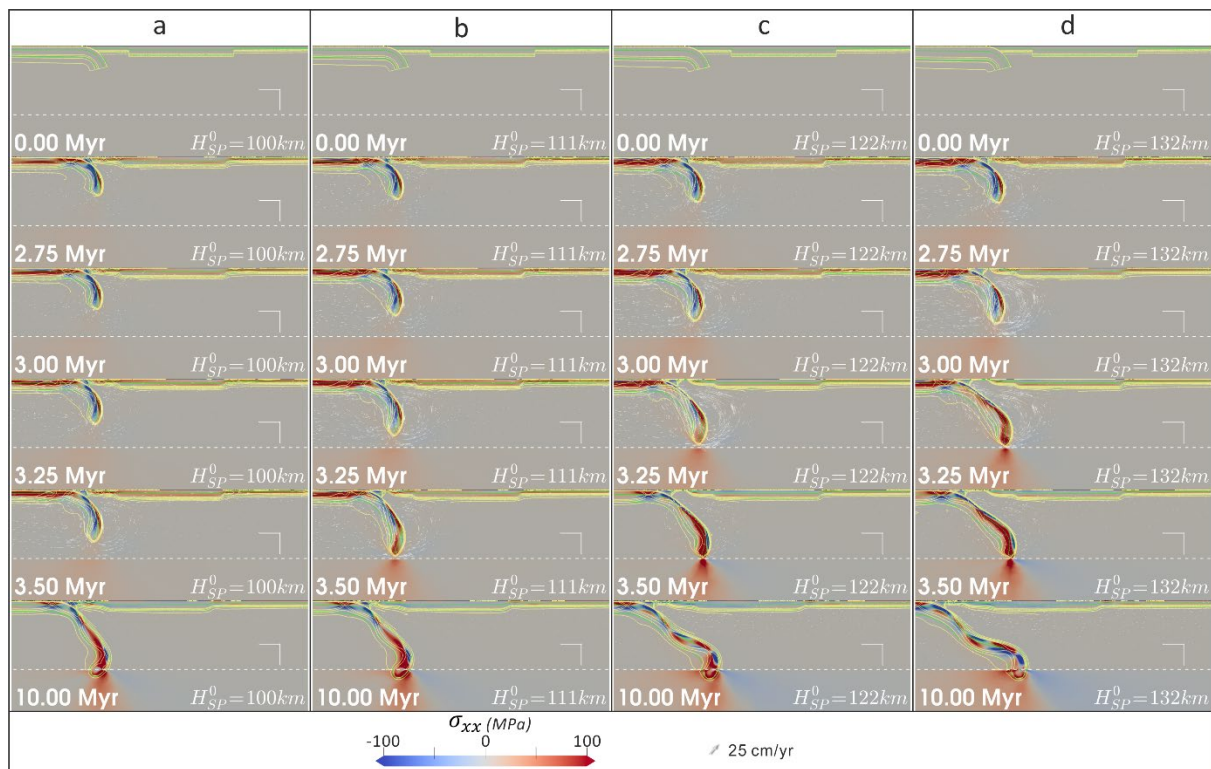
Figure 5.11 Simulation snapshots of models with varying H_{SP}^0. (a) Model '$H_{SP}^0 = 100\ km$'. (b) Model '$H_{SP}^0 = 111\ km$'. (c) Model '$H_{SP}^0 = 122\ km$'. (d) Model '$H_{SP}^0 = 132\ km$'. A detailed explanation of the legends can be found in the caption of Figure 5.2.

A growing magnitude of strain rate and viscosity reduction is observed throughout the overriding plate as H_{SP}^0 increases (Figure 5.12). Though there is also viscosity reduction developing on the right side of the continental block during subduction, it is not as significant as that on the left side of the continental block. Besides, the width of the active extension increases from ~50 km (Figure 5.12, f), to 130 km (Figure 5.12, g) and 200 km (Figure 5.12, h). The duration of active extension increases from 2 Myr (Figure 5.12, f) to 3 Myr (Figure 5.12, g-h).
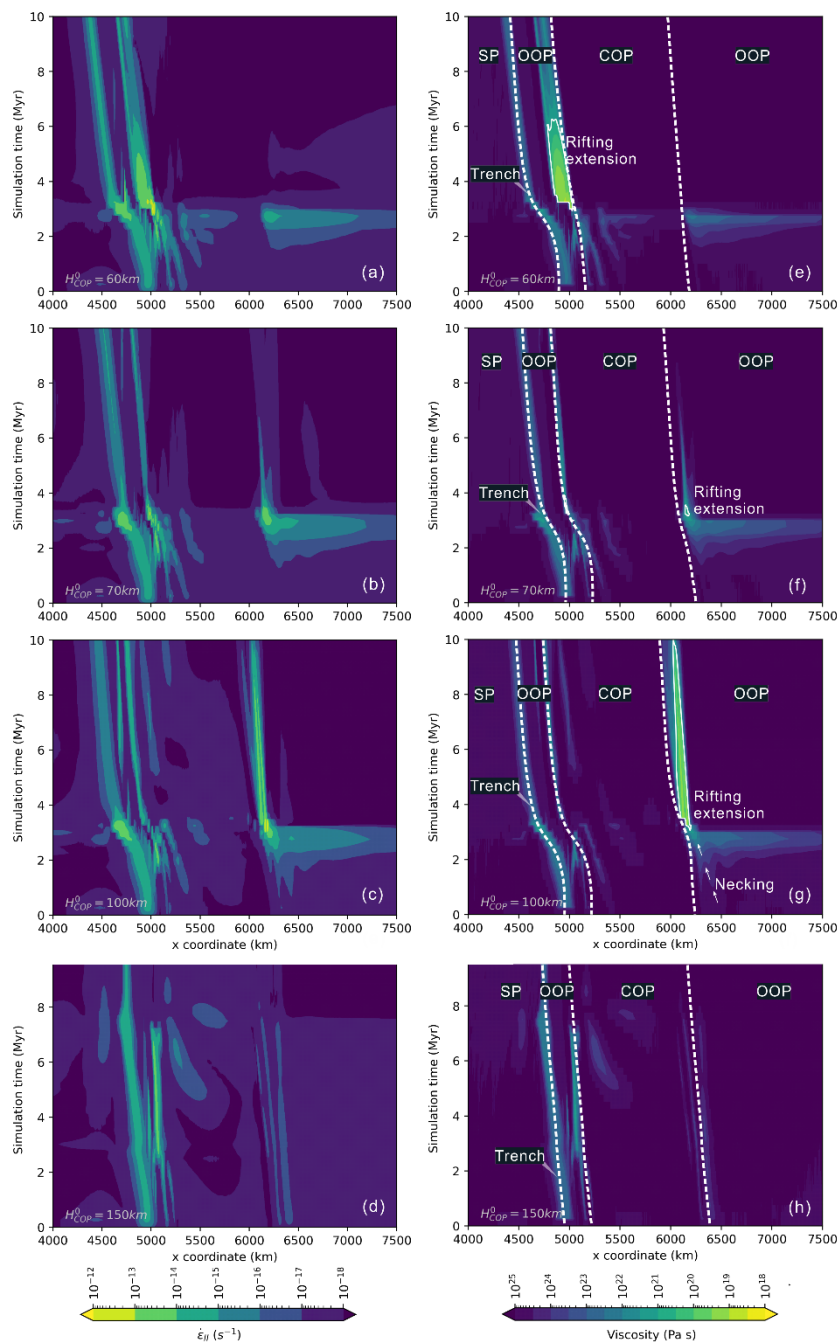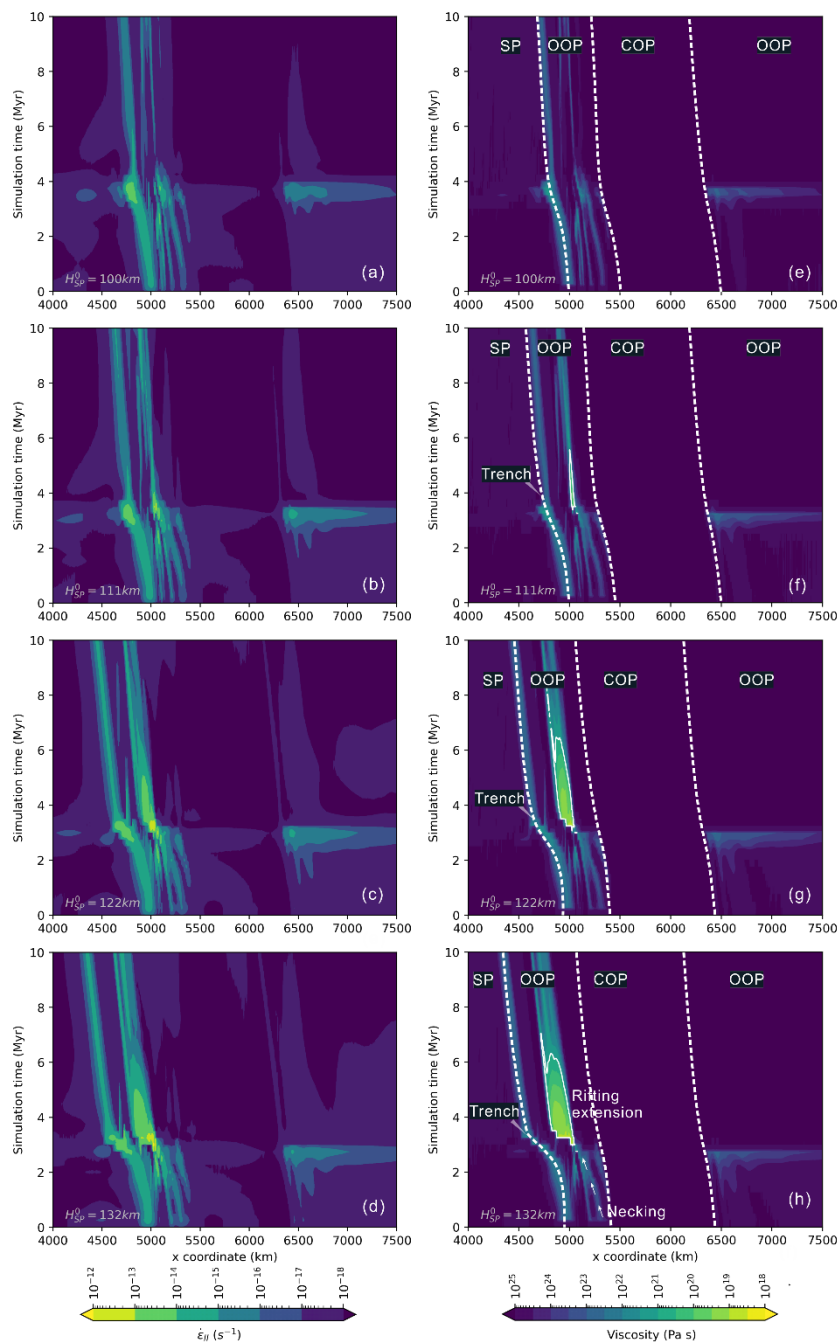
Figure 5.12 Temporal evolution of viscosity along a horizontal line at the depth of 20km. (a, e) Model '$H_{SP}^0 = 100\ km$'. (b, f) Model '$H_{SP}^0 = 111\ km$'. (c, g) Model '$H_{SP}^0 = 122\ km$'. (d, h) Model '$H_{SP}^0 = 132\ km$'. Dashed white line marks the migration trajectory as model evolves. The solid white iso-viscous contour ($10^{21}\ Pa \cdot s$) shows the temporal and special evolution of active rifting extension developed within the overriding plate.

The total trench retreat increases gradually from ~200 km to ~550 km at the end of 10 Myr simulation as H_{SP}^0 increases from 100 km to 132 km. This group of models

suggests that increasing the initial thickness of the subducting plate at the trench (H_{SP}^0) can strengthen the rifting extension behaviour on the left side of the continental lithosphere.
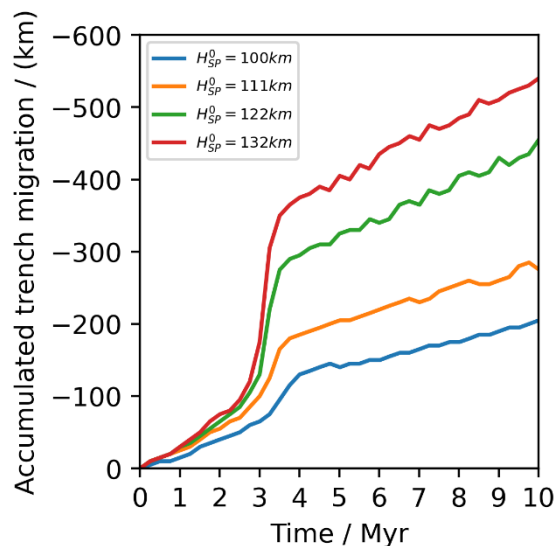
Figure 5.13 Total trench retreat throughout the 10 Myr simulation with varying H_{SP}^0.

5.3.5   Regime diagram

A variety of deformation patterns and stretching state within the overriding plate have been observed when varying L_{t2s}^0, L_{COP}^0, H_{COP}^0 and H_{SP}^0. Several diagnostics are evaluated to quantify the deformation developed within the overriding plate during the 10 Myr simulation. The detail of each diagnostic is described as follows.

t_{rift} indicates the time it takes to develop rifting extension within the overriding plate. There are some fluctuations of t_{rift} for models that develop rifting extension ranging from 3 Myr to 3.5 Myr (Table 5.2). All these models develop rifting or spreading extension during the non-steady state subduction, i.e., before the slab interacts with the lower mantle.

t_{660} equals how much time the subducting plate takes to sink to the depth of 660km. The models here yield a wide range of t_{660} ranging from 3.25 Myr to 7.5 Myr. The results show that t_{660} is independent of L_{t2s}^0 from 250 km to 1250 km (Table 5.2). While increasing L_{COP}^0 and H_{COP}^0, or decreasing H_{SP}^0 increases t_{660} to a limited extent (model '$H_{COP}^0 = 150\ km$' is an exception).

$\bar{v}_{sink}$ equals 460 km (the vertical distance from the initial slab tip depth to the depth of 660 km) divided by t_{660}. $\bar{v}_{sink}$ ranges from 6 to 14 cm/yr. Notably, models that develop rifting extension usually have a high $\bar{v}_{sink}$ value, but high $\bar{v}_{sink}$ does not necessarily produce rifting extension (e.g., model '$L_{COP}^0 = 1500\ km$' and model '$H_{SP}^0 = 100\ km$').

Extension position (EP) describes the extension centre's position relative to the continental block during subduction, and the result is either left side (close to the trench) or right side (away from the trench) or both sides. The results show that only varying L_{t2s}^0 and H_{COP}^0 in a certain range can effectively make the extension centre migrate from one side of the continental block to the other side (Table 5.2). The EP migration across the continental block is not observed in models with varying L_{COP}^0 and H_{SP}^0.

l_{EP2t} marks the lateral distance from the centre of the necking area to the trench at the timestep of t_{rift}. The simulations here generate a variety of l_{EP2t} extending from 200 km to 1600 km. The results indicate that l_{EP2t} does not vary in models with L_{t2s}^0 higher than 1000 km or with varying H_{SP}^0. While in the other models the location of the extension centre differs and therefore l_{EP2t} varies.

l_{EP2cc} records the lateral distance from the extension centre to the centre of the continental block at the timestep of t_{rift}. l_{EP2cc} is positive if EP lies right to the continental block, and l_{EP2cc} is negative if EP develops on the left side of the

continental block. The results show that varying L_{t2s}^0, L_{COP}^0 and H_{COP}^0 can effectively affect the value of l_{EP2cc} , while the initial thickness of subducting plate at trench (H_{SP}^0) shows little impact.

l_{EP2cm} is the lateral distance from the extension centre to the nearest margin of the continental block at the timestep of $t_{\rm rift}$. l_{EP2cm} is positive and ranges from 125 km to 160 km if EP is on the right side of the continental block. l_{EP2cm} is negative and ranges from -580 km to -70 km if EP is on the left side of the continental block. The results show that varying L_{t2s}^0, L_{COP}^0 and H_{COP}^0 yields a variety of magnitudes for l_{EP2cc} , while H_{SP}^0 plays little role in affecting l_{EP2cm}. The sensitivity of this diagnostic to the four variables is similar with that of l_{EP2cc}.

Table 5.2 Summary of diagnostics for all models.

Model name	$t_{\rm rift}$ (Myr)	t_{660} (Myr)	$\bar{v}_{sink}$ (cm/yr)	EP	l_{EP2t} (km)	l_{EP2cc} (km)	l_{EP2cm} (km)
$L_{t2s}^0 = 250\ km$ [a]	3.25	3.50	13	Right	1350	650	150
$L_{t2s}^0 = 450\ km$ [b]	3.00	3.50	13	Left	200	-780	-280
$L_{t2s}^0 = 650\ km$	3.25	3.50	13	Left	530	-660	-160
$L_{t2s}^0 = 850\ km$	3.00	3.50	13	Left	700	-690	-190
$L_{t2s}^0 = 1000\ km$	3.25	3.50	13	Left	750	-770	-270
$L_{t2s}^0 = 1250\ km$	3.25	3.50	13	Left	750	-1080	-580
$L_{COP}^0 = 500\ km$	3.25	3.50	13	Right	850	410	160
$L_{COP}^0 = 1000\ km$	3.25	3.50	13	Right	1350	650	150
$L_{COP}^0 = 1250\ km$	3.50	3.50	13	Right	1600	760	135
$L_{COP}^0 = 1500 km$	-	3.50	13	-	-	-	-
$H_{COP}^0 = 60\ km$	3.00	3.25	14	Left	200	-580	-80
$H_{COP}^0 = 70\ km$ [c]	3.25	3.25	14	Left/Right	200/1200	-570/625	-70/125
$H_{COP}^0 = 100\ km$	3.25	3.50	13	Right	1350	650	150
$H_{COP}^0 = 150\ km$	-	7.50	6	-	-	-	-
$H_{SP}^0 = 100\ km$	-	4.00	12	-	-	-	-
$H_{SP}^0 = 111\ km$	3.50	3.75	12	Left	200	-770	-270
$H_{SP}^0 = 122\ km$	3.25	3.50	13	Left	200	-780	-280
$H_{SP}^0 = 132\ km$	3.00	3.25	14	Left	200	-780	-280

[a] Reference model for models with varying L_{t2s}^0, L_{COP}^0 and H_{COP}^0.

[b] Reference model for models with varying H_{SP}^0.

[c] Model '$H_{COP}^0 = 70\ km$' develops rifting extension on both sides of the continental block simultaneously.

By combining all the qualitative and quantitative diagnostics presented in the results, two end members are classified here: 1) EP on the left side (close to the trench) of the continental block (EPL), and 2) EP on the right side (away from the trench) of the continental block (EPR). Three regime diagrams are plotted based on three frames of references listed in Table 5.2, and they are l_{EP2t}, l_{EP2cc}, and l_{EP2cm} (Figure 5.14).
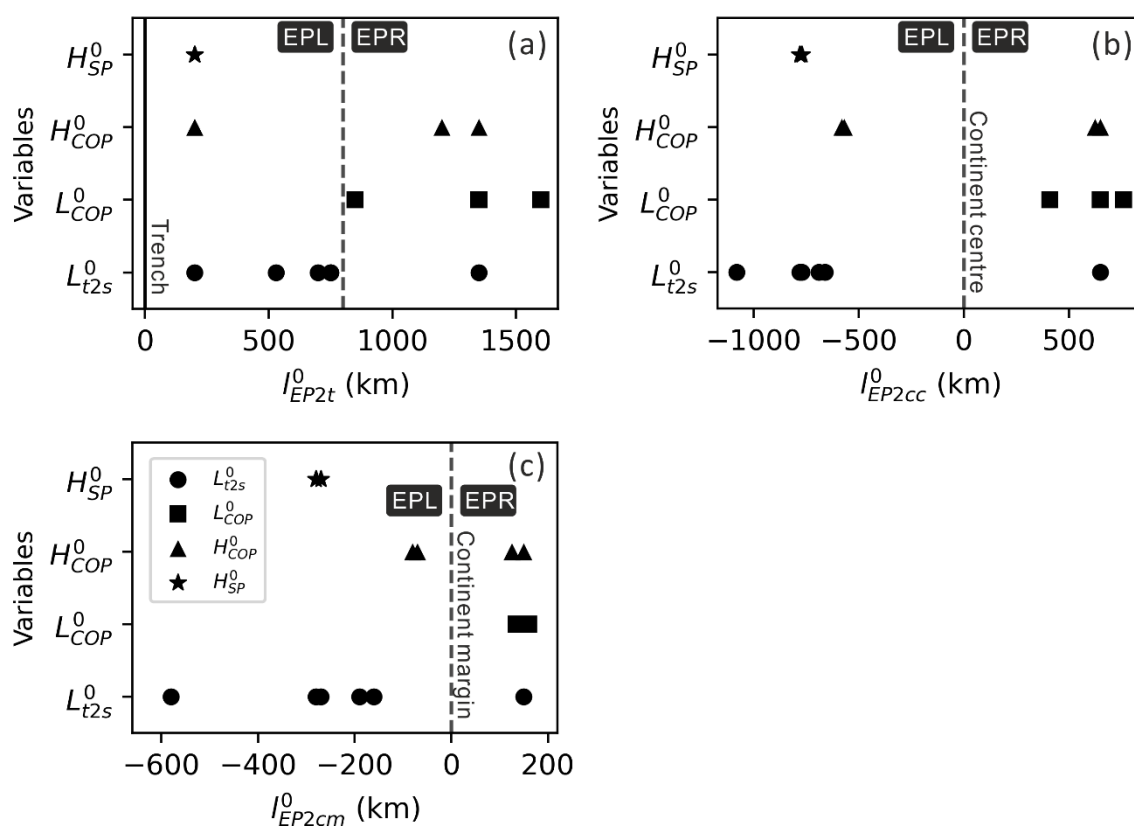
Figure 5.14 Regime diagram of lateral distance from extension centre to three frames of reference. (a) Frame of reference relative to the trench, which is marked with a vertical solid line. (b) Frame of reference relative to the centre of the continental block. (c) Frame of reference relative to the nearest margin of the continental block. Each marker in the subplots represents one of the models with the corresponding variable listed on the vertical axis. The vertical dashed line in all the subplots separates models with EP on the left side of the continental block (EPL) from those where EP develops on the right side of the continental block (EPR). To be noted, two markers on both sides of the dashed line are plotted for models that develop rifting or spreading extension on both sides of the continental block. The legend for the models in all the subplots is displayed in (c).

EPL models, by definition, lie closer to the trench relative than EPR models, and there is a maximum distance of l_{EP2t} that EPL models can achieve, which is ~750 km. Besides, EPL models yield a much wider range of lateral distance away from the margin of the continental block (l_{EP2cm}) than EPR models, with 70~580 km comparing with 125~160 km. A similar conclusion could also be made for the diagnostic l_{EP2cc}.

The visual results in section 5.3.1 show that the width of the extension centre is often wider in EPL models than that in EPR models. In addition, higher total trench retreat in 10 Myr simulation is often observed in EPL models than EPR models.

The results also show that varying L_{t2s}^0 and H_{COP}^0 can generate a transition from EPL to EPR or the other way around, while L_{COP}^0 and H_{SP}^0 fail to do so.

5.4   Discussion

5.4.1 The role of adding continental lithosphere

5.4.1.1   Origin of mechanism to initiate rift extension

There are at least three mechanisms that have been proposed to explain the deformation patterns, especially the extension in the back-arc region of the overriding plate during subduction. The first one assumes that the divergence flow underlying the overriding plate can generate high enough extensional stress gradient to initiate back-arc extension (Dal Zilio et al., 2018; Yang et al., 2019). The second one proposes that mantle wedge flow moving in the same direction can also alter the mobility of the overriding plate, producing a velocity gradient within the overriding plate through heterogeneous basal drag. The high strain rate leads to a reduction in viscosity, strain localisation, and can ultimately lead to extension. A third possibility is that an extensional stress is transmitted across the trench to the overriding plate.

To understand the details of initiating extension within the overriding plate, the velocity difference between the continental block and its marginal surrounding oceanic plates is compared for the three series of models along a horizontal slice at the depth of 20 km (Figure 5.15). For models that do not develop rifting extension within the overriding plate, they tend to develop a low magnitude and flat velocity curve, i.e., without much lateral velocity variation along the selected slice. While for models that produce rifting extension, there is always velocity variation in the proximity of the marginal area of the continental block. For example, the whole overriding plate of model '$H_{COP}^0 = 150\ km$' is moving trench-ward at the rate of 3 cm/yr, which is much slower than that of the other 3 models (Figure 5.15, b). The velocity curve is almost flat within the overriding plate compared with fluctuated curves for the other 3 models, and this model did not produce rifting.
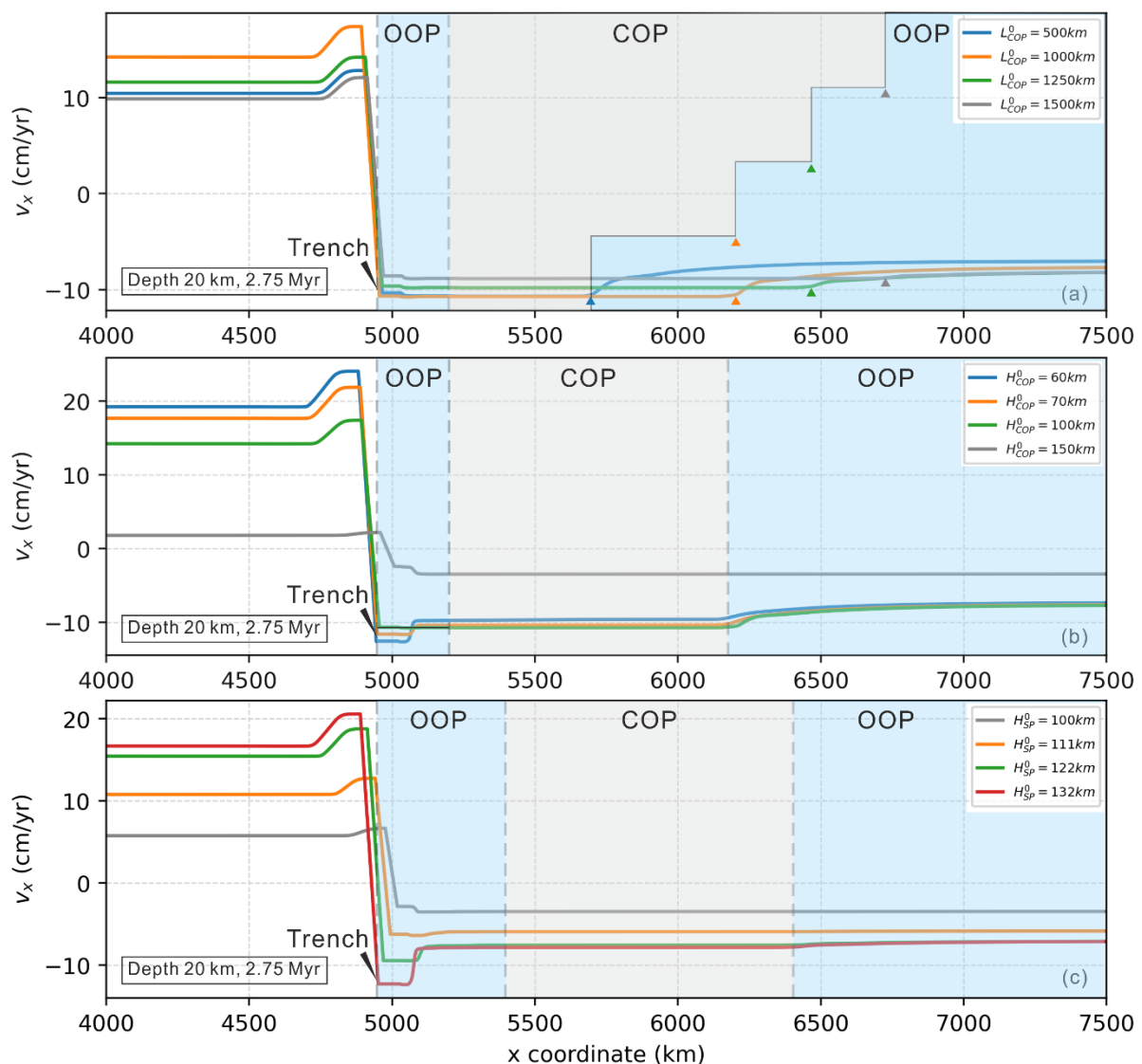
Figure 5.15 Line plot of horizontal velocity along a horizontal slice at the depth of 20 km and timestep of 2.75 Myr. Positive value represent trench-ward motion of subducting slab, and the negtive value is trench-ward motion of the overriding plate. The varation of the magnitude of velocity can be interpreted as compression or extension. The gray lines in all the subplots represent models that do not develop rift extension.

The diagnostic of horizontal stress field along the same horizontal slice at the depth of 20 km within the overriding plate for models with varying H_{SP}^0 (Figure 5.16) is also analysed. The result shows that the horizontal extensional normal stress component in the continental block is much lower than that in the neighbouring oceanic plate, suggesting that the tensional stress is not transmitted across the continental block.

This stress observation also confirms that the rigid continental block is moving as a whole, and little velocity variation or tensional stress develops within it. The location of steep stress gradient matches well with the location where horizontal velocity variation exists along the slice in Figure 5.15, c, indicating that the tensional stress correlates with the velocity jump at the margins of the continent.
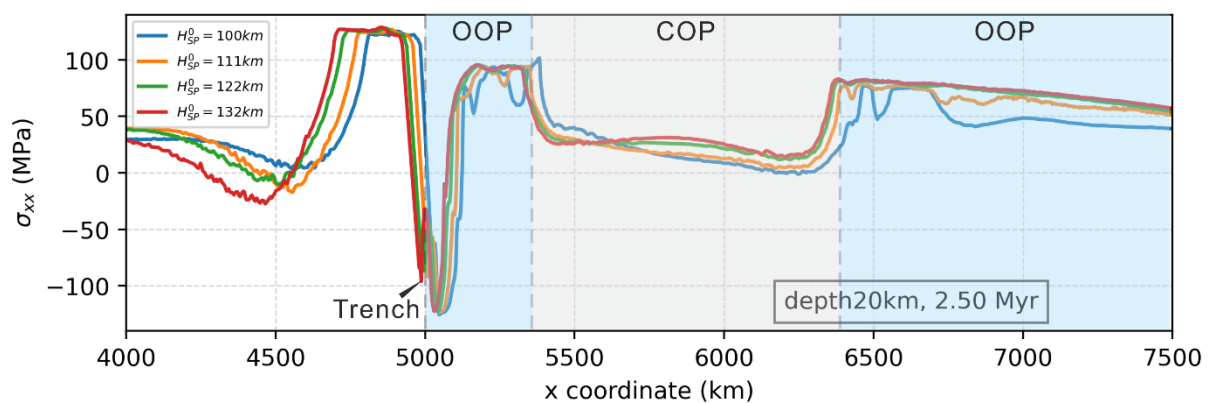
Figure 5.16 Line plot of horizontal stress field along a horizontal slice at the depth of 20 km and timestep of 2.50 Myr. Positive value represent extentional stress, and the negtive value is compressional. OOP is oceanic overriding plate and COP is continental overriding plate.

To summarise, the results of the simulations here support the second type of mechanism as initiating extension within the overriding plate during the subduction process. It is noted that no divergent motion or gradual decreasing horizontal stress is observed within the overriding plate. Instead, the whole overriding plate moves trench-ward as a whole, while there is variation of velocity at the continental margin of the continental block in the lateral direction. The velocity gradient creates significant stress gradient and may end up with rifting or spreading extension at the continental margin.

5.4.1.2   Critical condition to initiate rift extension

The results here show that three out of four tested variables, i.e., L_{COP}^0, H_{COP}^0 and H_{SP}^0, produce models that fail to generate rifting extension within the overriding plate,

indicating that the three variables affect the stretching tendency of the overriding plate. The stretching tendency depends on the creation of high enough velocity difference within the overriding plate through heterogeneous basal drag.

By comparing the results of models with varying initial thickness of the subducting plate at the trench (H_{SP}^0) with those models in Chapter 3, it is noted that adding a continental block within the oceanic overriding plate reduces the minimum H_{SP}^0 (or Age_{SP}^0) it takes to initiate rifting extension within the overriding plate from 132 km to 111 km (Figure 5.17). Equivalently, the minimum Age_{SP}^0 decreases from 175 Ma to 125 Ma. The inclusion of thermal heterogeneity within the oceanic overriding plate significantly increases the tendency to develop viscosity reduction and strain localisation within the lithosphere. This may originate from the fact that the mobility of the thicker continental block is less than the surrounding thinner oceanic plate.
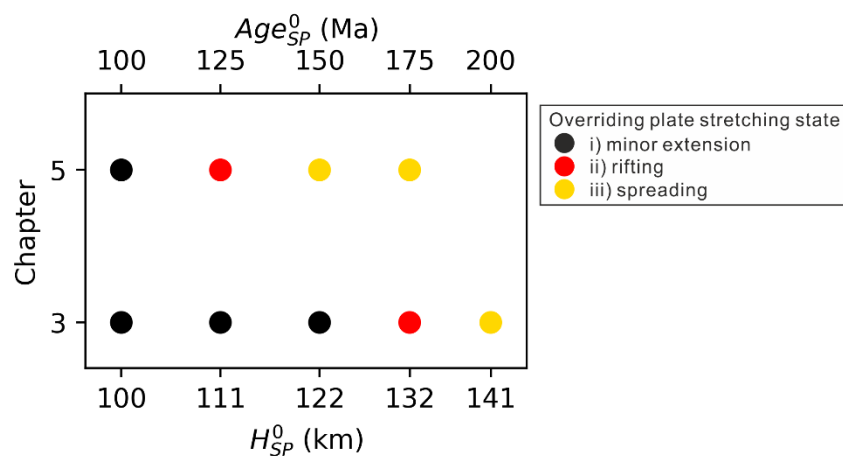
Figure 5.17 Comparison of stretching state diagram with varying H_{SP}^0 (or Age_{SP}^0). The initial thermal thickness of the oceanic overriding plate (characterised by the depth of 1300 K) at trench in all the plotted models is 50 km. The dual horizontal axises show the corresponding value of oceanic plate age and thickness through a half space cooling model.

5.4.1.3 Condition to enable migration of rifting extension

The results also show that varying L_{t2s}^0 and H_{COP}^0 can generate a transition from EPL to EPR or the other way around, while L_{COP}^0 and H_{SP}^0 fail to do so.

EPR models: As H_{COP}^0 increases from 60 km to 150 km, a growing thickness of the continental root protrudes into the underlying mantle. The thickening protruding root may get caught by the trench-ward mantle wind through both basal traction along the root bottom and additional mantle flow push (step push) at its right margin as slab rolls back (Figure 5.18, a). Consequently, the continental block can move trench-ward at a faster pace than the oceanic plate on its sides. This generates compressional velocity gradient at the left margin and extensional velocity gradient at the right margin of the continental block. The latter one can generate extensional stress and induce rifting or spreading extension in the end. On the other hand, the initial distance away from the trench to the left margin of the continental block (L_{t2s}^0) also decides if the extension takes place on the right margin of the continental block. Generally, the slab induced mantle wedge flow decreases away from the trench, and so does the basal traction applied at the bottom of the overriding plate. When L_{t2s}^0 increases to 450 km or more, both the basal traction and the 'step push' becomes so weak that it fails to generate high enough velocity variation to induce rift extension at the right margin of the continental block.
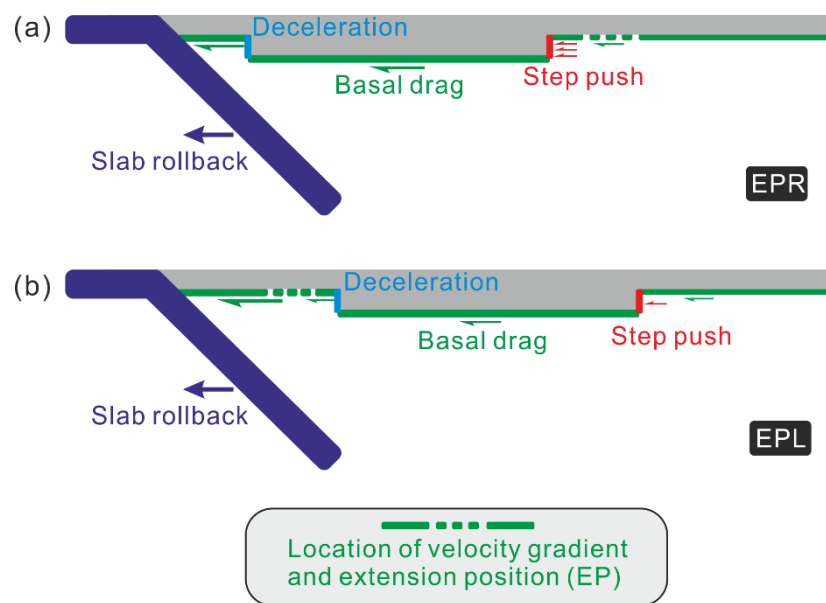
Figure 5.18 Driving mechanism of EPL and EPR models.

EPL models: The thermal step at the left margin of the continental block can slow down the trench-ward mantle wedge flow passing it, thus creating a velocity gradient within the oceanic plate close to the trench (Figure 5.18, b). The slowdown of the mantle wedge flow may also relate to the fact that the less mobile continental block can pose a 'quasi-fixed' velocity boundary condition for the oceanic plate on the left side of the continental block. The 'quasi-fixed' velocity boundary condition can also contribute to the formation of velocity gradient, which promotes the strain localisation at the left margin of the continental block. When L_{t2s}^0 is over 450 km, or H_{COP}^0 is less than 70 km, the integration of basal drag can create high velocity gradient at the left margin of the continental block. Rifting extension starts to develop as the extensional normal stress overtakes the strength of the oceanic plate close to the trench.

In general, the development of extension centres results from the competing ability of the mantle wedge flow to impose velocity gradient on either side of the continental margin. Both L_{t2s}^0 and H_{COP}^0 can regulate the mantle wedge flow and velocity gradient created at the continental margins. In the end, the least viscous part of the overriding

plate becomes the preferred weak position to develop strain localisation and rift extension.

5.4.2 Potential relevance to Earth

There is a wide range of rifting extension duration found in models with different L^0_{COP}: ~1 to 7 Myr. The results yield a variety of distance from extension centre to the trench, (l_{EP2t}) ranging from 200 to 1600 km. Observation at subduction zones on Earth shows that l_{EP2t} can range from 170 km to ~840 km, and the extension duration lasts up to ~14 Myr (Table 5.3). Previous research suggests that increasing the convergence rate, the width of the accreted sedimentary prism, and the age of the subducting plate correlates with longer l_{EP2t} (Cross et al., 1982). Besides, the gradual thickening of the overlying plate through accretion of subduction-related volcanic and plutonic rocks may also play a role to increase l_{EP2t} (Dickinson, 1973; James, 1971).This research here indicates that in addition the distance from the continental block to the trench (L^0_{t2s}), the initial length of the continental block (L^0_{COP}) and the initial thickness of the continental block (H^0_{COP}) can also affect l_{EP2t}.

Table 5.3 Overview of the some diagnostics observed on Earth and their literature source.

Spreading/rifting centre	l_{EP2t} (km)	Extension duration (Myr)	Trench length (km)	Data souce
Bransfield Trough	170	4	650	(Schliffke et al., 2022), and references therein
Sulu Sea	220	4	550	(Schliffke et al., 2022), and references therein
Okinawa Trough	235	6±2	1200	(Schliffke et al., 2022), and references therein
Liguro Basin	260	9±2	560	(Schliffke et al., 2022), and references therein
Cornaglia rifting	265±20	7±3	280±20	(Schliffke et al., 2022), and references therein
Cavilov	310±30	3±1	250±30	(Schliffke et al., 2022), and references therein
Manus Basin	325	3.5	600	(Schliffke et al., 2022), and references therein
Lau Basin	350	5.5	1500	(Schliffke et al., 2022), and references therein
Aleutian Arc	400±200	-	2000	(Cross et al., 1982)
Japan Sea	700±200	10	1400	(Tamaki et al., 1992)
Venezuela Basin	830±40	14±8	800±50	(Schliffke et al., 2022), and references therein
West Scotia Ridge	840±130	13±7	750±20	(Schliffke et al., 2022), and references therein

To be noted, this research is an example of general modelling rather than specific modelling. The intention here of general modelling is to form a diagram with multiple endmembers rather than to reproduce geodynamic evolution of a specific research area (van Zelst et al., 2022). Thus, a detailed comparison of the model results with a specific subduction zone will go beyond the scope of this research. Bearing this in mind, the prediction of the results is cautiously compared with some observations on Earth.

EPL example: Bristol Bay Basin (BBB) develops in the back-arc setting of the Aleutian volcanic arc during the Late Cretaceous-Cenozoic in response to episodes of extension, strike-slip faulting and flexure (Walker et al., 2003). BBB extends north-east towards the Alaska continent along the Aleutian Peninsula and it has ceased

extension. It is observed that as the proportion of continental component in the overriding plate increases landward, the distance from the volcanic arc to the trench increases along the Alaska subduction zone (Cross et al., 1982). This seems to match with the simulation results with a varying L_{t2s}^0, where l_{EP2t} increases with growing L_{t2s}^0. Another EPL example can be the Japan Sea, which lies between the subducting Pacific plate and the Eurasian continent. The major opening process extends from 28 Ma to 18 Ma (Tamaki et al., 1992).

EPR example: The models with varying L_{COP}^0 shows that rift extension becomes difficult to develop at the right margin of the continental block when L_{COP}^0 is longer than 1250 km. In the modern tectonic framework, it is not easy to find a 1500 km long continental block sided by oceanic plates. The South American continent may be a potential candidate. The width of the continent ranges from 1200 km to 5000 km, with the Nazca subducting plate to the west and the Atlantic Ocean to the east. According to the prediction of the model results, there should be magmatic activity or extensional tectonic events to be observed at the east margin of South American continent. In fact, there are linear magmatic records found along the margin, but these are Mesozoic igneous intrusions probably generated during the rifting extension period when the Atlantic Ocean opens (Mohriak and Fainstein, 2012). Cenozoic magmatism is also observed at the east continental margin (Mohriak, 2020), but it is more likely to relate to underlying hot spots rather than the Nazca subduction. Briefly, there is a lack of magmatism evidence along the eastern continental margin that correlates the South American continent with the EPR models. However, there is multiple Cenozoic extensional events which creates normal faults at the east continental margin of Brazil and Argentina (Loegering et al., 2013; Mohriak, 2020). Combining the fact that most of the South American continent is wider than 1500 km, the minor extensional events may originate from the insignificant velocity gradient developed in marginal areas.

5.5   Conclusion

In this chapter, the role of increasing heterogeneity by adding a continental block within the overriding plate is tested in how it affects the formation and localisation of extension during subduction. In detail, the continental lithosphere is configured with either a different initial distance away from the trench (L_{t2s}^0), or different initial extent (L_{COP}^0) or different initial thickness (H_{COP}^0), and the subducting plate is tested with a variety of initial thickness (H_{SP}^0) at the trench.

The results show that increasing the heterogeneity within an oceanic overriding plate by including a continental block controls two first-order features of deformation patterns within the overriding plate: 1) the tendency to develop marginal extension and 2) the position of marginal extension relative to the continental block or the trench.

Varying L_{COP}^0, H_{COP}^0 and H_{SP}^0 can regulate the formation of the rift and spreading extension within the overriding plate. It is observed that the whole continental block moves trench-ward as a whole. To form a rift or spreading extension at a continental margin, it takes a variation of velocity which originates from the heterogenous basal drag. The velocity gradient can create significant stress gradient, which generates a tensional stress field. The velocity gradient can lead to high extensional stress gradient that overcomes the strength of the neighbouring oceanic plate, and form rifting or spreading extension at continental margins during subduction.

Varying L_{t2s}^0 and H_{COP}^0 determines which side the extension develops relative to the continental block, i.e., extension position (EP) on the left side (close to the trench) of the continental block (EPL), and EP on the right side (away from the trench) of the continental block (EPR). In general, the localisation of extension centre results from the competing ability of the mantle wedge flow to impose velocity gradient on either

side of the continental margin. Both L_{t2s}^0 and H_{COP}^0 can regulate the interaction between the trench-ward mantle wedge flow and protruding continental root, which determines the magnitude of velocity gradient developed at the continental margins. In the end, the least viscous part of the overriding plate become the preferred weak position to develop strain localisation and rift extension.

Chapter 6 Conclusion

6.1   Extension tendency comparison

This thesis has investigated the role of high trench retreat rate (Chapter 3), dual inward dipping subduction (Chapter 4), and heterogenous overriding plate (Chapter 5), in generating different deformation patterns within the overriding plate. Chapter 3 investigates single sided subduction with a homogeneous and mobile oceanic overriding plate, and it is reference configuration for the following two chapters. Chapter 4 adds a symmetric subducting slab on the other end of the overriding plate, and Chapter 5 includes a thick continental block into the originally homogenous and mobile oceanic overriding plate. Different extent of extension is observed in each group of simulations, and models with a comparable configuration is compared here (Figure 6.1).
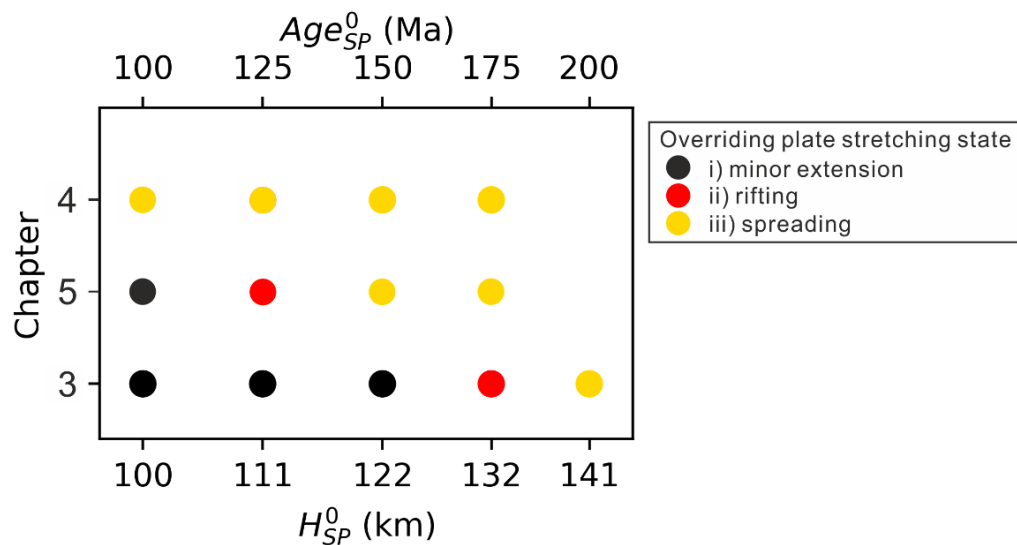
Figure 6.1 Regime diagram of stetching state as a function of subducting plate's initial thickness (or age) and different configurations tested in each chapter. The initial thermal thickness of the oceanic overriding plate (characterised by the depth of 1300 K) at trench is 50 km in all the plotted models. The detailed configuration of the models could be found in Table 4.1 and Table 5.1 separately. The level of extension uses the definition in Chapter 3: minor extension suggests that extension is limited and insignificant; rifting is recognized when the the thermal thickness reduces to <5 km; and spreading extension means the width of thin thermal lithosphere (<5 km) increases after rift extension. The dual horizontal axes show the corresponding value of oceanic plate age and thickness through a half space cooling model.

The result shows that configuring a second subducting slab symmetrically on the other side of the overriding plate and including a thick continental block within the oceanic overriding plate can both increase the extension tendency to form a back-arc or marginal extension within the overriding plate. For example, both dual inward dipping subduction and adding a continental block can produce multiple extension centres in a single simulation (e.g., model '$L_{OP}^0 = 700\ km$' in Chapter 4, and model '$H_{COP}^0 = 70\ km$' in Chapter 5).

Among all the models with a varying initial thickness of the subducting plate, dual-inward dipping subduction is most efficient in producing spreading extension. Its

powerful ability to weaken the overriding plate originates from the self-consistent fixed velocity boundary condition as the inward dipping slabs tend to roll back away from each other (Figure 6.2). Additionally, the two slabs generate two times the mantle wedge flow acting unitedly upon the root of the overriding plate, which can efficiently reduce the viscosity within the overriding plate.

While adding a thick continental block reshapes the mantle wedge flow patterns around the protruding plate root (Figure 6.2). This results in heterogeneous basal traction which drive the formation of a velocity gradient within the overriding plate. When the velocity gradient is sufficiently high, the imposed stress gradient can overcome the strength of the overriding plate and initiate extension processes.

Single sided subduction models in Chapter 3 find it most difficult to self-consistently induce rifting or spreading extension. This is because the mobile overriding plate enables the plate to adjust the internal stress state rather than allow it to accumulate. In addition, the homogeneous initial condition of the overriding plate requires a higher driving force to initiate strain localisation.

In spite of the differences observed in the three groups of models, the simulations share some common processes to generate extension centres within the overriding plate. The high trench retreat rate is not merely the result of the back-arc extension. Instead, the high trench retreat rate is key to generating strong mantle wedge flow, which applies heterogenous basal drag at the root of the overriding plate. As a result, the velocity gradient in the mantle wedge transmits upwards to the overriding plate and induces viscosity reduction within the overriding plate. In return, the softening overriding plate is likely to strengthen the trench retreat motion. Such feedback strengthening process found here may help understand the self-consistent formation of extensional processes developed within the overriding plate during subduction.
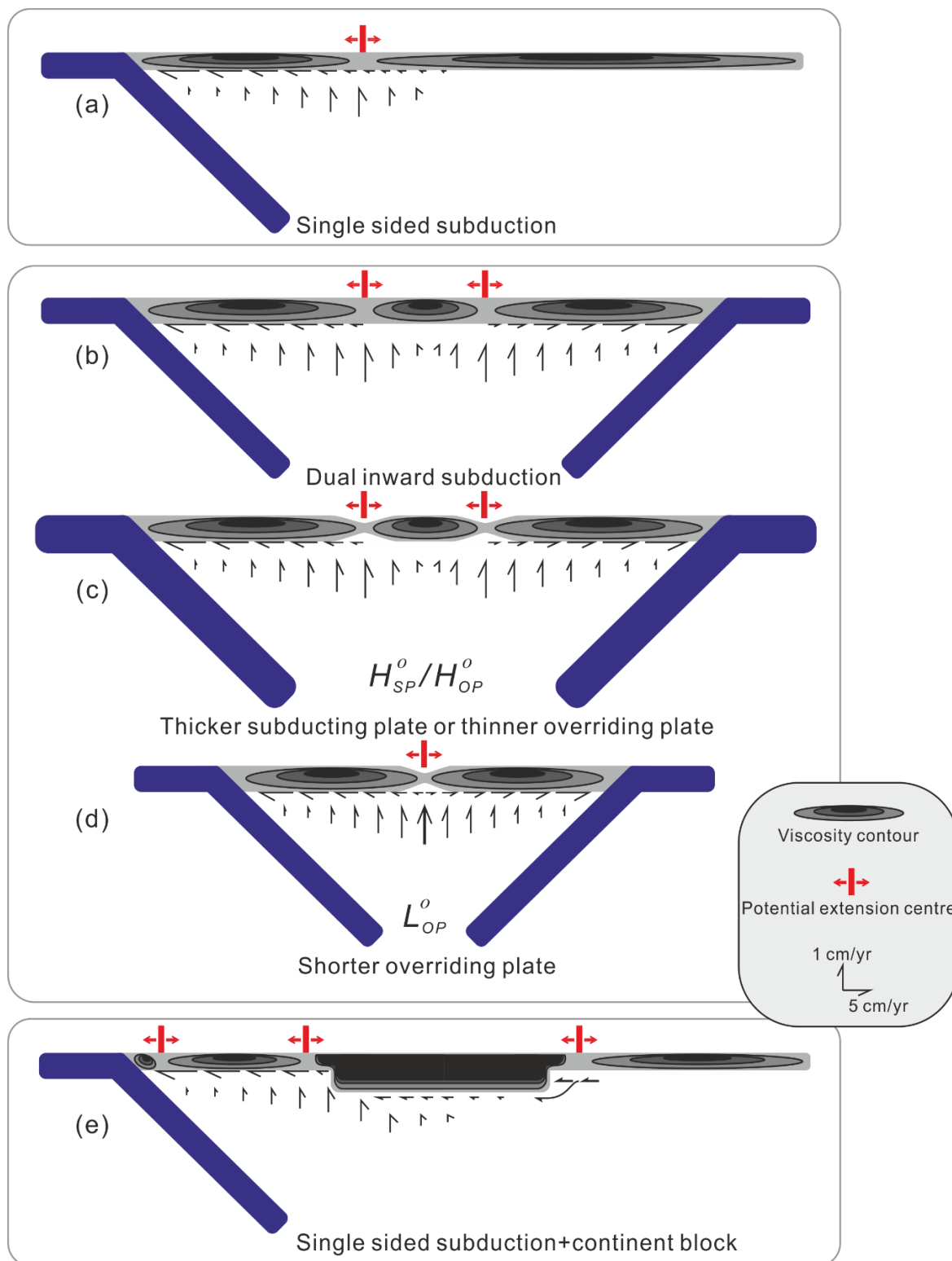
Figure 6.2 Synoptic comparison of different model setups' role in generating extension centres within the overriding plate. (a) Single sided subduction. (b-d) Dual inward dipping subduction. (e) Single sided subduction with a mixed overriding plate of both continental and oceanic proportions.

6.2   Highlights of the study

Chapter 3 shows that dynamic, internally driven subduction models can generate sufficiently high trench retreat rate to initiate focused back-arc extension through non-uniform basal drag, even when the overriding plate is mobile and homogeneous. This is significant because previous research implies that similar spreading back-arc is prone to only develop in models with a fixed overriding plate or an overriding plate containing an arbitrary weak zone. The results could potentially be used to explain the southward decreasing stretching state along the Lau-Havre-Taupo back-arc system where trench retreat rate decreases southward. On the other hand, it is found that an older subducting plate leads to faster trench retreat rate, but this correlation only exists before the slab approaches the lower mantle. This matches well with the observation that the subducting plate age is always old (>55 Ma) in subduction zones with back-arc extension. It also explains why there is a poor correlation between the age of subducting plate and trench retreat rate, because most slabs have already reached the lower mantle. The demonstration of developing back-arc extension in a mobile and homogeneous overriding plate is a significant advance in simulating back-arc extension. Though the trench retreat rate can go higher than what has been observed in current plate framework, suggesting that additional processes may also need to be considered, e.g., melt weakening, grain size reduction etc.

Chapter 4 shows that dynamic, internally driven dual inward dipping subduction (DIDS) models can generate progressive weakening by lowering the magnitude of viscosity within the overriding plate. This is significant because all previous dual inward dipping subduction models applied a compositional rheology where the magnitude of viscosity remains constant. By enabling viscosity to self-consistently evolve with time, the study investigates and quantifies what role dual inward dipping subduction may play in

deforming the overriding plate. Investigation indicates that the length of the overriding plate, the thickness of both the subducting and overriding plate can all substantially affect the deformation state within the overriding plate. Compared with single sided subduction, dual inward dipping subduction reduces the magnitude of viscosity to a lower level within the overriding plate. It does this by creating a dynamic fixed boundary condition for the overriding plate and forming a stronger upwelling mantle flow underlying the overriding plate. Investigation on the evolution of dominant deformation mechanism shows that dislocation and yielding contribute most to induce rifting and spreading extension within the overriding plate. The progressive weakening is mainly driven by the ever-increasing strain rate, which is also a precondition for initiating thermal weakening, strain localisation, lithosphere thinning and formation of new plate boundaries. The incorporation of composite rheology is a significant advance in simulating DIDS, and the quantitative method proposed here to evaluate each deformation mechanism's contribution to viscosity reduction can be a powerful tool to understand other strain localisation processes, e.g., formation of plate boundaries.

Chapter 5 shows that increasing the heterogeneity within an oceanic overriding plate by including a continental block controls two first-order features of deformation patterns within the overriding plate: 1) the tendency to develop marginal extension and 2) the position of marginal extension relative to the continental block or the trench. To form a rift or spreading extension at a continental margin, it takes a variation of velocity which originates from the heterogenous basal drag. The velocity gradient can create significant stress gradient, which generates a tensional stress field. The velocity gradient can lead to high extensional stress gradient that overcomes the strength of the neighbouring oceanic plate, and form rifting or spreading extension at continental margins during subduction. While the localisation of extension centre results from the competing ability of the mantle wedge flow to impose velocity gradient on either side

of the continental margin. In the end, the least viscous part of the overriding plate become the preferred weak position to develop strain localisation and rift extension.

6.3 Outlook

6.3.1 Exploring the rheology parameter space

This thesis mainly investigates the role of plate size and its thermal structure in generating different degrees of deformation (mainly extension) within the overriding plate. The models manage to do so by applying only a single suite of well constrained and widely used rheology parameters (Alsaif et al., 2020; Beall et al., 2021; Garel et al., 2014; Garel and Thoraval, 2021), which poses a strong control on the basal traction induced by the trench-ward mantle wedge flow (the driving force), and the plate strength which resists deformation and strain localisation during subduction.

As the rheology of the lithosphere, especially the mantle component where weakening initiates (Figure 4.15), is still poorly known, there is still a lot of space to explore for the parameters of the composite rheology laws applied. Chapter 4 suggests that yielding and dislocation have played the dominant role in reducing viscosity, initiating necking instability and rifting within the overriding plate. Varying the magnitude of rheology parameters, especially dislocation and yielding, is then likely to alter the position of force balance between the driving force and plate strength. As a result, it may also affect the critical value of plate size to initiate different degrees of deformation within the overriding plate. Thus, it is worth designing further experiments to rigorously investigate the role a wider range of parameter space for dislocation and yielding plays in affecting the tendency to develop extension within the overriding plate.

6.3.2 Incorporating melt weakening

The rheology of the four incorporated deformation mechanisms (Equation 2.7) is dependent on multiple parameters, e.g., temperature, deviatoric stress, strain rate, static pressure etc., which allows the viscosity to self-consistently reduce or strengthen as subduction evolves, generating a variety of deformation patterns in the overriding plate. To be noted, there are other parameters that can substantially affect the magnitude of viscosity for creep deformation, e.g., grain size and melting degree (Bercovici et al., 2015; Braun et al., 1999; England and Katz, 2010; Hirth and Kohlstedt, 2003; Montési and Hirth, 2003), both of which this thesis does not take into consideration.

In particular, grain size reduction is likely to take place when strain builds up and it may make diffusion creep become the dominant deformation mechanism, overtaking dislocation creep, in the mantle lithosphere (Gueydan et al., 2014; Ruh et al., 2022). However, grain size is often in the unit of millimetre or even less which is way beyond the scope of resolution of plate-scale subduction models. This makes it computationally expensive to be included in plate-scale models simulating for 10s of million years (Fuchs and Becker, 2021).

In comparison, melt weakening has been proven to be important in affecting the viscosity of mantle material (England and Katz, 2010; Hirth and Kohlstedt, 2003; Katz et al., 2022, 2003), and computationally feasible to be considered in plate-scale models simulating for 10s of million years (e.g., Duvernay et al., 2022, 2021; England and Katz, 2010; Gülcher et al., 2020). Taking melt weakening into consideration is likely to enhance the plate weakening process in this thesis, which in turn may modify the trench retreat rate it takes to initiate (back-arc) extension or alter the location where strain localises within the overriding plate during subduction. Thus, it is worth

designing further experiments to rigorously investigate the role of creep rheology laws incorporating melt weakening in affecting the tendency to develop extension within the overriding plate.

References

Adam, C., Vidal, V., 2010. Mantle flow drives the subsidence of oceanic plates. Science (80-.). 328, 83–85. https://doi.org/10.1126/science.1185906

Alsaif, M., Garel, F., Gueydan, F., Davies, D.R., 2020. Upper plate deformation and trench retreat modulated by subduction-driven shallow asthenospheric flows. Earth Planet. Sci. Lett. 532, 116013. https://doi.org/10.1016/j.epsl.2019.116013

Anderson, M.O., Norris-Julseth, C., Rubin, K.H., Haase, K., Hannington, M.D., Baxter, A.T., Stewart, M.S., 2021. Geologic and Structural Evolution of the NE Lau Basin, Tonga: Morphotectonic Analysis and Classification of Structures Using Shallow Seismicity. Front. Earth Sci. 9, 1–24. https://doi.org/10.3389/feart.2021.665185

Arnulf, A.F., Bassett, D., Harding, A.J., Kodaira, S., Nakanishi, A., Moore, G., 2022. Upper-plate controls on subduction zone geometry, hydration and earthquake behaviour. Nat. Geosci. 15, 143–148. https://doi.org/10.1038/s41561-021-00879-x

Baes, M., Gerya, T., Sobolev, S. V., 2016. 3-D thermo-mechanical modeling of plume-induced subduction initiation. Earth Planet. Sci. Lett. 453, 193–203. https://doi.org/10.1016/j.epsl.2016.08.023

Bassett, D., Watts, A.B., 2015. Gravity anomalies, crustal structure, and seismicity at subduction zones: 1. Seafloor roughness and subducting relief. Geochemistry, Geophys. Geosystems 16, 1508–1540. https://doi.org/10.1002/2014GC005684

Baxter, A.T., Hannington, M.D., Stewart, M.S., Emberley, J.M., Breker, K., Krätschell, A., Petersen, S., Brandl, P.A., Klischies, M., Mensing, R., Anderson, M.O., 2020. Shallow Seismicity and the Classification of Structures in the Lau Back-Arc Basin. Geochemistry, Geophys. Geosystems 21. https://doi.org/10.1029/2020GC008924

Beall, A., Fagereng, Å., Davies, J.H., Garel, F., Davies, D.R., 2021. Influence of Subduction Zone Dynamics on Interface Shear Stress and Potential Relationship With Seismogenic Behavior. Geochemistry, Geophys. Geosystems 22, 1–20. https://doi.org/10.1029/2020GC009267

Becker, T.W., Conrad, C.P., Buffett, B., Müller, R.D., 2009. Past and present seafloor age distributions and the temporal evolution of plate tectonic heat transport. Earth Planet. Sci. Lett. 278, 233–242. https://doi.org/10.1016/j.epsl.2008.12.007

Becker, T.W., Faccenna, C., 2009. A Review of the Role of Subduction Dynamics for Regional and Global Plate Motions, in: Lallemand, S., Funiciello, F. (Eds.), Subduction Zone Geodynamics. Frontiers in Earth Sciences. Springer, Berlin, Heidelberg, pp. 3–34. https://doi.org/10.1007/978-3-540-87974-9_1

Beniest, A., Schellart, W.P., 2020. A geological map of the Scotia Sea area constrained by bathymetry, geological data, geophysical data and seismic tomography models from the deep mantle. Earth-Science Rev. 210, 103391. https://doi.org/10.1016/j.earscirev.2020.103391

Bercovici, D., Tackley, P.J., Ricard, Y., 2015. The Generation of Plate Tectonics from Mantle Dynamics, in: Treatise on Geophysics: Second Edition. Elsevier B.V., Oxford, pp. 271–318. https://doi.org/10.1016/B978-0-444-53802-4.00135-4

Bevis, M., Taylor, F.W., Schutz, B.E., Recy, J., Isacks, B.L., Helu, S., Singh, R., Kendrick, E., Stowell, J., Taylor, B., Calmantli, S., 1995. Geodetic observations of very rapid convergence and back-arc extension at the tonga arc. Nature 374, 249–251. https://doi.org/10.1038/374249a0

Billen, M.I., Hirth, G., 2007. Rheologic controls on slab dynamics. Geochemistry, Geophys. Geosystems 8, 8012. https://doi.org/10.1029/2007GC001597

Braszus, B., Goes, S., Allen, R., Rietbrock, A., Collier, J., Harmon, N., Henstock, T., Hicks, S., Rychert, C.A., Maunder, B., van Hunen, J., Bie, L., Blundy, J., Cooper, G., Davy, R., Kendall, J.M., Macpherson, C., Wilkinson, J., Wilson, M., 2021. Subduction history of the Caribbean from upper-mantle seismic imaging and plate reconstruction. Nat. Commun. 12. https://doi.org/10.1038/s41467-021-24413-0

Braun, J., Chéry, J., Poliakov, A., Mainprice, D., Vauchez, A., Tomassi, A., Daignières, M., 1999. A simple parameterization of strain localization in the ductile regime due to grain size reduction: A case study for olivine. J. Geophys. Res. Solid Earth 104, 25167–25181.

Brune, S., Williams, S.E., Butterworth, N.P., Müller, R.D., 2016. Abrupt plate accelerations shape rifted continental margins. Nature 536, 201–204. https://doi.org/10.1038/nature18319

Bürgmann, R., Dresen, G., 2008. Rheology of the lower crust and upper mantle: Evidence from rock mechanics, geodesy, and field observations. Annu. Rev. Earth Planet. Sci. 36, 531–567. https://doi.org/10.1146/annurev.earth.36.031207.124326

Burov, E., Guillou-Frottier, L., 2005. The plume head-continental lithosphere

interaction using a tectonically realistic formulation for the lithosphere. Geophys. J. Int. 161, 469–490. https://doi.org/10.1111/j.1365-246X.2005.02588.x

Burov, E.B., 2011. Rheology and strength of the lithosphere. Mar. Pet. Geol. 28, 1402–1443. https://doi.org/10.1016/j.marpetgeo.2011.05.008

Butterworth, N.P., Quevedo, L., Morra, G., Müller, R.D., 2012. Influence of overriding plate geometry and rheology on subduction. Geochemistry, Geophys. Geosystems 13, 1–15. https://doi.org/10.1029/2011GC003968

Butterworth, N.P., Talsma, A.S., Müller, R.D., Seton, M., Bunge, H.P., Schuberth, B.S.A., Shephard, G.E., Heine, C., 2014. Geological, tomographic, kinematic and geodynamic constraints on the dynamics of sinking slabs. J. Geodyn. 73, 1–13. https://doi.org/10.1016/j.jog.2013.10.006

Byerlee, J., 1978. Friction of rocks. Pure Appl. Geophys. PAGEOPH 116, 615–626. https://doi.org/10.1007/BF00876528

Candioti, L.G., Schmalholz, S.M., Duretz, T., 2020. Impact of upper mantle convection on lithosphere hyperextension and subsequent horizontally forced subduction initiation. Solid Earth 11, 2327–2357. https://doi.org/10.5194/se-11-2327-2020

Capitanio, F.A., Stegman, D.R., Moresi, L.N., Sharples, W., 2010. Upper plate controls on deep subduction, trench migrations and deformations at convergent margins. Tectonophysics 483, 80–92. https://doi.org/10.1016/j.tecto.2009.08.020

Caratori Tontini, F., Bassett, D., de Ronde, C.E.J.J., Timm, C., Wysoczanski, R., 2019. Early evolution of a young back-arc basin in the Havre Trough. Nat. Geosci. 12, 856–862. https://doi.org/10.1038/s41561-019-0439-y

Chekhovich, V.D., Sukhov, A.N., Sheremet, O.G., Kononov, M. V., 2012. Cenozoic geodynamics of the Bering Sea region. Geotectonics 46, 212–231. https://doi.org/10.1134/S001685211203003X

Chen, Z., Schellart, W.P., Duarte, J.C., 2015. Overriding plate deformation and variability of fore-arc deformation during subduction: Insight from geodynamic models and application to the Calabria subduction zone. Geochemistry, Geophys. Geosystems 16, 3697–3715. https://doi.org/10.1002/2015GC005958

Chen, Z., Schellart, W.P., Strak, V., Duarte, J.C., 2016. Does subduction-induced mantle flow drive backarc extension? Earth Planet. Sci. Lett. 441, 200–210. https://doi.org/10.1016/j.epsl.2016.02.027

Chertova, M. V., Geenen, T., Van Den Berg, A., Spakman, W., 2012. Using open sidewalls for modelling self-consistent lithosphere subduction dynamics. Solid Earth 3, 313–326. https://doi.org/10.5194/se-3-313-2012

Christeson, G.L., Barth, G.A., 2015. Aleutian basin oceanic crust. Earth Planet. Sci. Lett. 426, 167–175. https://doi.org/10.1016/j.epsl.2015.06.040

Čížková, H., Bina, C.R., 2015. Geodynamics of trench advance: Insights from a Philippine-Sea-style geometry. Earth Planet. Sci. Lett. 430, 408–415. https://doi.org/10.1016/j.epsl.2015.07.004

Čížková, H., Bina, C.R., 2013. Effects of mantle and subduction-interface rheologies on slab stagnation and trench rollback. Earth Planet. Sci. Lett. 379, 95–103. https://doi.org/10.1016/j.epsl.2013.08.011

Cloetingh, S., Koptev, A., Kovács, I., Gerya, T., Beniest, A., Willingshofer, E., Ehlers, T.A., Andrić-Tomašević, N., Botsyun, S., Eizenhöfer, P.R., François, T.,

Beekman, F., 2021. Plume-Induced Sinking of Intracontinental Lithospheric Mantle: An Overlooked Mechanism of Subduction Initiation? Geochemistry, Geophys. Geosystems 22, 1–25. https://doi.org/10.1029/2020GC009482

Coltice, N., Rolf, T., Tackley, P.J., Labrosse, S., 2012. Dynamic causes of the relation between area and age of the ocean floor. Science (80-.). 336, 335–338. https://doi.org/10.1126/science.1219120

Conder, J.A., Wiens, D.A., 2007. Rapid mantle flow beneath the Tonga volcanic arc. Earth Planet. Sci. Lett. 264, 299–307. https://doi.org/10.1016/j.epsl.2007.10.014

Conrad, C.P., Lithgow-Bertelloni, C., 2002. How mantle slabs drive plate tectonics. Science (80-.). 298, 207–209. https://doi.org/10.1126/science.1074161

Crameri, F., Magni, V., Domeier, M., Shephard, G.E., Chotalia, K., Cooper, G., Eakin, C.M., Grima, A.G., Gürer, D., Király, Á., Mulyukova, E., Peters, K., Robert, B., Thielmann, M., 2020. A transdisciplinary and community-driven database to unravel subduction zone initiation. Nat. Commun. 11, 3750. https://doi.org/10.1038/s41467-020-17522-9

Crameri, F., Montési, L., Lithgow-Bertelloni, C.R., 2019. The dynamic life of an oceanic plate. Tectonophysics 760, 107–135. https://doi.org/10.1016/J.TECTO.2018.03.016

Crameri, F., Tackley, P.J., Meilick, I., Gerya, T. V., Kaus, B.J.P., 2012. A free plate surface and weak oceanic crust produce single-sided subduction on Earth. Geophys. Res. Lett. 39, 1–7. https://doi.org/10.1029/2011GL050046

Cross, T.A., Pilger, R.H., PILGER Jr, R.E.X.H., 1982. Controls of subduction geometry location of magmatic arcs and tectonics of arc and back-arc regions. Geol. Soc.

Am. Bull. 93, 545–562. https://doi.org/10.1130/0016-7606(1982)93<545:COSGLO>2.0.CO;2

Currie, C.A., Huismans, R.S., Beaumont, C., 2008. Thinning of continental backarc lithosphere by flow-induced gravitational instability. Earth Planet. Sci. Lett. 269, 436–447. https://doi.org/10.1016/j.epsl.2008.02.037

Dal Zilio, L., Faccenda, M., Capitanio, F., 2018. The role of deep subduction in supercontinent breakup. Tectonophysics 746, 312–324. https://doi.org/10.1016/j.tecto.2017.03.006

Dang, Z., Zhang, N., Li, Z.-X., Huang, C., Spencer, C.J., Liu, Y., 2020. Weak orogenic lithosphere guides the pattern of plume-triggered supercontinent break-up. Commun. Earth Environ. 1, 51. https://doi.org/10.1038/s43247-020-00052-z

Dasgupta, R., Mandal, N., 2018. Surface topography of the overriding plates in bi-vergent subduction systems: A mechanical model. Tectonophysics 746, 280–295. https://doi.org/10.1016/j.tecto.2017.08.008

Davies, D.R., Le Voci, G., Goes, S., Kramer, S.C., Wilson, C.R., 2016. The mantle wedge's transient 3-D flow regime and thermal structure. Geochemistry, Geophys. Geosystems 17, 78–100. https://doi.org/10.1002/2015GC006125

Davies, D.R., Valentine, A.P., Kramer, S.C., Rawlinson, N., Hoggard, M.J., Eakin, C.M., Wilson, C.R., 2019. Earth's multi-scale topographic response to global mantle flow. Nat. Geosci. 12, 845–850. https://doi.org/10.1038/s41561-019-0441-4

Davies, D.R., Wilson, C.R., Kramer, S.C., 2011. Fluidity: A fully unstructured anisotropic adaptive mesh computational modeling framework for geodynamics.

Geochemistry, Geophys. Geosystems 12, n/a-n/a. https://doi.org/10.1029/2011GC003551

Davies, J.H., Davies, D.R., 2010. Earth's surface heat flux. Solid Earth 1, 5–24. https://doi.org/10.5194/se-1-5-2010

Di Giuseppe, E., Van Hunen, J., Funiciello, F., Faccenna, C., Giardini, D., 2008. Slab stiffness control of trench motion: Insights from numerical models. Geochemistry, Geophys. Geosystems 9, 1–19. https://doi.org/10.1029/2007GC001776

Dickinson, W.R., 1973. Widths of modern arc-trench gaps proportional to past duration of igneous activity in associated magmatic arcs 78. https://doi.org/10.1029/JB078i017p03376

Duvernay, T., Davies, D.R., Mathews, C.R., Gibson, A.H., 2022. Continental Magmatism : The Surface Manifestation of Dynamic Interactions Between Cratonic Lithosphere , Mantle Plumes and Edge-Driven Convection Geochemistry , Geophysics , Geosystems. https://doi.org/10.1029/2022GC010363

Duvernay, T., Davies, D.R., Mathews, C.R., Gibson, A.H., Kramer, S.C., 2021. Linking Intraplate Volcanism to Lithospheric Structure and Asthenospheric Flow. Geochemistry, Geophys. Geosystems 22, 1–29. https://doi.org/10.1029/2021GC009953

Eagles, G., Jokat, W., 2014. Tectonic reconstructions for paleobathymetry in Drake Passage. Tectonophysics 611, 28–50. https://doi.org/10.1016/j.tecto.2013.11.021

East, M., Müller, R.D., Williams, S., Zahirovic, S., Heine, C., 2020. Subduction history

reveals Cretaceous slab superflux as a possible cause for the mid-Cretaceous plume pulse and superswell events. Gondwana Res. 79, 125–139. https://doi.org/10.1016/j.gr.2019.09.001

Elsasser, W.M., 1971. Sea-floor spreading as thermal convection. J. Geophys. Res. 76, 1101–1112. https://doi.org/10.1029/JB076i005p01101

England, P.C., Katz, R.F., 2010. Melting above the anhydrous solidus controls the location of volcanic arcs. Nature 467, 700–703. https://doi.org/10.1038/nature09417

Erdős, Z., Huismans, R.S., Faccenna, C., Wolf, S.G., 2021. The role of subduction interface and upper plate strength on back-arc extension: Application to Mediterranean back-arc basins. Tectonics 40. https://doi.org/10.1029/2021TC006795

Ewart, A., Collerson, K.D., Regelous, M., Wendt, J.I., Niu, Y., 1998. Geochemical evolution within the Tonga-Kermadec-Lau Arc-Back-arc systems: The role of varying mantle wedge composition in space and time. J. Petrol. 39, 331–368. https://doi.org/10.1093/petroj/39.3.331

Faccenna, C., Becker, T.W., Holt, A.F., Brun, J.P., 2021. Mountain building, mantle convection, and supercontinents: Holmes (1931) revisited. Earth Planet. Sci. Lett. 564, 116905. https://doi.org/10.1016/j.epsl.2021.116905

Faccenna, C., Becker, T.W., Lallemand, S., Lagabrielle, Y., Funiciello, F., Piromallo, C., 2010. Subduction-triggered magmatic pulses: A new class of plumes? Earth Planet. Sci. Lett. 299, 54–68. https://doi.org/10.1016/j.epsl.2010.08.012

Faccenna, C., Holt, A.F., Becker, T.W., Lallemand, S., Royden, L.H., 2018. Dynamics

of the Ryukyu/Izu-Bonin-Marianas double subduction system. Tectonophysics 746, 229–238. https://doi.org/10.1016/j.tecto.2017.08.011

Ficini, E., Dal Zilio, L., Doglioni, C., Gerya, T. V., 2017. Horizontal mantle flow controls subduction dynamics. Sci. Rep. 7, 7550. https://doi.org/10.1038/s41598-017-06551-y

Forsyth, D., Uyeda, S., 1975. On the Relative Importance of the Driving Forces of Plate Motion. Geophys. J. Int. 43, 163–200. https://doi.org/10.1111/j.1365-246X.1975.tb00631.x

Fouquet, Y., Stackelberg, U. Von, Charlou, J.L., Donval, J.P., Erzinger, J., Foucher, J.P., Herzig, P., Mühe, R., Soakai, S., Wiedicke, M., Whitechurch, H., 1991. Hydrothermal activity and metallogenesis in the Lau back-arc basin. Nature 349, 778–781. https://doi.org/10.1038/349778a0

Fowler, C., 2005. The Solid Earth: An Introduction to Global Geophysics. Cambridge Univ. Press, Cambridge, U. K.

Fuchs, L., Becker, T.W., 2021. Deformation memory in the lithosphere: A comparison of damage-dependent weakening and grain-size sensitive rheologies. J. Geophys. Res. Solid Earth 126, 1–22. https://doi.org/10.1029/2020JB020335

Fuchs, L., Becker, T.W., 2019. Role of strain-dependent weakening memory on the style of mantle convection and plate boundary stability. Geophys. J. Int. 218, 601–618. https://doi.org/10.1093/gji/ggz167

Fukao, Y., Obayashi, M., Nakakuki, T., 2009. Stagnant Slab: A Review. Annu. Rev. Earth Planet. Sci. 37, 19–46. https://doi.org/10.1146/annurev.earth.36.031207.124224

Funiciello, F., Faccenna, C., Giardini, D., 2004. Role of lateral mantle flow in the evolution of subduction systems: Insights from laboratory experiments. Geophys. J. Int. 157, 1393–1406. https://doi.org/10.1111/j.1365-246X.2004.02313.x

Garel, F., Goes, S., Davies, D.R., Davies, J.H., Kramer, S.C., Wilson, C.R., 2014. Interaction of subducted slabs with the mantle transition-zone: A regime diagram from 2-D thermo-mechanical models with a mobile trench and an overriding plate. Geochemistry, Geophys. Geosystems 15, 1739–1765. https://doi.org/10.1002/2014GC005257

Garel, F., Thoraval, C., 2021. Lithosphere as a constant-velocity plate: Chasing a dynamical LAB in a homogeneous mantle material. Phys. Earth Planet. Inter. 316, 106710. https://doi.org/10.1016/j.pepi.2021.106710

Garel, F., Thoraval, C., Tommasi, A., Demouchy, S., Davies, D.R., 2020. Using thermo-mechanical models of subduction to constrain effective mantle viscosity. Earth Planet. Sci. Lett. 539. https://doi.org/10.1016/j.epsl.2020.116243

Gerya, T., 2022. Numerical modeling of subduction: State of the art and future direction. Geosphere. https://doi.org/10.1130/GES02416.1

Gerya, T., Stern, J., Sobolev, S., Whattam, S.A., 2015. Plate tectonics on the Earth triggered by plume-induced subduction initiation. https://doi.org/10.1038/nature15752

Gerya, T. V., Connolly, J.A.D., Yuen, D.A., 2008. Why is terrestrial subduction one-sided? Geology 36, 43–46. https://doi.org/10.1130/G24060A.1

Goes, S., Agrusta, R., van Hunen, J., Garel, F., 2017. Subduction-transition zone interaction: A review. Geosphere 13, 644–664.

https://doi.org/10.1130/GES01476.1

Gueydan, F., Précigout, J., Montési, L.G.J., 2014. Strain weakening enables continental plate tectonics. Tectonophysics 631, 189–196. https://doi.org/10.1016/j.tecto.2014.02.005

Gülcher, A.J.P., Gerya, T. V., Montési, L.G.J., Munch, J., 2020. Corona structures driven by plume–lithosphere interactions and evidence for ongoing plume activity on Venus. Nat. Geosci. 13, 547–554. https://doi.org/10.1038/s41561-020-0606-1

Halbach, P., Nakamura, K., Wahsner, M., Lange, J., Sakai, H., Käselitz, L., Hansen, R.-D., Yamano, M., Post, J., Prause, B., Seifert, R., Michaelis, W., Teichmann, F., Kinoshita, M., Märten, A., Ishibashi, J., Czerwinski, S., Blum, N., 1989. Probable modern analogue of Kuroko-type massive sulphide deposits in the Okinawa Trough back-arc basin. Nature 338, 496–499. https://doi.org/10.1038/338496a0

Hall, C.E., Gurnis, M., Sdrolias, M., Lavier, L.L., Müller, R.D., 2003. Catastrophic initiation of subduction following forced convergence across fracture zones. Earth Planet. Sci. Lett. 212, 15–30. https://doi.org/10.1016/S0012-821X(03)00242-5

Hall, R., Spakman, W., 2015. Mantle structure and tectonic history of SE Asia. Tectonophysics 658, 14–45. https://doi.org/10.1016/j.tecto.2015.07.003

Hawkins, J.W., 1995. The Geology of the Lau Basin, in: Taylor, B. (Ed.), Backarc Basins: Tectonics and Magmatism. Springer US, Boston, MA, pp. 63–138. https://doi.org/10.1007/978-1-4615-1843-3_3

He, L., 2015. Thermal regime of the North China Craton: Implications for craton destruction. Earth-Science Rev. 140, 14–26.

https://doi.org/10.1016/j.earscirev.2014.10.011

He, L., 2014. Numerical modeling of convective erosion and peridotite-melt interaction in big mantle wedge: Implications for the destruction of the North China Craton. J. Geophys. Res. Solid Earth 119, 3662–3677. https://doi.org/10.1002/2013JB010657

Hertgen, S., Yamato, P., Guillaume, B., Magni, V., Schliffke, N., Hunen, J., van Hunen, J., 2020. Influence of the thickness of the overriding plate on convergence zone dynamics. Geochemistry, Geophys. Geosystems 21. https://doi.org/10.1029/2019GC008678

Hess, H.H., 1962. History of Ocean Basins, in: Engel, A.E.J., James, H.L., Leonard, B.F. (Eds.), Petrologic Studies. Geological Society of America, USA, pp. 599–620. https://doi.org/10.1130/Petrologic.1962.599

Hessler, A.M., Sharman, G.R., 2018. Subduction zones and their hydrocarbon systems. Geosphere 14, 2044–2067. https://doi.org/10.1130/GES01656.1

Heuret, A., Lallemand, S., 2005. Plate motions, slab dynamics and back-arc deformation. Phys. Earth Planet. Inter. 149, 31–51. https://doi.org/10.1016/j.pepi.2004.08.022

Hirth, G., Kohlstedt, D., 2003. Rheology of the upper mantle and the mantle wedge: A view from the experimentalists, in: Eiler, J. (Ed.), Inside the Subduction Factory. American Geophysical Union, pp. 83–105. https://doi.org/10.1029/138GM06

Hirth, G., Kohlstedt, D.L., 1995a. Experimental constraints on the dynamics of the partially molten upper mantle: Deformation in the diffusion creep regime. J. Geophys. Res. Solid Earth 100, 1981–2001.

https://doi.org/https://doi.org/10.1029/94JB02128

Hirth, G., Kohlstedt, D.L., 1995b. Experimental constraints on the dynamics of the partially molten upper mantle 2. Deformation in the dislocation creep regime. J. Geophys. Res. 100, 1981–2001. https://doi.org/10.1029/95jb01292

Hoernle, K., Gill, J., Timm, C., Hauff, F., Werner, R., Garbe-Schönberg, D., Gutjahr, M., 2021. Hikurangi Plateau subduction a trigger for Vitiaz arc splitting and Havre Trough opening (southwestern Pacific). Geology 49, 536–540. https://doi.org/10.1130/g48436.1

Holt, A.F., Becker, T.W., 2017. The effect of a power-law mantle viscosity on trench retreat rate. Geophys. J. Int. 208, 491–507. https://doi.org/10.1093/gji/ggw392

Holt, A.F., Becker, T.W., Buffett, B.A., 2015a. Trench migration and overriding plate stress in dynamic subduction models. Geophys. J. Int. 201, 172–192. https://doi.org/10.1093/gji/ggv011

Holt, A.F., Buffett, B.A., Becker, T.W., 2015b. Overriding plate thickness control on subducting plate curvature. Geophys. Res. Lett. 42, 3802–3810. https://doi.org/10.1002/2015GL063834

Holt, A.F., Royden, L.H., Becker, T.W., 2017. The Dynamics of Double Slab Subduction. Geophys. J. Int. 209, ggw496. https://doi.org/10.1093/gji/ggw496

Huang, Z., Li, H., Zheng, Y., Peng, Y., 2009. The lithosphere of North China Craton from surface wave tomography. Earth Planet. Sci. Lett. 288, 164–173. https://doi.org/10.1016/j.epsl.2009.09.019

Huang, Z., Zhao, D., Wang, L., 2015. P wave tomography and anisotropy beneath

Southeast Asia: Insight into mantle dynamics. J. Geophys. Res. Solid Earth 120, 5154–5174. https://doi.org/10.1002/2015JB012098

Husson, L., 2012. Trench migration and upper plate strain over a convecting mantle. Phys. Earth Planet. Inter. 212–213, 32–43. https://doi.org/10.1016/j.pepi.2012.09.006

Jadamec, M.A., Billen, M.I., 2010. Reconciling surface plate motions with rapid three-dimensional mantle flow around a slab edge. Nature 465, 338–341. https://doi.org/10.1038/nature09053

Jagoutz, O., Royden, L., Holt, A.F., Becker, T.W., 2015. Anomalously fast convergence of India and Eurasia caused by double subduction. Nat. Geosci. 8, 475–478. https://doi.org/10.1038/ngeo2418

James, D.E., 1971. Plate tectonic model for the evolution of the Central Andes. Geol. Soc. Am. Bull. 82, 3325–3346. https://doi.org/10.1130/0016-7606(1971)82[3325:PTMFTE]2.0.CO;2

Jolivet, L., Tamaki, K., Fournier, M., 1994. Japan Sea, opening history and mechanism: a synthesis. J. Geophys. Res. 99. https://doi.org/10.1029/93jb03463

Jones, T.D., Davies, D.R., Campbell, I.H., Wilson, C.R., Kramer, S.C., 2016. Do mantle plumes preserve the heterogeneous structure of their deep-mantle source? Earth Planet. Sci. Lett. 434, 10–17. https://doi.org/10.1016/j.epsl.2015.11.016

Kameyama, M., Yuen, D.A., Karato, S.I., 1999. Thermal-mechanical effects of low-temperature plasticity (the Peierls mechanism) on the deformation of a viscoelastic shear zone. Earth Planet. Sci. Lett. 168, 159–172.

https://doi.org/10.1016/S0012-821X(99)00040-0

Karato, S. ichiro, 2010. Rheology of the Earth's mantle: A historical review. Gondwana Res. 18, 17–45. https://doi.org/10.1016/j.gr.2010.03.004

Katz, R.F., Jones, D.W.R., Rudge, J.F., Keller, T., 2022. Physics of Melt Extraction from the Mantle: Speed and Style 507–540.

Katz, R.F., Spiegelman, M., Langmuir, C.H., 2003. A new parameterization of hydrous mantle melting. Geochemistry, Geophys. Geosystems 4, 1–19. https://doi.org/10.1029/2002GC000433

Király, Á., Capitanio, F.A., Funiciello, F., Faccenna, C., 2017. Subduction induced mantle flow: Length-scales and orientation of the toroidal cell. Earth Planet. Sci. Lett. 479, 284–297. https://doi.org/10.1016/j.epsl.2017.09.017

Király, Á., Funiciello, F., Capitanio, F.A., Faccenna, C., 2021. Dynamic interactions between subduction zones. Glob. Planet. Change 202, 103501. https://doi.org/10.1016/j.gloplacha.2021.103501

Király, Á., Holt, A.F., Funiciello, F., Faccenna, C., Capitanio, F.A., 2018. Modeling slab-slab interactions: Dynamics of outward dipping double-sided subduction systems. Geochemistry, Geophys. Geosystems 19, 693–714. https://doi.org/10.1002/2017GC007199

Knight, B.S., Davies, J.H., Capitanio, F.A., 2021. Timescales of successful and failed subduction: insights from numerical modelling. Geophys. J. Int. 225, 261–276. https://doi.org/10.1093/gji/ggaa410

Korenaga, J., 2013. Initiation and evolution of plate tectonics on earth: Theories and

observations. Annu. Rev. Earth Planet. Sci. 41, 117–151. https://doi.org/10.1146/annurev-earth-050212-124208

Korenaga, T., Korenaga, J., 2008. Subsidence of normal oceanic lithosphere, apparent thermal expansivity, and seafloor flattening. Earth Planet. Sci. Lett. 268, 41–51. https://doi.org/10.1016/j.epsl.2007.12.022

Korenaga, T., Korenaga, J., Kawakatsu, H., Yamano, M., 2021. A New Reference Model for the Evolution of Oceanic Lithosphere in a Cooling Earth. J. Geophys. Res. https://doi.org/10.1029/2020jb021528

Kósik, S., Bebbington, M., Németh, K., 2020. Spatio-temporal hazard estimation in the central silicic part of Taupo Volcanic Zone, New Zealand, based on small to medium volume eruptions. Bull. Volcanol. 82. https://doi.org/10.1007/s00445-020-01392-6

Kramer, S.C., Davies, D.R., Wilson, C.R., 2021. Analytical solutions for mantle flow in cylindrical and spherical shells. Geosci. Model Dev. 14, 1899–1919. https://doi.org/10.5194/gmd-14-1899-2021

Kramer, S.C., Wilson, C.R., Davies, D.R., 2012. An implicit free surface algorithm for geodynamical simulations. Phys. Earth Planet. Inter. 194–195, 25–37. https://doi.org/10.1016/j.pepi.2012.01.001

Kreemer, C., Blewitt, G., Klein, E.C., 2014. A geodetic plate motion and Global Strain Rate Model. Geochemistry, Geophys. Geosystems 15, 3849–3889. https://doi.org/10.1002/2014GC005407

Kusky, T.M., 2022. Déjà vu: Might Future Eruptions of Hunga Tonga-Hunga Ha'apai Volcano be a Repeat of the Devastating Eruption of Santorini, Greece (1650 BC)?

J. Earth Sci. https://doi.org/10.1007/s12583-022-1624-2

Lallemand, S., Heuret, A., Boutelier, D., 2005. On the relationships between slab dip, back-arc stress, upper plate absolute motion, and crustal nature in subduction zones. Geochemistry, Geophys. Geosystems 6. https://doi.org/10.1029/2005GC000917

Lallemand, S., Jolivet, L., 1986. Japan Sea: a pull-apart basin? Earth Planet. Sci. Lett. 76, 375–389. https://doi.org/10.1016/0012-821X(86)90088-9

Le Voci, G., Davies, D.R., Goes, S., Kramer, S.C., Wilson, C.R., 2014. A systematic 2-D investigation into the mantle wedge's transient flow regime and thermal structure: Complexities arising from a hydrated rheology and thermal buoyancy. Geochemistry, Geophys. Geosystems 15, 28–51. https://doi.org/10.1002/2013GC005022

Leat, P.T., Livermore, R.A., Millar, I.L., Pearce, J.A., 2000. Magma supply in back-arc spreading centre segment E2, East Scotia Ridge. J. Petrol. 41, 845–866. https://doi.org/10.1093/petrology/41.6.845

Li, Z.H., Gerya, T., Connolly, J.A.D., 2019. Variability of subducting slab morphologies in the mantle transition zone: Insight from petrological-thermomechanical modeling. Earth-Science Rev. https://doi.org/10.1016/j.earscirev.2019.05.018

Liu, S., Gurnis, M., Ma, P., Zhang, B., 2017. Reconstruction of northeast Asian deformation integrated with western Pacific plate subduction since 200 Ma. Earth-Science Rev. https://doi.org/10.1016/j.earscirev.2017.10.012

Loegering, M.J., Anka, Z., Autin, J., di Primio, R., Marchal, D., Rodriguez, J.F., Franke, D., Vallejo, E., 2013. Tectonic evolution of the Colorado Basin, offshore Argentina,

inferred from seismo-stratigraphy and depositional rates analysis. Tectonophysics 604, 245–263. https://doi.org/10.1016/j.tecto.2013.02.008

Lynch, H.D., Morgan, P., 1987. The tensile strength of the lithosphere and the localization of extension. Geol. Soc. Spec. Publ. 28, 53–65. https://doi.org/10.1144/GSL.SP.1987.028.01.05

Lyu, T., Zhu, Z., Wu, B., 2019. Subducting slab morphology and mantle transition zone upwelling in double-slab subduction models with inward-dipping directions. Geophys. J. Int. 218, 2089–2105. https://doi.org/10.1093/gji/ggz268

Maruyama, S., Santosh, M., Zhao, D., 2007. Superplume, supercontinent, and post-perovskite: Mantle dynamics and anti-plate tectonics on the Core-Mantle Boundary. Gondwana Res. 11, 7–37. https://doi.org/10.1016/j.gr.2006.06.003

Matthews, K.J., Maloney, K.T., Zahirovic, S., Williams, S.E., Seton, M., Müller, R.D., 2016. Global plate boundary evolution and kinematics since the late Paleozoic. Glob. Planet. Change 146, 226–250. https://doi.org/10.1016/j.gloplacha.2016.10.002

Maunder, B., Prytulak, J., Goes, S., Reagan, M., 2020. Rapid subduction initiation and magmatism in the Western Pacific driven by internal vertical forces. Nat. Commun. 11, 1874. https://doi.org/10.1038/s41467-020-15737-4

McKenzie, D.P., Roberts, J.M., Weiss, N.O., 1974. Convection in the earth's mantle: towards a numerical simulation. J. Fluid Mech. 62, 465. https://doi.org/10.1017/S0022112074000784

Meyer, C., Schellart, W.P., 2013. Three-dimensional dynamic models of subducting plate-overriding plate-upper mantle interaction. J. Geophys. Res. Solid Earth 118,

775–790. https://doi.org/10.1002/jgrb.50078

Mibe, K., Kawamoto, T., Matsukage, K.N., Fei, Y., Ono, S., 2011. Slab melting versus slab dehydration in subduction-zone magmatism. Proc. Natl. Acad. Sci. U. S. A. 108, 8177–8182. https://doi.org/10.1073/pnas.1010968108

Miller, K.A., Thompson, K.F., Johnston, P., Santillo, D., 2018. An overview of seabed mining including the current state of development, environmental impacts, and knowledge gaps. Front. Mar. Sci. 4. https://doi.org/10.3389/fmars.2017.00418

Mohriak, W., 2020. Genesis and evolution of the South Atlantic volcanic islands offshore Brazil. Geo-Marine Lett. 40, 1–33. https://doi.org/10.1007/s00367-019-00631-w

Mohriak, W.U., Fainstein, R., 2012. Phanerozoic regional geology of the eastern Brazilian margin, in: Regional Geology and Tectonics: Phanerozoic Passive Margins, Cratonic Basins and Global Tectonic Maps. Elsevier, pp. 222–282.

Montési, L.G.J., Hirth, G., 2003. Grain size evolution and the rheology of ductile shear zones: From laboratory experiments to postseismic creep. Earth Planet. Sci. Lett. 211, 97–110. https://doi.org/10.1016/S0012-821X(03)00196-1

Morishita, T., Hirano, N., Sumino, H., Sato, H., Shibata, T., Yoshikawa, M., Arai, S., Nauchi, R., Tamura, A., 2020. Alkali basalt from the Seifu Seamount in the Sea of Japan: Post-spreading magmatism in a back-arc setting. Solid Earth 11, 23–36. https://doi.org/10.5194/se-11-23-2020

Morley, C.K., Alvey, A., 2015. Is spreading prolonged, episodic or incipient in the Andaman Sea? Evidence from deepwater sedimentation. J. Asian Earth Sci. 98, 446–456. https://doi.org/10.1016/j.jseaes.2014.11.033

Müller, R.D., Sdrolias, M., Gaina, C., Roest, W.R., 2008. Age, spreading rates, and spreading asymmetry of the world's ocean crust. Geochemistry, Geophys. Geosystems 9, 1–19. https://doi.org/10.1029/2007GC001743

Nakakuki, T., Mura, E., 2013. Dynamics of slab rollback and induced back-arc basin formation. Earth Planet. Sci. Lett. 361, 287–297. https://doi.org/10.1016/j.epsl.2012.10.031

Navarrete, C., Gianni, G., Encinas, A., Márquez, M., Kamerbeek, Y., Valle, M., Folguera, A., 2019. Triassic to Middle Jurassic geodynamic evolution of southwestern Gondwana: From a large flat-slab to mantle plume suction in a rollback subduction setting. Earth-Science Rev. 194, 125–159. https://doi.org/10.1016/j.earscirev.2019.05.002

O'neill, C., Marchi, S., Zhang, S., Bottke, W., O'Neill, C., Marchi, S., Zhang, S., Bottke, W., 2017. Impact-driven subduction on the Hadean Earth. Nat. Geosci. 10, 793–797. https://doi.org/10.1038/NGEO3029

Parson, L.M., Wright, I.C., 1996. The Lau-Havre-Taupo back-arc basin: A southward-propagating, multi-stage evolution from rifting to spreading. Tectonophysics 263, 1–22. https://doi.org/10.1016/S0040-1951(96)00029-7

Parsons, B., Sclater, J.G., 1977. An analysis of the variation of ocean floor bathymetry and heat flow with age. J. Geophys. Res. 82, 803–827. https://doi.org/10.1029/JB082i005p00803

Perfit, M.R., Gust, D.A., Bence, A.E., Arculus, R.J., Taylor, S.R., 1980. Chemical characteristics of island-arc basalts: Implications for mantle sources. Chem. Geol. 30, 227–256. https://doi.org/10.1016/0009-2541(80)90107-2

Perrin, A., Goes, S., Prytulak, J., Rondenay, S., Davies, D.R., 2018. Mantle wedge temperatures and their potential relation to volcanic arc location. Earth Planet. Sci. Lett. 501, 67–77. https://doi.org/10.1016/j.epsl.2018.08.011

Pusok, A.E., Stegman, D.R., 2020. The convergence history of India-Eurasia records multiple subduction dynamics processes. Sci. Adv. 6. https://doi.org/10.1126/sciadv.aaz8681

Ranalli, G., 1995. Rheology of the Earth. Springer Science & Business Media.

Rawlinson, N., Davies, D.R., Pilia, S., 2017. The mechanisms underpinning Cenozoic intraplate volcanism in eastern Australia: Insights from seismic tomography and geodynamic modeling. Geophys. Res. Lett. 44, 9681–9690. https://doi.org/10.1002/2017GL074911

Ren, R., Guan, S.W., Zhang, S.C., Wu, L., Zhang, H.Y., 2020. How did the peripheral subduction drive the Rodinia breakup: Constraints from the Neoproterozoic tectonic process in the northern Tarim Craton. Precambrian Res. 339. https://doi.org/10.1016/j.precamres.2020.105612

Ribe, N.M., 2001. Bending and stretching of thin viscous sheets. J. Fluid Mech. 433, 135–160. https://doi.org/10.1017/S0022112000003360

Richards, F.D., Hoggard, M.J., Cowton, L.R., White, N.J., 2018. Reassessing the Thermal Structure of Oceanic Lithosphere With Revised Global Inventories of Basement Depths and Heat Flow Measurements. J. Geophys. Res. Solid Earth 123, 9136–9161. https://doi.org/10.1029/2018JB015998

Rodríguez-González, J., Billen, M.I., Negredo, A.M., 2014. Non-steady-state subduction and trench-parallel flow induced by overriding plate structure. Earth

Planet. Sci. Lett. 401, 227–235. https://doi.org/10.1016/j.epsl.2014.06.013

Ruellan, E., Delteil, J., Wright, I., Matsumoto, T., 2003. From rifting to active spreading in the Lau Basin-Havre trough backarc system (SW Pacific): Locking/unlocking induced by seamount chain subduction. Geochemistry, Geophys. Geosystems 4. https://doi.org/10.1029/2001GC000261

Ruh, J.B., Tokle, L., Behr, W.M., 2022. Grain-size-evolution controls on lithospheric weakening during continental rifting. Nat. Geosci. https://doi.org/10.1038/s41561-022-00964-9

Santosh, M., 2010. Assembling North China Craton within the Columbia supercontinent: The role of double-sided subduction. Precambrian Res. 178, 149–167. https://doi.org/10.1016/j.precamres.2010.02.003

Schellart, W.P., 2017. A geodynamic model of subduction evolution and slab detachment to explain Australian plate acceleration and deceleration during the latest Cretaceous-early Cenozoic. Lithosphere 9, 976–986. https://doi.org/10.1130/L675.1

Schellart, W.P., 2008. Subduction zone trench migration: Slab driven or overriding-plate-driven? Phys. Earth Planet. Inter. 170, 73–88. https://doi.org/10.1016/j.pepi.2008.07.040

Schellart, W.P., 2007. The potential influence of subduction zone polarity on overriding plate deformation, trench migration and slab dip angle. Tectonophysics 445, 363–372. https://doi.org/10.1016/j.tecto.2007.09.009

Schellart, W.P., Moresi, L., 2013. A new driving mechanism for backarc extension and backarc shortening through slab sinking induced toroidal and poloidal mantle flow:

Results from dynamic subduction models with an overriding plate. J. Geophys. Res. Solid Earth 118, 3221–3248. https://doi.org/10.1002/jgrb.50173

Schellart, W.P., Stegman, D.R., Farrington, R.J., Moresi, L., 2011. Influence of lateral slab edge distance on plate velocity, trench velocity, and subduction partitioning. J. Geophys. Res. Solid Earth 116, 1–15. https://doi.org/10.1029/2011JB008535

Schellart, W.P., Stegman, D.R., Freeman, J., 2008. Global trench migration velocities and slab migration induced upper mantle volume fluxes: Constraints to find an Earth reference frame based on minimizing viscous dissipation. Earth-Science Rev. 88, 118–144. https://doi.org/10.1016/j.earscirev.2008.01.005

Schliffke, N., van Hunen, J., Allen, M.B., Magni, V., Gueydan, F., 2022. Episodic back-arc spreading centre jumps controlled by transform fault to overriding plate strength ratio. Nat. Commun. 13, 582. https://doi.org/10.1038/s41467-022-28228-5

Sdrolias, M., Müller, R.D., 2006. Controls on back-arc basin formation. Geochemistry, Geophys. Geosystems 7. https://doi.org/10.1029/2005GC001090

Sharples, W., Jadamec, M.A., Moresi, L.N., Capitanio, F.A., 2014. Overriding plate controls on subduction evolution. J. Geophys. Res. Solid Earth 119, 6684–6704. https://doi.org/10.1002/2014JB011163

Shi, Y.-N.N., Niu, F., Li, Z.-H.H., Huangfu, P., 2020. Craton destruction links to the interaction between subduction and mid-lithospheric discontinuity: Implications for the eastern North China Craton. Gondwana Res. 83, 49–62. https://doi.org/10.1016/j.gr.2020.01.016

Sleep, N.H., Toksöz, M.N., 1971. Evolution of Marginal Basins. Nature 233, 548–550.

https://doi.org/10.1038/233548a0

Stegman, D.R., Freeman, J., Schellart, W.P., Moresi, L., May, D., 2006. Influence of trench width on subduction hinge retreat rates in 3-D models of slab rollback. Geochemistry, Geophys. Geosystems 7, n/a-n/a. https://doi.org/10.1029/2005GC001056

Stein, C.A., Stein, S., 1992. A model for the global variation in oceanic depth and heat flow with lithospheric age. Nature 359, 123–129. https://doi.org/10.1038/359123a0

Steinberger, B., Becker, T.W., 2018. A comparison of lithospheric thickness models. Tectonophysics 746, 325–338. https://doi.org/10.1016/j.tecto.2016.08.001

Stern, R.J., 2018. The evolution of plate tectonics. Philos. Trans. R. Soc. A Math. Phys. Eng. Sci. 376, 20170406. https://doi.org/10.1098/rsta.2017.0406

Sternai, P., Jolivet, L., Menant, A., Gerya, T., 2014. Driving the upper plate surface deformation by slab rollback and mantle flow. Earth Planet. Sci. Lett. 405, 110–118. https://doi.org/10.1016/j.epsl.2014.08.023

Straub, S.M., Gómez-Tuena, A., Vannucchi, P., 2020. Subduction erosion and arc volcanism. Nat. Rev. Earth Environ. 1, 574–589. https://doi.org/10.1038/s43017-020-0095-1

Suchoy, L., Goes, S., Maunder, B., Garel, F., Davies, R., 2021. Effects of basal drag on subduction dynamics from 2D numerical models. Solid Earth 12, 79–93. https://doi.org/10.5194/se-12-79-2021

Tamaki, K., Suyehiro, K., Allan, J., Ingle Jr, J.C., Pisciotto, K.A., 1992. Tectonic

Synthesis and Implications of Japan Sea ODP Drilling, in: Proceedings of the Ocean Drilling Program, Sci. Results. pp. 1333–1348.

Tatsumi, Y., Maruyama, S., Nohda, S., 1990. Mechanism of backarc opening in the Japan Sea: role of asthenospheric injection. Tectonophysics 181, 299–306. https://doi.org/10.1016/0040-1951(90)90023-2

Taylor, B., Zellmer, K., Martinez, F., Goodliffe, A., 1996. Sea-floor spreading in the Lau back-arc basin. Earth Planet. Sci. Lett. 144, 35–40. https://doi.org/10.1016/0012-821x(96)00148-3

Timm, C., Bassett, D., Graham, I.J., Leybourne, M.I., De Ronde, C.E.J., Woodhead, J., Layton-Matthews, D., Watts, A.B., 2013. Louisville seamount subduction and its implication on mantle flow beneath the central Tonga-Kermadec arc. Nat. Commun. 4. https://doi.org/10.1038/ncomms2702

Toksöz, M.N., Hsui, A.T., 1978. Numerical studies of back-arc convection and the formation of marginal basins. Tectonophysics 50, 177–196. https://doi.org/10.1016/0040-1951(78)90134-8

Tosi, N., Stein, C., Noack, L., Hüttig, C., Maierová, P., Samuel, H., Davies, D.R., Wilson, C.R., Kramer, S.C., Thieulot, C., Glerum, A., Fraters, M., Spakman, W., Rozel, A., Tackley, P.J., 2015. A community benchmark for viscoplastic thermal convection in a 2-D square box. Geochemistry, Geophys. Geosystems 16, 2175–2196. https://doi.org/10.1002/2015GC005807

Turcotte, D.L., Schubert, G., 2014. Geodynamics, 3rd ed. Cambridge University Press, Cambridge. https://doi.org/10.1017/CBO9780511843877

Uyeda, S., 1981. Subduction zones and back arc basins — A review. Geol.

Rundschau 70, 552–569. https://doi.org/10.1007/BF01822135

Uyeda, S., Kanamori, H., 1979. Back-arc opening and the mode of subduction. J. Geophys. Res. 84, 1049. https://doi.org/10.1029/jb084ib03p01049

Vaes, B., van Hinsbergen, D.J.J., Boschman, L.M., 2019. Reconstruction of Subduction and Back-Arc Spreading in the NW Pacific and Aleutian Basin: Clues to Causes of Cretaceous and Eocene Plate Reorganizations. Tectonics 38, 1367–1413. https://doi.org/10.1029/2018TC005164

Van Benthem, S., Govers, R., Spakman, W., Wortel, R., 2013. Tectonic evolution and mantle structure of the Caribbean. J. Geophys. Res. Solid Earth 118, 3019–3036. https://doi.org/10.1002/jgrb.50235

van der Meer, D.G., van Hinsbergen, D.J.J., Spakman, W., 2018. Atlas of the underworld: Slab remnants in the mantle, their sinking history, and a new outlook on lower mantle viscosity. Tectonophysics 723, 309–448. https://doi.org/10.1016/j.tecto.2017.10.004

van Dinther, Y., Morra, G., Funiciello, F., Faccenna, C., 2010. Role of the overriding plate in the subduction process: Insights from numerical models. Tectonophysics 484, 74–86. https://doi.org/10.1016/j.tecto.2009.08.038

van Hinsbergen, D.J.J., Steinberger, B., Guilmette, C., Maffione, M., Gürer, D., Peters, K., Plunder, A., McPhee, P.J., Gaina, C., Advokaat, E.L., Vissers, R.L.M., Spakman, W., 2021. A record of plume-induced plate rotation triggering subduction initiation. Nat. Geosci. 14, 626–630. https://doi.org/10.1038/s41561-021-00780-7

van Zelst, I., Crameri, F., Pusok, A.E., Glerum, A., Dannberg, J., Thieulot, C., 2022.

101 geodynamic modelling: how to design, interpret, and communicate numerical studies of the solid Earth. Solid Earth 13, 583–637. https://doi.org/10.5194/se-13-583-2022

Vlaar, N.J., Wortel, M.J.R., 1976. Lithospheric aging, instability and subduction. Tectonophysics 32, 331–351. https://doi.org/10.1016/0040-1951(76)90068-8

Walker, K.T., McGeary, S.E., Klemperer, S.L., 2003. Tectonic evolution of the Bristol Bay basin, southeast Bering Sea: Constraints from seismic reflection and potential field data. Tectonics 22, 1–19. https://doi.org/10.1029/2002tc001359

Wang, L., He, X., 2020. Seismic Anisotropy in the Java-Banda and Philippine Subduction Zones and its Implications for the Mantle Flow System Beneath the Sunda Plate. Geochemistry, Geophys. Geosystems 21, 1–19. https://doi.org/10.1029/2019GC008658

Wang, T., Tong, Y., Xiao, W., Guo, L., Windley, B.F., Donskaya, T., Li, S., Narantsetseg, T., Zhang, J., 2021. Rollback, scissor-like closure of the Mongol-Okhotsk Ocean and formation of an orocline: Magmatic migration based on a large archive of age-data. Natl. Sci. Rev. nwab210. https://doi.org/10.1093/nsr/nwab210

Wenker, S., Beaumont, C., 2018. Effects of lateral strength contrasts and inherited heterogeneities on necking and rifting of continents. Tectonophysics 746, 46–63. https://doi.org/10.1016/j.tecto.2016.10.011

Windley, B.F., Maruyama, S., Xiao, W.J., 2010. Delamination/thinning of sub-continental lithospheric mantle under eastern China: The role of water and multiple subduction. Am. J. Sci. 310, 1250–1293.

https://doi.org/10.2475/10.2010.03

Yang, A.Y., Langmuir, C.H., Cai, Y., Michael, P., Goldstein, S.L., Chen, Z., 2021. A subduction influence on ocean ridge basalts outside the Pacific subduction shield. Nat. Commun. 12, 4757. https://doi.org/10.1038/s41467-021-25027-2

Yang, J., Faccenda, M., 2020. Intraplate volcanism originating from upwelling hydrous mantle transition zone. Nature 579, 88–91. https://doi.org/10.1038/s41586-020-2045-y

Yang, J., Zhao, L., Kaus, B.J.P., Lu, G., Wang, K., Zhu, R., 2018. Slab-triggered wet upwellings produce large volumes of melt: Insights into the destruction of the North China Craton. Tectonophysics 746, 266–279. https://doi.org/10.1016/j.tecto.2017.04.009

Yang, T., Moresi, L., Gurnis, M., Liu, S., Sandiford, D., Williams, S., Capitanio, F.A., 2019. Contrasted East Asia and South America tectonics driven by deep mantle flow. Earth Planet. Sci. Lett. 517, 106–116. https://doi.org/10.1016/j.epsl.2019.04.025

Young, A., Flament, N., Maloney, K., Williams, S., Matthews, K., Zahirovic, S., Müller, R.D., 2019. Global kinematics of tectonic plates and subduction zones since the late Paleozoic Era. Geosci. Front. 10, 989–1013. https://doi.org/10.1016/j.gsf.2018.05.011

Zhang, N., Dang, Z., Huang, C., Li, Z.X., 2018. The dominant driving force for supercontinent breakup: Plume push or subduction retreat? Geosci. Front. 9, 997–1007. https://doi.org/10.1016/j.gsf.2018.01.010